UCLA
UCLA Electronic Theses and Dissertations

Title
Two-dimensional semiconducting materials for next-generation electronics and optoelectronics

Permalink
https://escholarship.org/uc/item/30s3t0dm

Author
Wang, Chen

Publication Date
2017

Peer reviewed|Thesis/dissertation

eScholarship.org Powered by the California Digital Library
University of California

UNIVERSITY OF CALIFORNIA

Los Angeles

Two-dimensional Semiconducting Materials for Next-generation Electronics and Optoelectronics

A dissertation submitted in partial satisfaction of the requirements for the degree Doctor of Philosophy in Material Science and Engineering

by

Chen Wang

2017

© Copyright by

Chen Wang

2017

ABSTRACT OF THE DISSERTATION

Two-dimensional Semiconducting Materials

for Next-generation Electronics and Optoelectronics

by

Chen Wang

Doctor of Philosophy in Material Science and Engineering

University of California, Los Angeles, 2017

Professor Yu Huang, Chair

The discovery of atomically thin graphene has ignited intensive interest in two-dimensional (2D) layered materials. These two-dimensional materials represent a new class of nearly ideal 2D material systems for exploring fundamental chemistry and physics at the limit of monolayer thickness, and have the potential to open up totally new technological opportunities beyond the reach of existing materials. In general, there are wide range of two-dimensional materials in which the atomic layers are weakly bonded together by van der Waals interactions and can be isolated into single or few-layer nanosheets. Among them, semiconducting two-dimensional materials, including transition metal dichalcogenides or phosphorene, attract most attention due to broad application of next-generation electronics and optoelectronics.

My Ph.D research interest is applying standard micro/nano synthesis, fabrication, and processing equipment to creatively develop next-generation nanoelectronics and nanophotonics devices by employing two-dimensional (2D) semiconducting materials and novel device concepts.

In detail, transition metal dichalcogenides (TMDs), such as WS_2, WSe_2, MoS_2, $MoSe_2$, represent a large family of layered materials, many of which exhibit tunable band gaps that can transition from an indirect band gap in bulk crystals to direct a band gap in monolayer nanosheets. Besides, black phosphorus and monolayer phosphorene attracted considerable recent interest as an alternative layered semiconductor expected to exhibit high carrier mobility and layer-number tunable electronic properties. An important feature of these layered materials is the van der Waals interactions between neighboring layers that may allow much more flexible integration of distinct materials without the limitation of lattice mismatch, the similar lattice structure but with distinct properties that enable lateral epitaxial heterogeneous integration, thus opening up vast possibilities to nearly arbitrarily combine and control different properties at the atomic scale.

My first research project focused on the FETs performance optimization using WSe_2, a new 2D transition metal dichalcogenides (TMDs) (*Nano Lett* 15, 709-713 (2015)). By tuning the substrate temperature gradient, carrier gas flow, and relative position of the targeted substrate in a home-made CVD system, I succeeded in producing high quality and large scale WSe_2 flake with controllable layer number, single crystal size, and even stacking mode, which in turn achieved exceptional transistors performance with record hole mobility of over 350 $cm^2V^{-1}s^{-1}$ and on/off ratio of above 10^8. This experience gave me a unique perspective on

the optimization of CVD parameters and device contact engineering.

Driven by this pioneering study of WSe_2, I further developed an in situ source-switch CVD system to synthesize the first atomically thin WSe_2/WS_2 heterostructure with 1D interface. Based on this specially designed heterostructure, I made the first WSe_2/WS_2 heterojunction featuring the photovoltaic effect. (*Nat. Nanotechnol*. 9, 1024 (2014)). My research with this promising material is an important advance in the development of layered semiconductor heterostructures and an essential step towards achieving functional 2D electronics. I also did deep research on the synthesis and electronic properties of the $WS_{2x}Se_{2-2x}$ alloy nanosheets, which realized the full optical response and electronic properties tuning of the two-dimensional material. Additionally, our pioneering method realized the controllable doping of TMDs by the modulation of atomic ratio (*Nano Lett*. 16, 264 (2016)).

Fascinated by 2D materials, I extended this research by developing a novel intercalation method to obtain the monolayer phosphorene molecular superlattice (MPMS), based on black phosphorus (BP), an emerging 2D materials with great electronics application potential. With this creative method, I can now control BP from few-layer down to monolayer without properties degradation, and achieve exceptionally high performance with the MPMS transistors to 10^7 on/off ratio and a lifetime of 15X than that of BP. I also developed a novel device concept, BP-MPMS heterojunction with typical p+/p++ junction properties.

The dissertation of Chen Wang is approved.

Mark Goorsky

Xiangfeng Duan

Yu Huang, Committee Chair

University of California, Los Angeles

2017

Table of Contents

ACKNOWLEDGEMENTS....................xii

BIOGRAPHY....................xv

INTRODUCTION....................1

A. Introduction to 2D semiconducting materials....................1

B. Figures and Legends....................6

C. References....................7

Chapter I: LARGE AREA GROWTH OF P-TYPE WSE2 ATOMIC LAYERS AND ITS ELECTRICAL PROPERTIES....................13

A. Introduction to p-type TMD: WSe_2....................13

B. CVD synthesized methods and morphology control....................14

C. Characterization of p-type WSe_2....................18

D. Electrical properties of p-type WSe_2....................21

E. Discussion and Summary....................23

F. Figures and Legends....................24

G. References....................32

Chapter II: LATERAL EPITAXIAL GROWTH OF TWO-DIMENSIONAL LAYERED SEMICONDUCTOR WS2-WSE2 HETEROJUNCTIONS....................36

A. Introduction to lateral TMD heterostructure....................36

B. Lateral epitaxial growth strategy....................37

C. Characterization of WS_2-WSe_2 lateral heterostructures....................39

D. Electronic characterizations and heterostructure devices....................42

E. Discussion and summary..45

F. Method Summary..47

G. Figures and Legends..49

H. References..54

Chapter III: SYNTHESIS OF WS2XSE2-2X ALLOY NANOSHEETS WITH COMPOSITION TUNABLE ELECTRONIC PROPERTIES...59

A. Introduction to semiconductor TMD alloy...59

B. Dual source CVD growth of $WS_{2x}Se_{2-2x}$ alloy..61

C. Characterization of $WS_{2x}Se_{2-2x}$ alloy...62

D. Electrical properties of $WS_{2x}Se_{2-2x}$ alloy..65

E. Discussion and summary..68

F. Figures and Legends...70

G. References..77

Chapter IV: MONOLAYER PHOSPHORENE MOLECULAR SUPERLATTICES............85

A. Black phosphorus and phosphorene electronics...85

B. Intercalation of thin black phosphorus...86

C. Electrochemical intercalation dynamics...87

D. Structural characterizations of MPMS...90

E. DFT calculation of atomic structure and electronic structure...91

F. Raman spectroscopic studies..93

G. Electrical properties and stability analysis..94

H. Lateral BP-MPMS heterojunctions...96

I. Discussion and summary..97

J. Materials and methods..98

K. Supplementary Text..99

L. Figure and Legends..103

M. References..114

List of Figures

Figure 1-1. Two-dimensional transition metal dichalcogenides (2D-TMD)............................6

Figure 2-1. Schematic illustration of the growth equipment and recipe.................................24

Figure 2-2. Reactor-conditions-dependent WSe_2 growth with varying temperature and flow rate of argon..25

Figure 2-3. Time dependent growth of large area monolayer WSe_2 single crystal domains.. 26

Figure 2-4. Micro-Raman investigation of the monodomain WSe_2.......................................27

Figure 2-5. Optical properties of the single domain and fully covered WSe_2 monolayers......28

Figure 2-6. Crystalline structure characterization...29

Figure 2-7. Electrical characteristics of the WSe_2 monodomains..30

Figure 2-8. Electronic properties of WSe_2 atomic layers...31

Figure 3-1. Schematic illustration of the home-built CVD system for the growth of WS_2-WSe_2 lateral heterostructures..49

Figure 3-2. Schematic illustration of lateral epitaxial growth WS_2-WSe_2 heterostructures....50

Figure 3-3. The AFM, Raman and photoluminescence (PL) characterizations of WS_2-WSe_2 lateral heterostructures...51

Figure 3-4. Structural and chemical modulation in WS_2-WSe_2 lateral heterostructures..........52

Figure 3-5. Electrical characterizations and functional devices from WS_2-WSe_2 lateral heterojunctions..53

Figure 4-1. Schematic illustration of the home-built CVD system..70

Figure 4-2. Bandgap engineering of $WS_{2x}Se_{2-2x}$ nanosheets..71

Figure 4-3. The evolution of Raman spectra in the $WS_{2x}Se_{2-2x}$ monolayer nanosheets as a

function of chemical composition..72

Figure 4-4. Composition and crystal structure analysis of the alloy nanosheet by TEM.........73

Figure 4-5. Electrical transport properties of $WS_{2x}Se_{2-2x}$ alloy nanosheets............................74

Figure 4-6. Typical AFM image of $WS_{2x}Se_{2-2x}$ nanosheets (x=0.668) with thickness 0.86 nm..75

Figure 4-7. Relationship between the lattice constants derived from SAED studies and the alloy composition...75

Figure 4-8. Transfer characteristics of $WS_{2x}Se_{2-2x}$ (x=0.515) transistors...............................76

Figure 4-9. Transfer characteristics of $WS_{2x}Se_{2-2x}$ nanosheet transistors with different S atomic ratio from nearly pure WSe_2 to nearly pure WS_2...76

Figure 5-1. *in situ* electrochemical-optical measurement (IS-ECOM) platform to monitor electrochemical intercalation in real time..103

Figure 5-2. Structural and property evolution from BP to MPMS during the dynamic electrochemical intercalation process...104

Figure 5-3. TEM characterization of structure evolution from BP to MPMS.......................105

Figure 5-4. The calculated electronic band structure evolution from BP to MPMS..............106

Figure 5-5. Raman spectra characterization of BP and MPMS..107

Figure 5-6. Electrical properties evolution from BP to MPMS and stability comparison.....108

Figure 5-7. Lateral BP-MPMS heterojunction...109

Figure 5-8. Stepwise reaction mechanism and its partition map...110

Figure 5-9. Photoluminescence spectrum of thin black phosphorus.....................................110

Figure 5-10. XRD of mixed few-layer phosphorene molecular superstructure....................111

Figure 5-11. TEM EDX spectra of BP and MPMS..111

Figure 5-12. Raman peak of CH_3 antisym deformation or CH_2 scissors vibration from CTAB...112

Figure 5-13. Statistical analysis of six MPMS devices performance compared with few-layer and thin BP devices of recent other studies..112

Table 1. Device key characteristics compassion between MPMS and other recent studies..113

Acknowledgements

Foremost, I would like to express my sincere gratitude to my advisors Prof. Yu Huang and Prof. Xiangfeng Duan for their patience, motivation, enthusiasm, criticism and immense knowledge and skills. Your guidance helped me in all the time of my research and writing of this thesis. I could not have imagined completing my PhD research and this thesis without your supervision.

Besides my advisors, I would like to thank the rest of my thesis committee: Prof. Yang Yang and Prof. Mark Goorsky, for their encouragement, talented comments, and insightful questions. Special thanks to my research collaborators, including Dr. Xidong Duan (Hunan University), Prof. William A. Goddard III (Caltech), Dr. Yuanyue Liu (Caltech), Dr. Hai Xiao (Caltech), Prof. Xianhui Chen (USTC), Dr. Guojun Ye (USTC), Mr. Zeliang Sun (USTC), Prof. Liangzhi Kou (Queensland University of Technology). Great thanks go to UCLA NRF Nanolab staff, including Tom Lee, Wilson Lin, Hoc Ngo, Brian Matthews, Noah Bodzin, Huynh Do and Max Ho for the support in clean room facilities and equipment; great thanks go to California Nanosystem Institute (CNSI) staff, including Baolai Liang, Matthew Schibler, Adam Stieg and Yuwei Fan for their support of nanocharacterization and nanofabrication; great thanks go to Minji Zhu from Center for high frequency electronics (CHFE-UCLA) for the support of RF device measurement.

Great thanks for equipment support engineers, including Jeff Burkett, Greg Hinds, John Van Noy, Drew C. Erwin from Tescan USA, Inc., Nicholas E. Burke, John Chris, John Aleksandravicius, John Ryan from HORIBA Instruments Inc., Joe Nabity from JC Nabity Lithography Systems, Adam Bertuch, TJ Ennion, Noah Cooper from Ultratech, Inc., Brian L

Bohan, Eric D. Brown, Kevin Ostler from Cambridge Lasers Laboratories, Inc. Great thanks go to UCLA facility team, including Roland Amrhein, Lex Kopfer, Marc Corey, Dirk Williams, John Myers, Joe Sykes, Anthony Bruce for lab relocation and facility maintenance support. Great thanks go to staff of Department of Materials Science and Engineering (MSE) and Department of Chemistry and Biochemistry, including Charlene Almeida, Lili Bulhoes, Patti Barrera, Sergey Prikhodko, Nicholas T. Belli, Katherine Rea, Robert Duncan, Jose Gonzalez, Nati Alcaraz.

I am also grateful to my labmates from UCLA MSE department and Chemistry department: Rui Cheng, Hailong Zhou, Qiyuan He, Udayabagya Halim, Yuxi Xu, Zhaoyang Lin, Boris Volosskiy, Dehui Li, Enbo Zhu, Yu Chen, Yongjia Li, Ziying Feng, Mengning Ding, Guolin Hao, Fanli Meng, Nathan Weiss, Yuan Liu, Hao Wu, Yun-Chiao Huang, Hung-Chieh Cheng, Jian Guo, Gongming Wang, Xiangheng Xiao, Yiliu Wang, Chuancheng Jia, Hossein Zarghami, Jonathan Shaw, Huiying Shiu, Zipeng Zhao, Zheng Fan, Chin-Yi Chiu, Jianjing Dong, Lingyan Ruan, Yang Wang, Shan Jiang, Hua Zhang, Teng Xue, Xiaoqing Huang, Sen Yang, Kayla Roeser, Anxiang Yin, Zhihong Huang, Chain Lee, Mufan Li, Ben Papandrea, Woojong Yu, Xing Zhong, Chungsuk Choi, Hyunpil Boo, Freda Lam, Jin Huang, Sungjoon Lee, Peiqi Wang, Chengzhang Wan, Huilong Fei, Shengxue Yang, Chih-Yen Chen, Xu Xu, Huajian Xu for the experimental support and enlightening suggestions.

I would like to thank my UCLA friend Yang Yang, Lisa Wang, Xiaodan Zhu, Zhu Ma, Chia-Pu Chu, Caifu Zeng, Lili Feng, Shan Jiang, Qi Chen, Huanping Zhou, Yingxia Liu, Zhihui Zhu, Huajun Chen, Xiao Ma, Dian Yu, Menglu Li, Ming Xia, Chuanzhen Zhao,

Andrew Serino, Jessica Wang, Fangchao Zhao. I'd like to thank the board member of eGSA (engineering Graduate Student Association), IGSA (International Graduate Student Association) and WHUAASC (Wuhan University Alumni Association of Sothern California), including Harsha Kittur, Zixing Deng, Sudarsan Ranganathan, Joey Lao, Tandre Oey, Shashank Gowda, Luke Shaw, Edgar Rios, Yuxiang Liu, Pranshu Bansal, Lindsey Perry, Mrinal Rath, Simon Han, Yilian Wang, Yusi Ou, Alex Fung, Jason Liu, Sherry Lin, Siyuan Meng, Chris Chen, Aoki Emi, Andy Tay, Xiaoqing Pi, Yalan Zheng, Chendi Zhu, Xiaoling Zan, Sen Cheng, Mingzhi Cai, Tong Li, Peng Qian, Diana, Lisa Smith and Chris Lu. All of you make my Ph.D life much more delightful!

Last but not least, I would like to thank my family, my parents and my sister. Thank you for the continuous support you have given me throughout my time in graduate school. You selflessly encouraged me to explore new directions in life and seek my own destiny. This journey would not have been possible if not for you, and I dedicate this milestone to you.

Biography

Chen Wang received his B.S. degree in Physics from Wuhan University, Wuhan, China in 2012. He joined Prof. Yu Huang's group in 2012 and conducted the research of two-dimensional materials for novel electronic and optoelectronics development. He was awarded *University Fellowship* in 2012 and *UCLA Dissertation Year Fellowship (DYF)* in 2016. He has 5 first-author and 15 co-author papers published/submitted in peer reviewed journals and 1 book chapter published by *Cambridge University Press*. He gives oral presentations in *Material Research Society (MRS) Spring Meeting 2017* in Phoenix and the *17th IEEE International Conference on Nanotechnology 2017 (IEEE-Nano 2017)* in Pittsburgh. He is currently the Associate Editor of *Micro & Nano Letters*, Institute of Engineering and Technology, and Associate Editor and Track Chair of *IEEE-Nano 2017*. His research interests include two-dimensional semiconducting materials and its electronic and optoelectronic device development.

INTRODUCTION

A. Introduction to two-dimensional semiconducting materials

Graphene, a single atomic sheet of carbon atoms arranged in a honeycomb lattice, has taken the center stage of materials science for both fundamental studies and many potential applications, ever since its first discovery in 2004. In particular, graphene exhibits many unique characteristics that make it a highly attractive materials for a new generation electronics with unprecedented combination of speed and flexibility.[1] For example, graphene exhibits a highest carrier mobility up to 1,000,000 $cm^2/V \cdot s$ (*i.e.*, ~2-3 orders of magnitude higher than that in silicon) [2-5] and the highest carrier saturation velocity of all known material,[6] making it a potential channel material for ultra-high-speed transistors.[7] Additionally, the single atom thickness represents the ultimate limit for down-scaling,[8-13] while the large area two-dimensional structure makes it suitable for large scale integration[14-16] and the exceptional mechanical strength and elasticity make it desirable for highly robust flexible electronics.[16]

However, the lack of an intrinsic band gap in graphene has limited the achievable on/off ratio in transistors using graphene as the active channel. Considerable efforts have been devoted to addressing this challenge, including the induction of transport gap in graphene nanostructures[17-28] or bilayer graphene.[29-32] The creation of a transport gap in graphene nanostructures or bilayer graphene can improve the on/off ratio,[17,19,33] but often at a cost of the electronic performance and the deliverable current density.

To overcome limitation of semimetal nature of graphene, the recent interest is expanding to other 2D materials, particularly transition metal dichalcogenide (TMDs) with tunable

intrinsic band gap (Fig. 1-1). The transition metal dichalcogenides (TMDs) (*e.g.*, WS_2, WSe_2) represent a large family of layered materials, many of which exhibit tunable band gaps that can transit from an indirect band gap in bulk crystals to direct a band gap in monolayer nanosheets (Fig. 1-1b). These 2D-TMDs have thus emerged as an exciting class of atomically thin semiconductors for a new generation of electronic and optoelectronic devices. An important feature of these 2DLMs is the *van der Waals* interactions between neighboring layers that may allow much more flexible integration of distinct materials without the limitation of lattice mismatch, and thus opening up vast possibilities to nearly arbitrarily combine and control different properties at the atomic scale (Fig. 1-1a). Recent studies have shown exciting potential of these atomically thin materials, including the demonstration of atomically thin transistors, a new design of vertical transistors, as well as new types of optoelectronic devices, including tunable photovoltaic devices and light emitting devices. In parallel, there have also been considerable efforts in developing diverse synthetic approaches for the rational growth of various forms of 2D materials with precisely controlled chemical composition, physical dimension, and heterostructure interface. To this end, black phosphorous has recently attracted considerable interest because of its moderate intrinsic band gap and considerably higher carrier mobility (~ 1000 $cm^2/V/s$) than TMDs.[34] Black phosphorus was first synthesized by applying high pressure to red phosphorus and studied in 1914 by P. W. Bridgman.[35] However, its two dimensional essence was not well studied until one hundred year later, when it was recognized as perfect materials with balanced mobility and bandgap, compared with semimetal graphene or low-mobility transition metal dichalcogenides (TMDs).[34] Together with all the advantages of 2DLMs,[16] it was regarded as

one of best electronic and optical material for post-silicon era. However, all recently works are based on thin black phosphorus, not monolayer phosphorene, because of the great difficulty to isolate monolayer black phosphorene which is not chemically stable in ambient.

In this thesis, I will present my study about high performance p-type WSe_2 transistors (*Nano Lett* 15, 709-713 (2015), WS_2-WSe_2 heterojunction by lateral epitaxial growth (*Nat. Nanotechnol*. 9, 1024 (2014), $WS_{2x}Se_{2-2x}$ alloy with tunable optical and electrical properties (*Nano Lett*. 16, 264 (2016) and novel monolayer phosphorene molecular superlattice (MPMS) with superior electrical and optical properties (submitted). I included four of my first author publications and assemble them in sequence [36-39]. My first research project focused on the FETs performance optimization using WSe_2, a member of TMDs. By tuning the substrate temperature gradient, carrier gas flow, and relative position of the targeted substrate in a home-made CVD system, we succeeded in producing high quality and large scale WSe_2 flake with controllable layer number, single crystal size, and even stacking mode, which in turn achieved exceptional transistors performance with record monolayer hole mobility of over 100 $cm^2V^{-1}s^{-1}$ and on/off ratio of above 10^8. By studying the layer number dependent electrical properties of WSe_2, the highest mobility of the few-layer WSe_2 FETs can reach up to 350 $cm^2V^{-1}s^{-1}$, which represents the highest value observed in these atomically thin TMDs at room temperature. This experience gave me a unique perspective on the optimization of CVD parameters and device contact engineering. Driven by this pioneering study of WSe_2, we further developed an *in situ* source-switch CVD system to synthesize the first atomically thin WSe_2/WS_2 heterostructure with 1D interface. By using Raman mapping, photoluminescence mapping, EDS mapping, the spatial separation of WSe_2 and WS_2 was

confirmed. Furthermore, series ED across interface, whole interface ED and EDS line scan direct verified the sharp interface with sub-40 nm (limited by TEM electron beam size). Based on this specially designed heterostructure, the first WSe_2/WS_2 heterojunction featuring the photovoltaic effect was made. My research with this promising material is an important advance in the development of layered semiconductor heterostructures and an essential step towards achieving functional 2D electronics. With quantum confinement in two dimensions at this interline (one dimensional interface) and the importance of the interface in semiconductor heterojunctions, the formation of the interline in ultrathin lateral heterostructures could open up a new door to exotic physics and totally new device concepts .

Based on above projects, I also did deep research on the synthesis of the $WS_{2x}Se_{2-2x}$ alloy nanosheets, which realized the continuous fully optical response and electronic properties tuning of the two-dimensional material from pure WS_2 to pure WSe_2. Additionally, our pioneering method realized the controllable doping of TMDs by the modulation of atomic ratio. Fascinated by 2D materials and seeking for better 2D material for next-generation electronics applications, I extended my research by developing a novel intercalation method to obtain the monolayer phosphorene molecular superlattice (MPMS), based on black phosphorus (BP), an emerging 2D materials with great electronics application potential. With this creative method, I can now control BP from few-layer down to monolayer without properties degradation, and achieve exceptionally high performance with the MPMS transistors to 10^7 on/off ratio and a lifetime of 15X than that of BP. I also developed a novel device concept, BP-MPMS heterojunction with typical p+/p++ junction properties. Our study thus defines a general strategy to preparing 2D superlattices and opens up a new pathway to

tailoring and taming the electronic properties of 2D materials for functional electronics and optoelectronics.

B. Figures and Legends

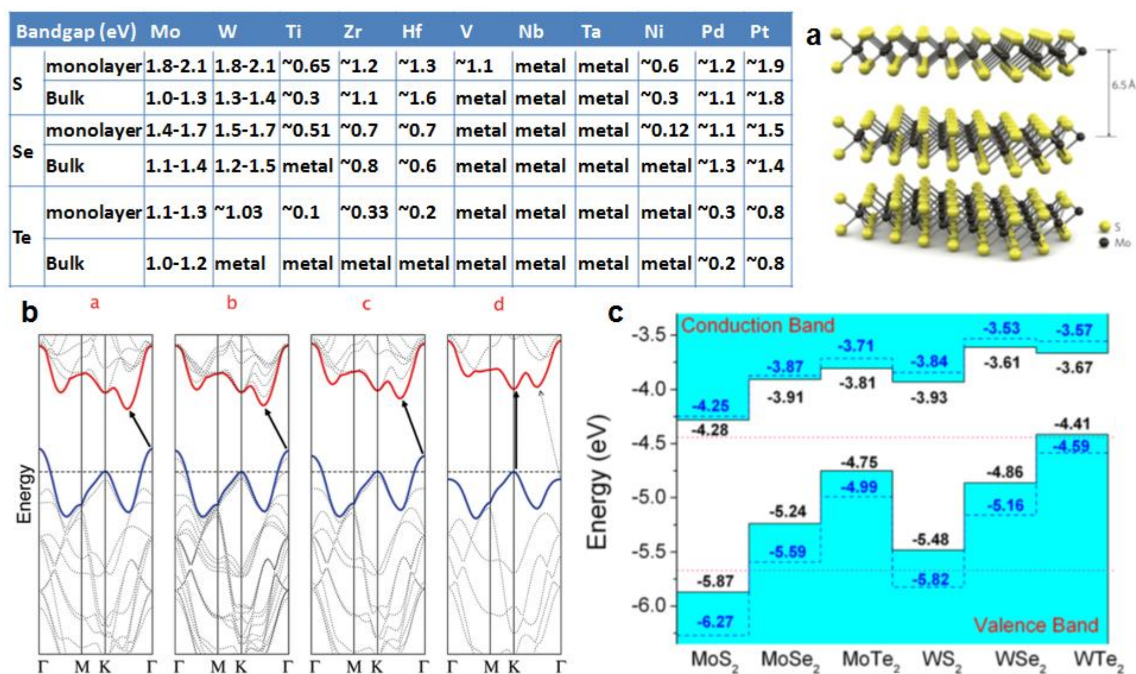

Bandgap (eV)		Mo	W	Ti	Zr	Hf	V	Nb	Ta	Ni	Pd	Pt
S	monolayer	1.8-2.1	1.8-2.1	~0.65	~1.2	~1.3	~1.1	metal	metal	~0.6	~1.2	~1.9
	Bulk	1.0-1.3	1.3-1.4	~0.3	~1.1	~1.6	metal	metal	metal	~0.3	~1.1	~1.8
Se	monolayer	1.4-1.7	1.5-1.7	~0.51	~0.7	~0.7	metal	metal	metal	~0.12	~1.1	~1.5
	Bulk	1.1-1.4	1.2-1.5	metal	~0.8	~0.6	metal	metal	metal	metal	~1.3	~1.4
Te	monolayer	1.1-1.3	~1.03	~0.1	~0.33	~0.2	metal	metal	metal	metal	~0.3	~0.8
	Bulk	1.0-1.2	metal	metal	metal	metal	metal	metal	metal	metal	~0.2	~0.8

Figure 1-1. Two-dimensional transition metal dichalcogenides (2D-TMDs). The table shows common TMDs and their band gap.[40-48] **a**, Schematic illustration of the layered structure of MoS_2. **b**, Energy dispersion in bulk, quadrilayer (4L), bilayer (2L) and monolayer (1L) MoS_2 from left to right. The horizontal dashed line represents the energy of a band maximum at the K point. The red and blue lines represent the conduction and valence band edges, respectively. The lowest energy transition increases with decreasing layer and evolve from indirect to direct (vertical). **c**, Relative valence and conduction band edge of some common TMDs (monolayer). **a**, **b**, **c** are reproduced with permission from ref. 49 Copyright 2011 Macmillan Publishers Limited, ref. 50 Copyright 2010 American Chemical Society and ref. 51 Copyright 2013 AIP Publishing LLC, respectively.

C. References

1. Schwierz, F. Graphene transistors. *Nat. Nanotechnol.* **5**, 487-496, doi:10.1038/NNANO.2010.89 (2010).

2. Bolotin, K. I. *et al.* Ultrahigh electron mobility in suspended graphene. *Solid State Communications* **146**, 351-355, doi:10.1016/j.ssc.2008.02.024 (2008).

3. Elias, D. C. *et al.* Dirac cones reshaped by interaction effects in suspended graphene. *Nat Phys* **7**, 701-704 (2011)

4. Castro, E. V. *et al.* Limits on Charge Carrier Mobility in Suspended Graphene due to Flexural Phonons. *Phys Rev Lett* **105**, doi:10.1103/PhysRevLett.105.266601 (2010).

5. Liao, L. *et al.* High-κ oxide nanoribbons as gate dielectrics for high mobility top-gated graphene transistors. *Proceedings of the National Academy of Sciences* **107**, 6711-6715, doi:10.1073/pnas.0914117107 (2010).

6. Meric, I. *et al.* Current saturation in zero-bandgap, topgated graphene field-effect transistors. *Nat. Nanotechnol.* **3**, 654-659, doi:10.1038/nnano.2008.268 (2008).

7. Liao, L. & Duan, X. Graphene for radio frequency electronics. *Materials Today* **15**, 328-338, (2012).

8. Lin, Y. M. *et al.* 100-GHz Transistors from Wafer-Scale Epitaxial Graphene. *Science* **327**, 662-662, doi:10.1126/science.1184289 (2010).

9. Jeon, D.-Y. *et al.* Radio-Frequency Electrical Characteristics of Single Layer Graphene. *Japanese Journal of Applied Physics* **48**, 091601 (2009).

10. Lin, Y.-M. *et al.* Operation of Graphene Transistors at Gigahertz Frequencies. *Nano Lett* **9**, 422-426, doi:10.1021/nl803316h (2009).

11. Xia, F., Mueller, T., Lin, Y.-M., Valdes-Garcia, A. & Avouris, P. Ultrafast graphene photodetector. *Nat Nanotechnol* **4**, 839-843, doi:10.1038/NNANO.2009.292 (2009).

12. Liao, L. *et al.* Sub-100 nm Channel Length Graphene Transistors. *Nano Lett* **10**, 3952-3956, doi:10.1021/nl101724k (2010).

13. Liao, L. *et al.* High-speed graphene transistors with a self-aligned nanowire gate. *Nature* **467**, 305-308 (2010).

14. Li, X. *et al.* Large-Area Synthesis of High-Quality and Uniform Graphene Films on Copper Foils. *Science* **324**, 1312-1314, doi:10.1126/science.1171245 (2009).

15. Reina, A. *et al.* Large Area, Few-Layer Graphene Films on Arbitrary Substrates by Chemical Vapor Deposition. *Nano Lett* **9**, 30-35, doi:10.1021/nl801827v (2009).

16. Bae, S. *et al.* Roll-to-roll production of 30-inch graphene films for transparent electrodes. *Nat Nanotechnol* **5**, 574-578, doi:10.1038/nnano.2010.132 (2010).

17. Li, X. L., Wang, X. R., Zhang, L., Lee, S. W. & Dai, H. J. Chemically derived, ultrasmooth graphene nanoribbon semiconductors. *Science* **319**, 1229-1232 (2008).

18. Bai, J. W., Duan, X. F. & Huang, Y. Rational Fabrication of Graphene Nanoribbons Using a Nanowire Etch Mask. *Nano Lett* **9**, 2083-2087, doi:10.1021/nl900531n (2009).

19. Liao, L. *et al.* Top-Gated Graphene Nanoribbon Transistors with Ultrathin High-k Dielectrics. *Nano Lett* **10**, 1917-1921 (2010).

20. Jiao, L. Y., Zhang, L., Wang, X. R., Diankov, G. & Dai, H. J. Narrow graphene nanoribbons from carbon nanotubes. *Nature* **458**, 877-880 (2009).

21. Wei, D. C. *et al.* Controllable unzipping for intramolecular junctions of graphene nanoribbons and single-walled carbon nanotubes. *Nat Commun* **4**, doi:Artn 1374

10.1038/Ncomms2366 (2013).

22. Han, M. Y., Ozyilmaz, B., Zhang, Y. B. & Kim, P. Energy band-gap engineering of graphene nanoribbons. *Phys Rev Lett* **98** (2007).

23. Yang, L., Park, C. H., Son, Y. W., Cohen, M. L. & Louie, S. G. Quasiparticle energies and band gaps in graphene nanoribbons. *Phys Rev Lett* **99**, doi:Artn 186801 10.1103/Physrevlett.99.186801 (2007).

24. Liao, L. *et al.* High-Performance Top-Gated Graphene-Nanoribbon Transistors Using Zirconium Oxide Nanowires as High-Dielectric-Constant Gate Dielectrics. *Adv Mater* **22**, 1941 (2010).

25. Bai, J. W., Zhong, X., Jiang, S., Huang, Y. & Duan, X. F. Graphene nanomesh. *Nat Nanotechnol* **5**, 190-194 (2010).

26. Berrada, S. *et al.* Graphene nanomesh transistor with high on/off ratio and good saturation behavior. *Appl Phys Lett* **103** (2013).

27. Seol, G., Kumar, B. & Guo, J. Performance projection of graphene nanomesh and nanoroad transistors. *Nano Res* **5**, 164-171, doi:10.1007/s12274-012-0196-3 (2012).

28. Zeng, Z. Y. *et al.* Fabrication of Graphene Nanomesh by Using an Anodic Aluminum Oxide Membrane as a Template. *Adv Mater* **24**, 4138-4142 (2012).

29. Castro, E. V. *et al.* Biased bilayer graphene: Semiconductor with a gap tunable by the electric field effect. *Phys Rev Lett* **99,** 216802 (2007).

30. Zhang, Y. B. *et al.* Direct observation of a widely tunable bandgap in bilayer graphene. *Nature* **459**, 820-823 (2009).

31. Yu, W. J., Liao, L., Chae, S. H., Lee, Y. H. & Duan, X. F. Toward Tunable Band Gap and

Tunable Dirac Point in Bilayer Graphene with Molecular Doping. *Nano Lett* **11**, 4759-4763, doi:10.1021/nl2025739 (2011).

32. Yu, W. J. & Duan, X. F. Tunable transport gap in narrow bilayer graphene nanoribbons. *Sci Rep-Uk* **3**, doi:Artn 1248 10.1038/Srep01248 (2013).

33. Xia, F. N., Farmer, D. B., Lin, Y. M. & Avouris, P. Graphene Field-Effect Transistors with High On/Off Current Ratio and Large Transport Band Gap at Room Temperature. *Nano Lett* **10**, 715-718, doi:10.1021/nl9039636 (2010).

34. Li, L. K. *et al.* Black phosphorus field-effect transistors. *Nat Nanotechnol* **9**, 372-377 (2014).

35. Bridgman, P. W. Two new modifications of phosphorus. *J Am Chem Soc* **36**, 1344-1363, doi:Doi 10.1021/Ja02184a002 (1914).

36. Duan, X. D. *et al.* Synthesis of WS2xSe2-2x Alloy Nanosheets with Composition-Tunable Electronic Properties. *Nano Lett* **16**, 264-269, doi:10.1021/acs.nanolett.5b03662 (2016).

37. Zhou, H. L. *et al.* Large Area Growth and Electrical Properties of p-Type WSe2 Atomic Layers. *Nano Lett* **15**, 709-713, doi:Doi 10.1021/Nl504256y (2015).

38. Duan, X. D. *et al.* Lateral epitaxial growth of two-dimensional layered semiconductor heterojunctions. *Nat Nanotechnol* **9**, 1024-1030, doi:Doi 10.1038/Nnano.2014.222 (2014).

39. Chen Wang, U. H., Yuanyue Liu, Enbo Zhu, Qiyuan He, Hai Xiao, Ziying Feng, Rui Cheng, Nathan O. Weiss, Guojun Ye, Yun-Chiao Huang, Hao Wu, Hung-Chieh Cheng, Xianhui Chen, William A. Goddard III, Yu Huang, Xiangfeng Duan. Monolayer phosphorene molecular superlattice. *submitted* (2017).

40. Bayliss, S. C. & Liang, W. Y. Symmetry Dependence of Optical-Transitions in Group-4b Transition-Metal Dichalcogenides. *J Phys C Solid State* **15**, 1283-1296, doi:Doi 10.1088/0022-3719/15/6/021 (1982).

41. Guo, H. Y., Lu, N., Wang, L., Wu, X. J. & Zeng, X. C. Tuning Electronic and Magnetic Properties of Early Transition-Metal Dichalcogenides via Tensile Strain. *J Phys Chem C* **118**, 7242-7249, doi:Doi 10.1021/Jp501734s (2014).

42. Kaul, A. B. Two-dimensional layered materials: Structure, properties, and prospects for device applications. *J Mater Res* **29**, 348-361, doi:Doi 10.1557/Jmr.2014.6 (2014).

43. Lebegue, S., Bjorkman, T., Klintenberg, M., Nieminen, R. M. & Eriksson, O. Two-Dimensional Materials from Data Filtering and Ab Initio Calculations. *Phys Rev X* **3**, doi:Artn 031002 Doi 10.1103/Physrevx.3.031002 (2013).

44. Lee, P. A., Said, G., Davis, R. & Lim, T. H. On the optical properties of some layer compounds. *Journal of Physics and Chemistry of Solids* **30**, 2719-2729, doi:http://dx.doi.org/10.1016/0022-3697(69)90045-6 (1969).

45. Chhowalla, M. *et al.* 05 The chemistry of two-dimensional layered transition metal dichalcogenide nanosheets. *Nat Chem* **5**, 263-275, doi:Doi 10.1038/Nchem.1589 (2013).

46. Lv, R. *et al.* Transition Metal Dichalcogenides and Beyond: Synthesis, Properties, and Applications of Single- and Few-Layer Nanosheets. *Accounts of Chemical Research* **48**, 56-64, doi:10.1021/ar5002846 (2015).

47. Rasmussen, F. A. & Thygesen, K. S. Computational 2D Materials Database: Electronic Structure of Transition-Metal Dichalcogenides and Oxides. *The Journal of Physical Chemistry C*, doi:10.1021/acs.jpcc.5b02950 (2015).

48. Terrones, H., Lopez-Urias, F. & Terrones, M. Novel hetero-layered materials with tunable direct band gaps by sandwiching different metal disulfides and diselenides. *Sci Rep-Uk* **3**, doi:Artn 1549 Doi 10.1038/Srep01549 (2013).

49. Radisavljevic, B., Radenovic, A., Brivio, J., Giacometti, V. & Kis, A. Single-layer MoS_2 transistors. *Nat. Nanotechnol.* **6**, 147-150 (2011)

50. Splendiani, A. *et al.* Emerging Photoluminescence in Monolayer MoS2. *Nano Lett* **10**, 1271-1275 (2010).

51. J. Kang, S. Tongay, J. Zhou, J. B. Li, J. Q. Wu, Band offsets and heterostructures of two-dimensional semiconductors. Appl Phys Lett 102, 012111 (2013);

Chapter I: LARGE AREA GROWTH OF P-TYPE WSE2 ATOMIC LAYERS AND ITS ELECTRICAL PROPERTIES

A. Introduction to p-type TMD: WSe_2

Graphene has attracted considerable interest for applications in diverse electronic and optoelectronic devices due to its unique electronic properties and atomically thin geometry.[1-12] However, the gapless band structure limits the potential of graphene for digital electronic devices.[2,4] It has been shown the energy band structure of the transition metal dichalcogendes (TMD) materials exhibit a unique indirect-to-direct band gap transition as their layer number is reduced to one.[13-18] For example, bulk WSe_2 is a p-type semiconductor with an indirect band gap of ~1.2 eV, whereas its monolayer exhibits a direct band gap of ~ 1.65 eV.[17] The direct band gap of atomically thin TMDs can offer exciting opportunities for potential applications in both digital electronic and optoelectronic devices.[19-23] For example, it has been recently reported that exfoliated monolayer WSe_2 can be used to create a high performance p-type field-effect transistor (FET).[25] However, the size of the monolayer materials obtained from mechanical exfoliation method is limited in a few to a few tens of micrometers. It has also been recently reported that a chemical vapor deposition approach can be used to grow WSe_2 atomic flakes, but only in separated domains with the domain size on the order of 10 micrometers.[26, 27] Therefore, the preparation of large-area monolayer WSe_2 film is essential for practical applications, yet remains a significant challenge.

In this study, a systematic study of chemical vapor deposition approach for the preparation of large area atomically thin WSe_2 films directly on SiO_2/Si substrates with areal size of monolayer WSe_2 film up to 1 cm^2 was reported. Micro-photoluminescence mapping

demonstrates distinct layer-number dependent photoluminescence, with the monolayer area exhibiting much stronger emission than bilayer or multi-layers. The transmission electron microscopy (TEM) studies reveal excellent crystalline quality of the atomically thin WSe_2 and electrical transport studies further demonstrate that the p-type WSe_2 field-effect transistors exhibit excellent electronic characteristics with hole carrier mobility up to 100 $cm^2V^{-1}s^{-1}$ for monolayer and up to 350 $cm^2V^{-1}s^{-1}$ for few-layer materials, comparable or well above that of previously reported mobility values or the synthetic WSe_2 and comparable to the best exfoliated materials.[26, 36, 37]

B. CVD synthesized methods and morphology control

The growth processes are performed in a home-made tube furnace (Fig. 2-1). Briefly, the WSe_2 powders are placed in an alumina boat at the center of a quartz tube inside a one-inch tube furnace, and the clean SiO_2/Si substrates are used as the growth substrate for the deposition of WSe_2 atomic layers at the down-stream end with variable substrate temperature. Argon is continuously supplied through the reactor with designed flow rate as the carrier gas. In details, to synthesize the layered WS_2 flakes, the 0.2 g WS_2 powder (Alfa Aesar, 13084) was added into an alumina boat as precursor. The blank SiO_2/Si substrates (1 cm by 5 cm) loaded into a home-built vapor deposition system in a horizontal tube furnace (Lindberg/Blue M) with 1-inch quartz tube (Fig. 2-1). The system was pumped down to a vacuum of 10 mTorr in 10 min, and re-filled with 150 sccm of ultra-high purity argon gas (Airgas, ~ 99.9999%) then heated to desired growth temperature within 30 min. After that, the growth kept at the designed temperature for 30 min, and then terminated by shutoff the power of the furnace. The sample was naturally cooled down to ambient temperature.

We have first conducted systematic studies to investigate the effect of substrate temperature and flow rate of carrier gas with a constant source temperature at 1060 °C (Fig. 2-2). Most of the WSe_2 domains exhibit a triangular shape as shown by the optical microscope images in Fig. 2-2b, c and Fig. 2-3a-c, and some of them show a hexagonal shape as shown in Fig. 2-2g, l. In general, with a fixed source temperature, the lower substrate temperature typically results in a higher nucleation density (Fig. 2-2m), and a higher flow rate of the carrier gas produces a similar effect due to higher super-saturation of the precursors over the substrate surface (Fig. 2-2o). On the other hand, the higher substrate temperature promotes the nucleation of the extra atomic layers to produce multi-layers.

At lower substrate temperature of 750 °C with low flow rate of 100 sccm, there are apparently no visible WSe_2 domains observed on the SiO_2/Si substrates under optical microscope. However, after analyzing the same sample by using scanning electron miscroscopy (SEM), very small nuclei (~ 300 nm of average edge size) were observed with nucleation density of ~ 4200/mm^2. By increasing the substrate temperature to 765 °C, the monolayer WSe_2 domains (~ 10 μm average edge size) start to appear with a nucleation density of ~ 1060/mm^2 (Fig. 2-2b). When the substrate growth temperature reaches 780 °C, the bilayer WSe_2 domains (~ 20 μm average edge size) start to appear with an overall lower domain density reduced to ~ 350/mm^2 (Fig. 2-2c). As the substrate growth temperature is further increased to 795 °C, even thicker and larger flakes (~ 50 μm average edge size) appear with even lower domain density of ~ 280/mm^2 (Fig. 2-2d). Overall, higher substrate growth temperature yields a lower density of thicker WSe_2 domains with a larger domain size (Fig. 2-2n). By increasing the flow rate of the carrier gas, both the layer number and the

domain density of the WSe_2 are increased (Fig. 2-2o). For instance, at substrate growth temperature of 765 °C, the nucleation density of is ~ 1060/mm^2 under 100 sccm flow rate of carrier gas, which increases to ~ 11000/ mm^2 under 150 sccm, and ~ 23000/ mm^2 under 200 sccm. All of our observations are consistent with the nucleation model of the vapor phase deposition developed by W. K. Burton and N. Cabrera, where they predict that the nucleation probability is proportional to the super saturation and inversely proportional to the substrate temperature (Fig. 2-2m, 2o).[27]

In detail, the nucleation of WSe_2 from vapor phase could be understood by considering the vapor phase supersaturation. Assuming equilibrium exists at the source temperature and substrate temperature, there is no gas phase recombination or other gas phase reactions and no change in the composition in the gas phase. By increasing in the gas phase supersaturation of WSe_2 with increasing in the partial pressure of argon with both source temperature (1060°C) and substrate temperature (765°C) remaining constant, it's observed that from 100 sccm to 200 sccm argon gas flow, the nucleation density increase linearly from 1060 mm^{-2} to 23,000 mm^{-2} (Fig. 2-2o). It's worthy to note that the WSe_2 surface will transform from smooth to rough at very high driving force conditions (high supersaturation), where adhesive-type growth dominates, instead of birth and spread in the intermediate supersaturation (Fig. 2-2i). Quantitatively, based on above assumption and classical heterogeneous nucleation and growth theory,[27] the following relevant energetic dominate nucleation and thin film growth follow the equation showed below:

$$N_D = R^a \exp(\frac{E_i}{kT_S})$$
$$= R^a \exp(\frac{-E_{Des} + E_{Diff} + \Delta G^*}{kT_S})$$
$$= \left(\frac{N_A P}{\sqrt{2\pi MRT_S}} \right)^a \exp(\frac{-E_{Des} + E_{Diff} + \Delta G^*}{kT_S})$$

where, N_D is the nucleation density, R is the rate of molecular impinging, a is a constant, E_i is crystal disintegration energy, T_S is substrate temperature, k is Boltzmann's constant, E_{Des} is energetic barrier of desorption, E_{Diff} is energetic barrier of diffusion, ΔG^* is the energetic barrier of crystal formation, N_A is Avogadro constant, P is pressure, M is molecular weight, R is ideal gas constant.

It's clear that the nucleation density, $N_D \sim T_S^{-\frac{a}{2}} \exp\left(\frac{1}{T_S}\right)$, then $\ln\left(N_D\right) \sim -\frac{a}{2}\ln(T_S) + \frac{1}{T_S} \approx \frac{1}{T_S}$, so our results of nucleation density relationship with substrate temperature match this model prediction quantitatively (Fig. 2-2m). Similarly, for the relationship of carrier gas flow vs nucleation density, from above equation, we can see $N_D \sim P^a$, after we changed the flow rate, the system pressure changed, leading to nucleation density change. Quantitatively, if we fit the data to this equation, a is around 4.4. But due to the gas purity of argon is just industrial purity; the impurity from deliver gas may great increase if the flow was increased. Additionally, the nucleation density itself vs carrier gas flow relationship may not directly reflect grow mechanism, since at different flow rate, even fixed all other parameters, the growth at different flow rate will be at quite different growth stage with different thickness. Due to the 2D semiconductor growth complexity with

lateral growth, vertical growth, different stacking mode, high order island growth under different temperature and pressure, more systematical study is necessary to fully understand this mechanism.

C. Characterization of p-type WSe_2

Based on the above studies, we have identified an optimized condition for the large area growth of WSe_2 monolayers at a substrate temperature of 765°C and 100 sccm of carrier gas. Fig. 2-3a shows the OM images of typical triangular WSe_2 monolayers after 20 minute growth with an average edge length approximately 5 μm. With the continued growth, the monolayer domains starts to merge together at 30 minutes, with bilayer and few-layer domains occasionally appeared on their first layer (Fig. 2-3b). After 40 min growth, the WSe_2 monolayer domains are completely merged together to form a continuous monolayer, with a few second layer triangular domains seen with different optical contrast (Fig. 2-3c). In this case, the SiO_2/Si substrates are completely covered by the monolayer WSe_2 domains with less than 5% areal coverage of the bilayer. The number of WSe_2 atomic layers is also determined by AFM measurements (Fig. 2-3d). The AFM step heights of WSe_2 monolayer on the SiO_2 substrate is typically measured between 0.7 – 1.0 nm, and the step heights of the second layer on monolayer is around ~ 0.7 nm (line scan in Fig. 2-3d), which is consistent with the published reports of exfoliated WSe_2. [14,15] The larger step height observed in the first layer is commonly seen in graphene or other layered materials such as $MoSe_2$.[16] The lateral size of the resulted continuous monolayer WSe_2 film is as large as 1 cm^2, and is only limited by the size of the furnace (Fig. 2-3e). The large area monolayer WSe_2 film can be readily transferred onto other substrate such as the glass (Fig. 2-3f). We have further investigated the

layer number dependent morphological and optical properties of the resulting atomically thin WSe_2 films. To this end, we have employed the μ-Raman to study the monolayer/bilayer WSe_2 domains. The bilayer WSe_2 domain shows a triangular shape, which prefers to crystallize from the center of the first layer. The layer number of the WSe_2 domains is further confirmed using μ-Raman studies. The Raman spectrum of monolayer region show a single peak at 252 cm^{-1} (green line in Fig. 2-4b), corresponding to the A_{1g} resonance mode of WSe_2; and that of bilayer area show an additional small peak at 307 cm^{-1} (red line in Fig. 2-4b), corresponding to the B_{2g} resonance mode of WSe_2. In general, the B_{2g} signature mode only is active on the bilayer or few-layer region, which could reflect the presence of the additional interlayer interaction.[14,15] In contrast, the Raman A_{1g} mode of WSe_2 is less sensitive to layer thickness, only with the intensity increasing with reducing atomic layers. The corresponding Raman map recorded at A_{1g} mode can be further used to determine the layer number of the WSe_2 (Fig. 2-4c to f). The darker triangular region on the Raman map of A_{1g} mode corresponds to the bilayer or few-layer WSe_2 domain. The Raman mapping show nearly the same color contrast throughout the monolayer and bilayer or few-layer area, indicating a uniform crystal quality.

The optical properties of the monolayer WSe_2 domains and the continuous WSe_2 sheets were further investigated using micro-photoluminescence (μ-PL). The WSe_2 monodomain with single layer shows the PL peak located at approximately 767 nm, with full-width-half-maximum (FWHM) values of 24.8 nm (Fig. 2-5b), which is comparable to the published data for exfoliated WSe_2.[14,15] The corresponding μ-PL map of the monolayer WSe_2 single crystal domain shows a very uniform contrast (Fig. 2-5c), indicating the high

crystalline quality and uniformity of the as-grown WSe_2 atomic layers. We have also conducted μ-PL studies on the continuous WSe_2 film that are merged together (Fig. 2-5d). The μ-PL spectra taken of the monolayer region show the characteristic peak around 766 nm (red curve in Fig. 2-5e). The strong light emission from monolayer indicates the high quality of the continuous WSe_2 films. The μ-PL spectra taken at bilayer WSe_2 region (the darker triangular area on the OM image in Fig. 2-5d) shows a wider peak at ~ 790 nm with significantly lower intensity (black curve in Fig. 2-5e). We have further conducted μ-PL mapping studies over a relatively large area (~ 60 × 60 μm) to evaluate the overall quality of the material (Fig. 2-5f). Importantly, the PL mapping shows rather uniform emission across the entire film, indicating that the film is largely consisted of monolayer crystals. There are a few darker triangles in the PL mapping image, corresponding to the bilayer region. Additionally, it is also noted that there are some slightly darker lines, which can be attributed the grain boundaries between merged monolayer domains.

To further evaluate the atomic structure of the WSe_2 atomic layers, we have performed high resolution transmission electron microscopy (HRTEM) and electron diffraction (ED) studies. To this end, the as-grown WSe_2 crystals were transferred onto a carbon-coated TEM grid. Fig. 2-6a is the optical microscopy image. Fig. 2-6b shows a low magnification TEM image of a typical transferred WSe_2 triangular crystal, which shows increasing contrast from the edge to the center, with three distinct regions corresponding to the monolayer, bilayer and few-layer area. The energy dispersive X-ray studies demonstrate that the atomic ratio between W and Se is approximately 1:2 (Fig. 2-6c), consistent with the expected stoichiometry. We have further conducted HRTEM on different regions of the same WSe_2

flake. Fig. 2-6d to 6f show the HRTEM images of the atomic structure of the WSe_2 monolayer, bilayer, and few layers, respectively. These images were taken on the regions indicated on the Fig. 2-6b by the arrows with blue, red, and dark cyan colors, respectively. The hexagonal lattice is clearly visible from each atomic resolution image, confirming the excellent crystalline quality of the atomic layered material. The selected-area electron diffraction (SAED) is used to characterize the crystal structure of the film. Fig. 2-6g to 6i show the SAED patterns of the monolayer, bilayer and few-layer WSe_2 with the zone axis of [0001]. The single set of diffraction spots with six-fold symmetry demonstrates that the triangular monolayer is single crystals with hexagonal structures.[28] The morphology and structure of the WSe_2 were characterized with optical microscope (Olympus BX51), field emission scanning electron microscope (FESEM, JSM-6701F), high-resolution transmission electron microscopy (HRTEM, FEI Titan S/TEM at 300 kV), and Raman spectroscopy (Horiba, 514 nm laser wavelength, 50 × objective).

D. Electrical properties of p-type WSe_2

Electrical transport properties of the samples were measured at room temperature in a Lakeshore probe station (Model PTT4) with a computer-controlled precision source/measure unit (Agilent B2902A). Single back-gated FETs were fabricated on the monolayer, bilayer, and few layers WSe_2 on a silicon substrate with 300 nm SiO_2 substrates. E-beam lithography was employed to pattern the contact electrodes. The source/drain electrodes (Au: 100 nm) were deposited using e-beam evaporation. The back gate voltage was applied by using a high doped Si back gate with 300nm SiO_2 as the dielectric. Thus we have further evaluated the electronic properties of the WSe_2 atomic layers. To this end, we have fabricated back-gated

field-effect transistors (FETs) from the synthetic WSe_2 on the 300 nm SiO_2/Si substrates (Fig. 2-7, Fig. 2-8a). The source and drain electrodes (100 nm Au) defined by the electron beam lithography (EBL) and deposited using thermal evaporation. More than 100 transistors were fabricated on WSe_2 monolayer, bilayer, and few-layer monodomains. The standard transistor measurements were conducted under ambient conditions to obtain the on-currents, carrier mobility, and on/off ratios for all devices. Fig. 2-8b shows the I_{ds}-V_{ds} output characteristic of a monolayer WSe_2 FETs at various gate voltages. The linear and symmetric curves suggested that Ohmic contacts were formed at the source and drain electrodes. The I_{ds}-V_{bg} curve of the same device was measured at different drain bias from 1 V to 5 V, with the back-gate voltage sweeping from -100 V to 100 V (Fig. 2-8c). Additionally, the I_{ds}-V_{bg} curve of the typical WSe_2 monolayer, bilayer and few-layer FETs are shown in Fig. 2-7. All these IV curves show typical p-type semiconductor characteristic, consistent with mechanically exfoliated WSe_2 materials. The highest mobility of the monolayer WSe_2 FETs is 100 $cm^2V^{-1}s^{-1}$. The measured on/off ratio of this device reaches a maximum value above 1×10^8 for gate voltages swept in the range from -100 V to 100 V with a source-drain bias of 2 V, which is comparable to the best reported values for exfoliated samples, and greatly higher than synthetic samples reported previously. After analysis of all the fabricated WSe_2 FETs, we have plotted a histogram to show the mobility distribution for all devices (Fig. 2-8d). Importantly, the highest mobility of the few layers WSe_2 FETs can reach up 350 $cm^2V^{-1}s^{-1}$, which represent the highest value observed in these atomically thin TMDs at room temperature,[25,32-37] further highlighting the high crystalline quality of these as-grown materials.

E. Discussion and summary

In summary, a systematic investigation on the chemical vapor deposition growth of large area p-type WSe_2 atomic layers was reported in this study. By systematically tuning the synthetic parameters, high quality monolayer WSe_2 thin film can be prepared over large area with the lateral dimensions up to ~1 cm^2. Micro-photoluminescence studies demonstrate uniform PL emission from the monolayer materials and the transmission electron microscopy studies confirms the excellent crystalline quality. Electrical transport studies further demonstrate the p-type WSe_2 back-gated field-effect transistors exhibit excellent electronic characteristics with hole mobility over 350 $cm^2V^{-1}s^{-1}$ and on/off ratio above 10^8. The availability of high quality large area p-type atomically thin materials offers an important building block for the design of future van de Waals heterostructures for electronic and photonic devices. This main ideas of this studied was published in title "Large Area Growth and Electrical Properties of p-Type WSe_2 Atomic Layers" at *Nano Lett* **15**, 709-713 (2015) and it has been cited for more than 78 times. This study had broad impact to 2D semiconducting materials morphology control, device performance optimization, layer dependent electrical properties of TMDs, etc. Also, the high-quality p-type WSe_2 inspire us to synthesize next step functional devices with epitaxial lateral WSe_2-WS_2 heterostructure, which will be discussed in the next chapter.

F. Figures and Legends

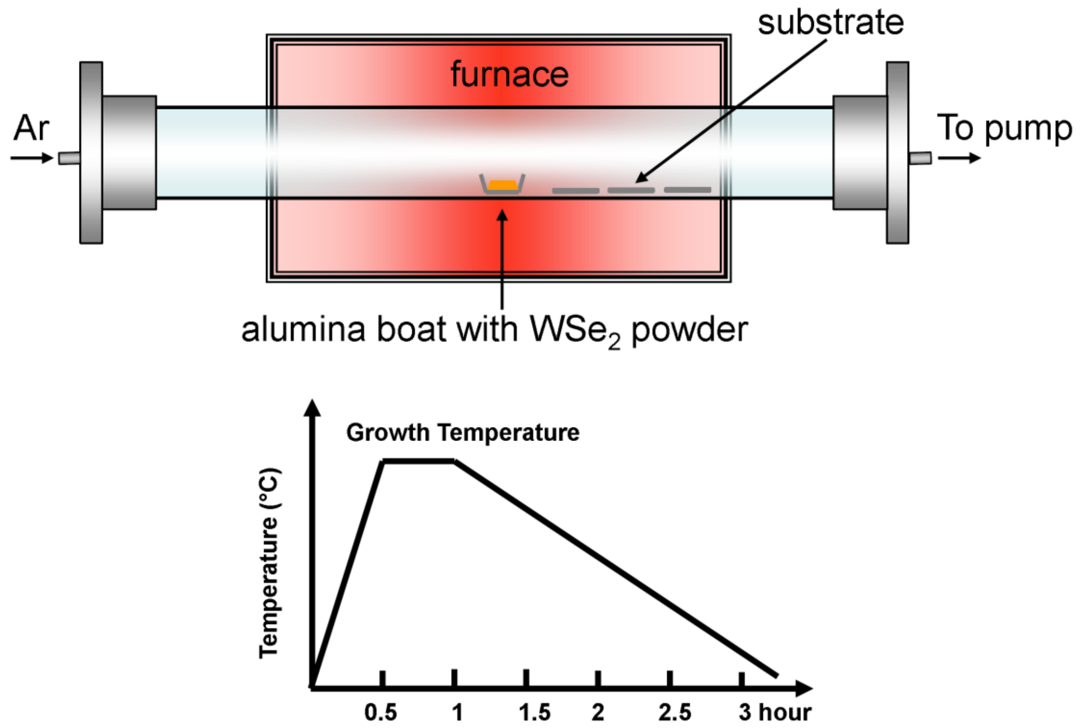

Figure 2-1. Schematic illustration of the growth equipment and recipe. **Up**: The WSe_2 powders are placed in an alumina boat at the center of the quartz tube, and the clean SiO_2/Si substrates designated for growth of WSe_2 atomic layers are leaved on the down-stream side. Argon is continuously supplied through the reactor with designed flow rate. **Down**: temperature control curve of source during growth.

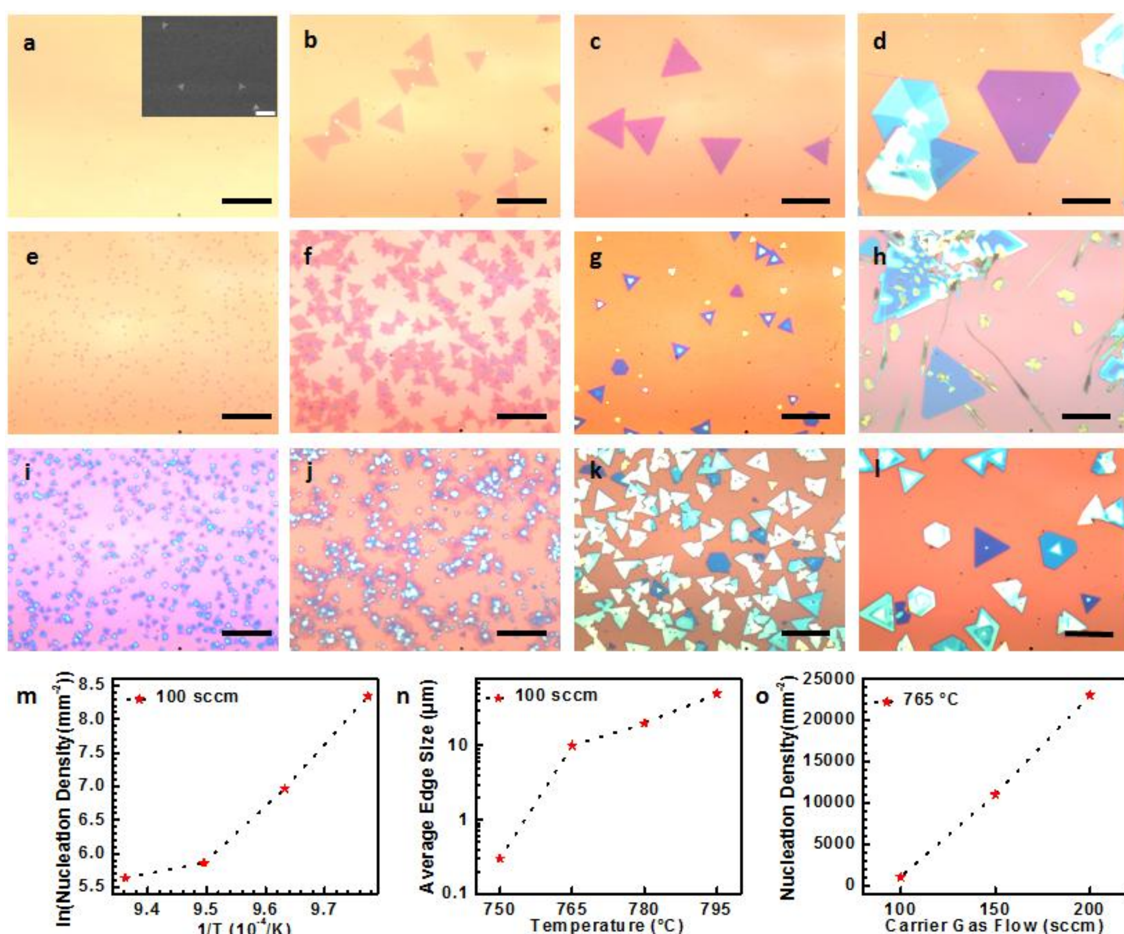

Figure 2-2. Reactor-conditions-dependent WSe_2 growth with varying temperature and flow rate of argon. Optical microscope images of WSe_2 samples grown at different temperature under designed flow rate for 20 min: **a,** 750 °C, 100 sccm, inset: SEM image of same size sample, indicating high density but small nucleations (~ 300 to 500 nm), scale bar of inset: 5μm; **b**, 765 °C, 100 sccm; **c**, 780 °C, 100 sccm; **d**, 795 °C, 100 sccm; **e**, 750 °C, 150 sccm; **f**, 765 °C, 150 sccm; **g**, 780 °C, 150 sccm; **h**, 795 °C, 150 sccm; **i**, 750 °C, 200 sccm; **j**, 765 °C, 200 sccm; **k**, 780 °C, 200 sccm; **l**, 795 °C, 200 sccm; All the scale bars are 20 μm. **m** and **n**, substrate temperature effect on nucleation density (**m**) and average edge size (**n**). **o**, nucleation density vs carrier gas flow relationship.

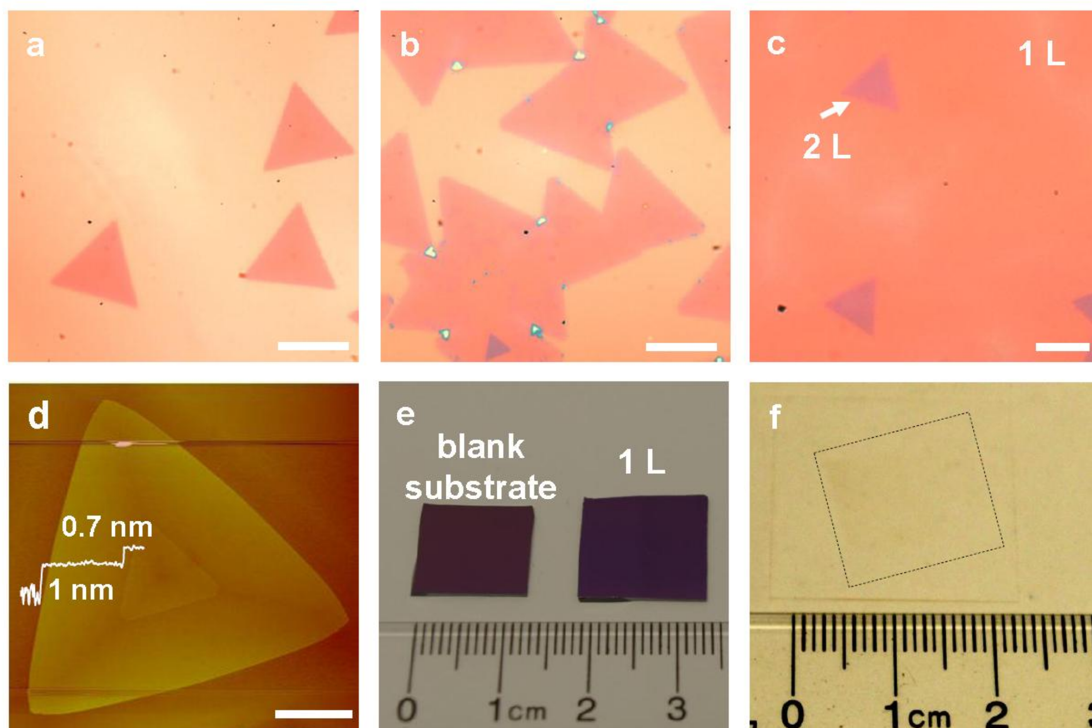

Figure 2-3. Time dependent growth of large area monolayer WSe_2 single crystal domains. **a**, A typical optical microscope images of the monolayer WSe_2 domains taken after 20 min of growth; **b**, 30 min of growth, and **c,** 40 min of growth. **d**, Atomic force microscope image of a WSe_2 monolayer and bilayer domains and their line scan profile. **e**, Photograph of the ~ 1 cm sized monolayer WSe_2 films obtained with 40 min growth time. Left: blank 300nm SiO_2/Si substrate; Right: fully covered WSe_2 monolayer on blank 300nm SiO_2/Si substrate. **f**, Photograph of the ~ 1 cm sized monolayer WSe_2 films transferred onto a glass template by chemical etching of SiO_2 layers. Scale bars of a-d are all 5 μm.

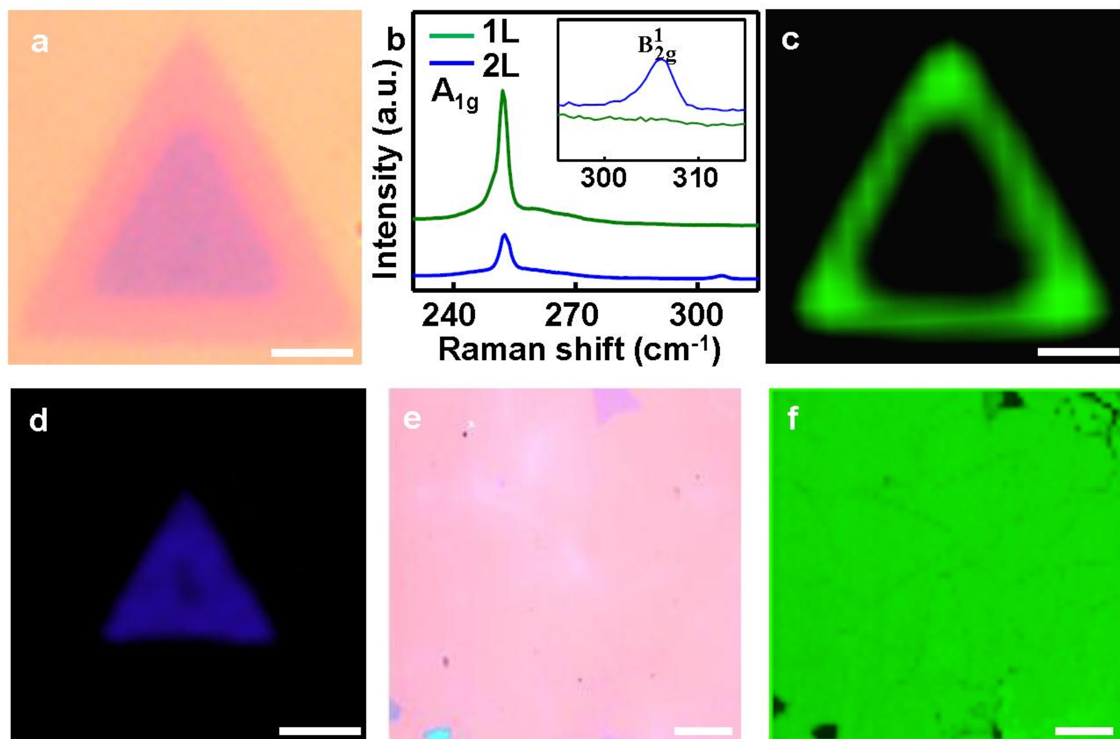

Figure 2-4. Micro-Raman investigation of the monodomain WSe_2. a, Optical microscope image of a typical monolayer WSe_2 with bilayer domain on the center. **b**, The Raman spectra of the monolayer and bilayer WSe_2. **c** and **d**, A typical Raman map of the single domain monolayer (**c**, center wavenumber: ~ 250 cm^{-1}) with bilayer (**d**, center wavenumber: ~ 307 cm^{-1}) WSe_2 domain; **e**, Optical microscope image of large scale monolayer WSe_2 with several bilayer or few-layer domain. **f**, Raman map of the large scale monolayer (center wavenumber: ~ 250 cm^{-1}) WSe_2 with several bilayer and few-layer domain. Scale bars of a,c,d are all 5 μm; Scale bars of e, f are 10um;

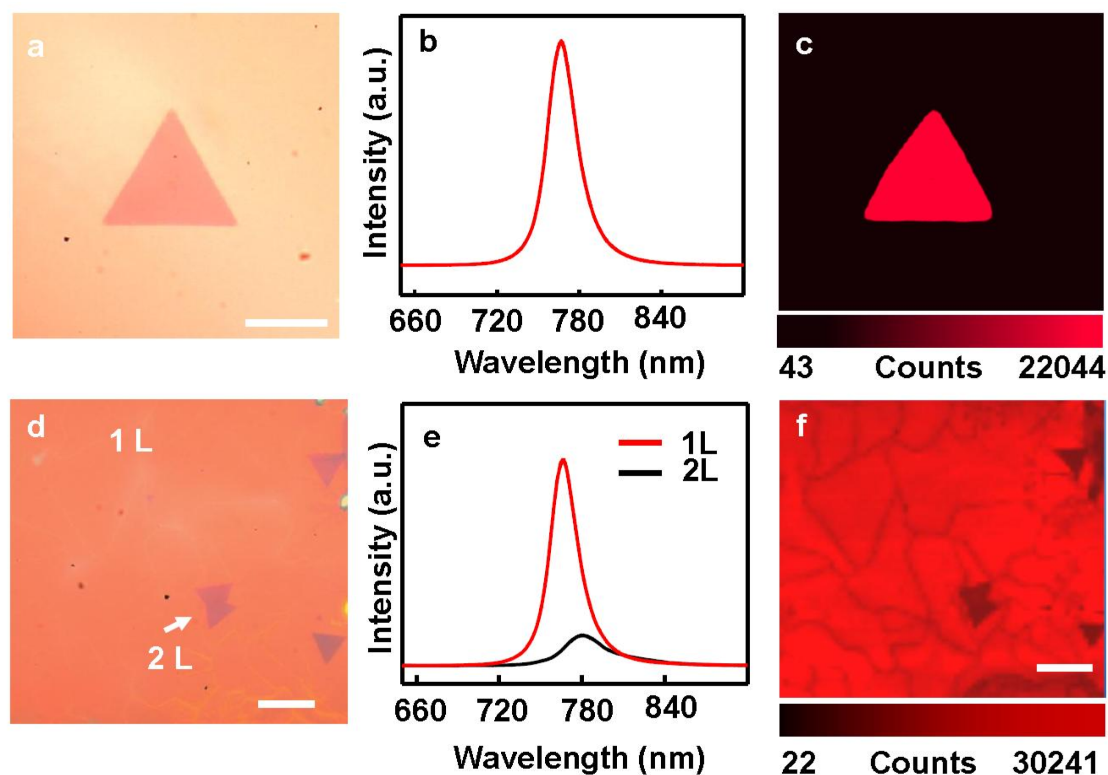

Figure 2-5. Optical properties of the single domain and fully covered WSe_2 monolayers. **a**, Optical microscope image of a typical monolayer WSe_2. Scale bar is 5 μm. **b**, PL spectra of the monolayer WSe_2 and Raman map **(c)**, of WSe_2 single domain showed in **(a)**. **d**, Optical microscope image of the full covered monolayer WSe_2 with some bilayer domains. Scale bar is 10 μm. **e**, PL spectra of the monolayer and bilayer WSe_2. **f**, Corresponding PL intensity map of the same region taken at panel D, Scale bar is 10 μm.

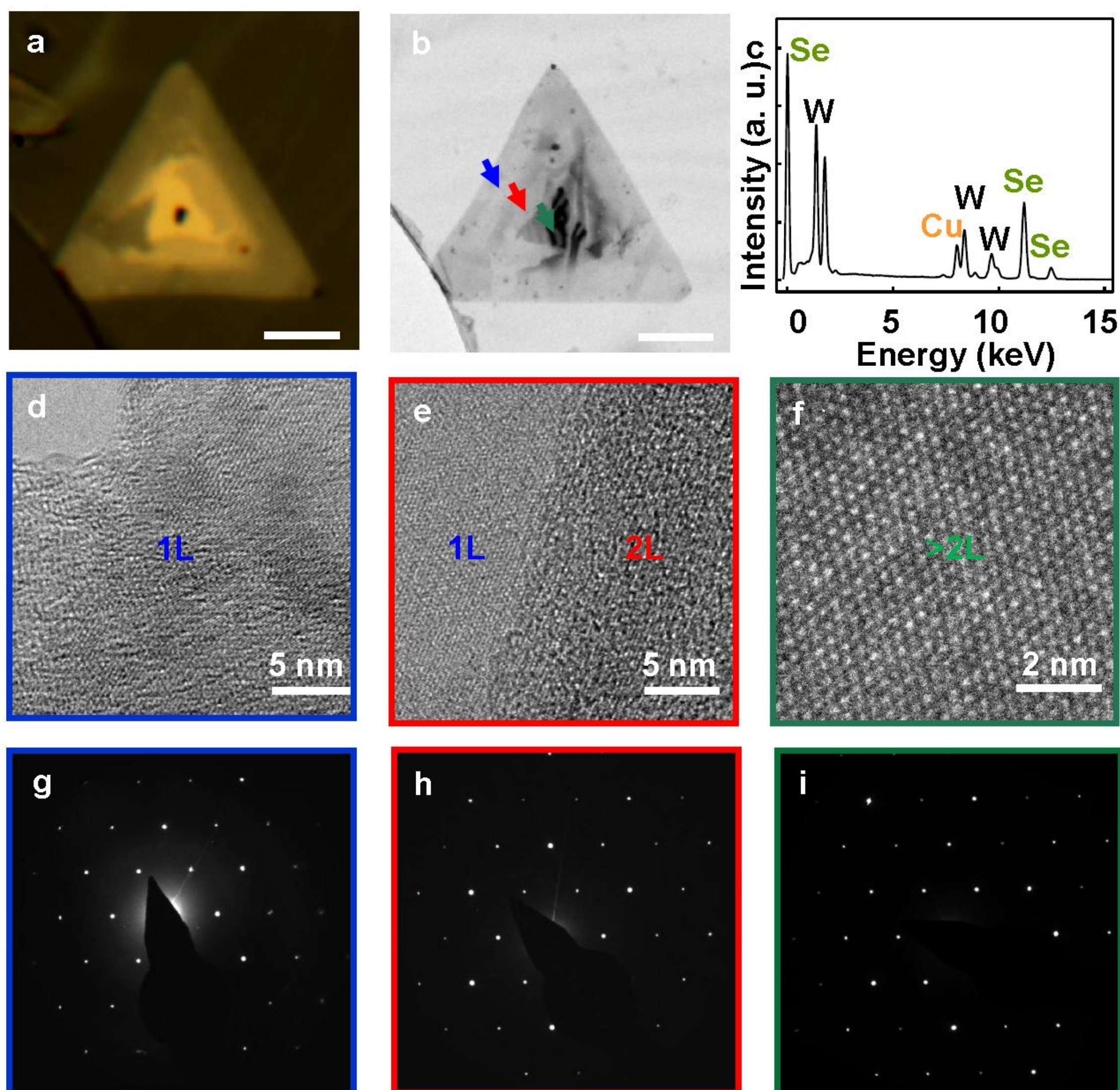

Figure 2-6. Crystalline structure characterization. a, Dark field optical microscope image of a typical monolayer WSe_2 with domain of few layers on the center. Scale bar is 10 μm. **b**, Low magnification bright field TEM image of a typical transferred WSe_2 triangular crystal; **c**, energy dispersive X-ray spectra showing the ratio between W and Se obtained from the integrated peak area is approximately 1:2. **d-f**, HRTEM images of the atomic structure of the WSe_2 monolayer **d**, bilayer **e**, and few layers. These images were taken on the regions indicated on the Figure **5b** by the arrows with blue, red, and dark cyan colors, respectively. Scale bar is 5 nm **d,e** and 2nm **f**. **g-i**, SAED pattern of the monolayer **g**, bilayer **h** and few-layer **i** WSe_2 with the zone axis of [0001], the six-fold symmetry in the position of the diffraction spots demonstrates that the triangular monolayer is predominantly single crystal with hexagonal structures.

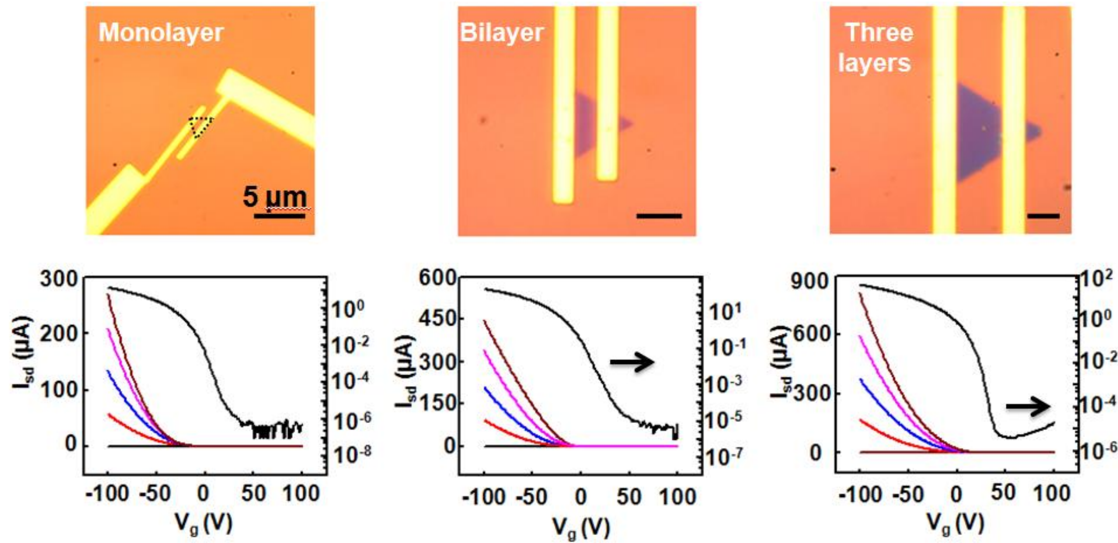

Figure 2-7. Electrical characteristics of the WSe_2 monodomains. Optical microscope image of **a** monolayer WSe_2 transistor (dashed line highlighted), **b** bilayer WSe_2 transistor, and **c** few-layer WSe_2 transistor, respectively. I_{sd}-V_g transfer characteristics plotted in **d**, **e**, and **f** of the device shown in panels **a**, **b**, and **c** at V_{sd} = 0.1, 0.2, 0.3, 0.4, and 0.5 V, respectively. All scale bars are 5 µm.

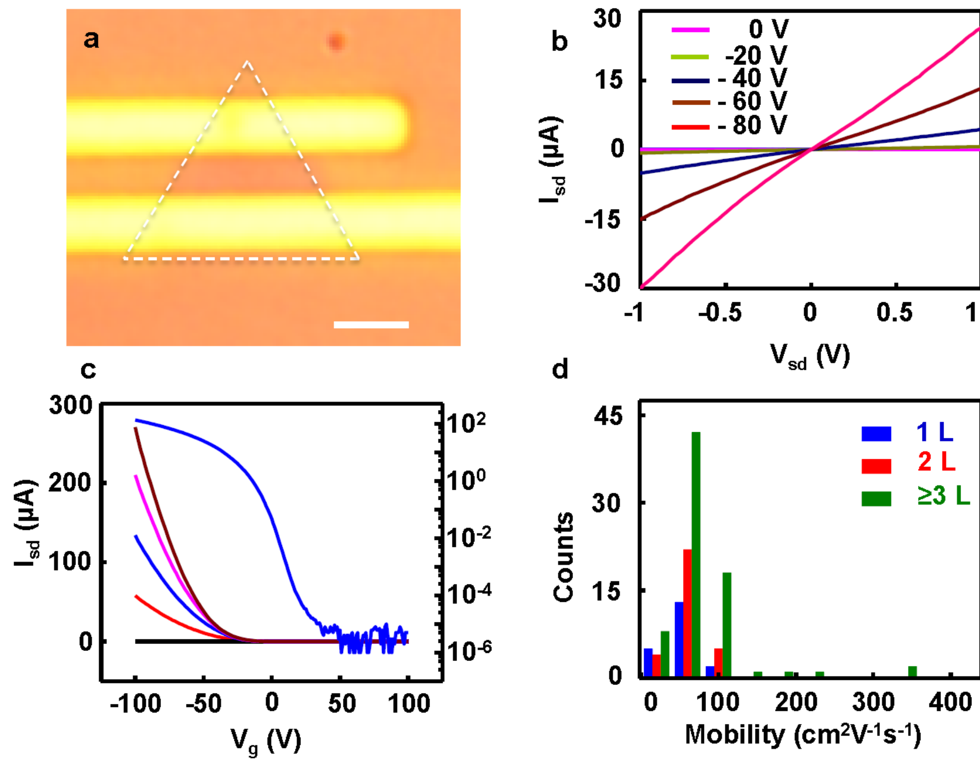

Figure 2-8. Electronic properties of WSe_2 atomic layers. a Optical microscope image of a monolayer WSe_2 transistor, Scale bar is 2 μm. **b**, I_{sd}-V_{sd} output characteristics of the WSe_2 transistor shown in panel A. **c**, I_{sd}-V_g transfer characteristics of the device shown in A at V_{sd} = 0.1, 0.2, 0.3, 0.4, and 0.5 V. **d**, A summary of the mobility values obtained in WSe_2 field effect transistors with different number of atomic layers, demonstrating a mobility range of 10 – 350 $cm^2V^{-1}s^{-1}$ and maximum on/off ratio over 10^8.

G. References

1. Novoselov, K. S. *et al.* A roadmap for graphene. *Nature* **490**, 192-200 (2012).

2. Schwierz, F. Graphene transistors. *Nat Nanotechnol* **5**, 487-496 (2010).

3. Bonaccorso, F., Sun, Z., Hasan, T. & Ferrari, A. C. Graphene photonics and optoelectronics. *Nat Photonics* **4**, 611-622 (2010).

4. Weiss, N. O. *et al.* Graphene: An Emerging Electronic Material. *Adv Mater* **24**, 5782-5825 (2012).

5. Liao, L. *et al.* High-speed graphene transistors with a self-aligned nanowire gate. *Nature* **467**, 305-308 (2010).

6. Bao, Q. L. & Loh, K. P. Graphene Photonics, Plasmonics, and Broadband Optoelectronic Devices. *Acs Nano* **6**, 3677-3694 (2012).

7. Lin, Y. M. *et al.* Wafer-Scale Graphene Integrated Circuit. *Science* **332**, 1294-1297 (2011).

8. Britnell, L. *et al.* Field-Effect Tunneling Transistor Based on Vertical Graphene Heterostructures. *Science* **335**, 947-950 (2012).

9. Yang, H. *et al.* Graphene Barristor, a Triode Device with a Gate-Controlled Schottky Barrier. *Science* **336**, 1140-1143 (2012).

10. Xia, F. N., Mueller, T., Lin, Y. M., Valdes-Garcia, A. & Avouris, P. Ultrafast graphene photodetector. *Nat Nanotechnol* **4**, 839-843 (2009).

11. Liu, Y. *et al.* Plasmon resonance enhanced multicolour photodetection by graphene. *Nat Commun* **2**, 579 (2011).

12. Mueller, T., Xia, F. N. A. & Avouris, P. Graphene photodetectors for high-speed optical

communications. *Nat Photonics* **4**, 297-301 (2010).

13. Splendiani, A. *et al.* Emerging Photoluminescence in Monolayer MoS2. *Nano Lett* **10**, 1271-1275 (2010).

14. Li, H. *et al.* Mechanical Exfoliation and Characterization of Single- and Few-Layer Nanosheets of WSe2, TaS2, and TaSe2. *Small* **9**, 1974-1981 (2013).

15. Tonndorf, P. *et al.* Photoluminescence emission and Raman response of monolayer MoS2, MoSe2, and WSe2. *Opt Express* **21**, 4908-4916 (2013).

16. Xu, Y. X. *et al.* One-step strategy to graphene/Ni(OH)(2) composite hydrogels as advanced three-dimensional supercapacitor electrode materials. *Nano Res* **6**, 65-76 (2013).

17. Terrones, H., Lopez-Urias, F. & Terrones, M. Novel hetero-layered materials with tunable direct band gaps by sandwiching different metal disulfides and diselenides. *Sci Rep-Uk* **3**, 1549 (2013).

18. Lee, Y. H. *et al.* Synthesis and Transfer of Single-Layer Transition Metal Disulfides on Diverse Surfaces. *Nano Lett* **13**, 1852-1857 (2013).

19. Kumar, A. & Ahluwalia, P. K. Electronic structure of transition metal dichalcogenides monolayers 1H-MX2 (M = Mo, W; X = S, Se, Te) from ab-initio theory: new direct band gap semiconductors. *Eur Phys J B* **85**, 186 (2012).

20. Najmaei, S. *et al.* Vapour phase growth and grain boundary structure of molybdenum disulphide atomic layers. *Nat Mater* **12**, 754-759 (2013).

21. Wang, Q. H., Kalantar-Zadeh, K., Kis, A., Coleman, J. N. & Strano, M. S. Electronics and optoelectronics of two-dimensional transition metal dichalcogenides. *Nat Nanotechnol* **7**, 699-712 (2012).

22. Yu, W. J. *et al.* Highly efficient gate-tunable photocurrent generation in vertical heterostructures of layered materials. *Nat Nanotechnol* **8**, 952-958 (2013).

23. Yu, W. J. *et al.* Vertically stacked multi-heterostructures of layered materials for logic transistors and complementary inverters. *Nat Mater* **12**, 246-252 (2013).

24. Zhu, C. F. *et al.* Single-Layer MoS2-Based Nanoprobes for Homogeneous Detection of Biomolecules. *J Am Chem Soc* **135**, 5998-6001 (2013).

25. Fang, H. *et al.* High-Performance Single Layered WSe2 p-FETs with Chemically Doped Contacts. *Nano Lett* **12**, 3788-3792 (2012).

26. Huang, J. K. *et al.* Large-Area Synthesis of Highly Crystalline WSe2 Mono layers and Device Applications. *Acs Nano* **8**, 923-930, doi:Doi 10.1021/Nn405719x (2014).

27. Burton, W. K. & Cabrera, N. Crystal Growth and Surface Structure .1. *Discuss Faraday Soc*, 33-39 (1949).

28. Liu, L. X. *et al.* High-Yield Chemical Vapor Deposition Growth of High-Quality Large-Area AB-Stacked Bilayer Graphene. *Acs Nano* **6**, 8241-8249 (2012).

29. Zhou, H. L. *et al.* Chemical vapour deposition growth of large single crystals of monolayer and bilayer graphene. *Nat Commun* **4**, 2096 (2013).

30. Liu, L. T., Kumar, S. B., Ouyang, Y. & Guo, J. Performance Limits of Monolayer Transition Metal Dichalcogenide Transistors. *Ieee T Electron Dev* **58**, 3042-3047 (2011).

31. Lee, Y. H. *et al.* Synthesis of Large-Area MoS2 Atomic Layers with Chemical Vapor Deposition. *Adv Mater* **24**, 2320-2325 (2012).

32. Huang, X., Zeng, Z. Y. & Zhang, H. Metal dichalcogenide nanosheets: preparation, properties and applications. *Chem Soc Rev* **42**, 1934-1946 (2013).

33. Zhan, Y. J., Liu, Z., Najmaei, S., Ajayan, P. M. & Lou, J. Large-Area Vapor-Phase Growth and Characterization of MoS2 Atomic Layers on a SiO2 Substrate. *Small* **8**, 966-971 (2012).

34. Liu, K. K. *et al.* Growth of Large-Area and Highly Crystalline MoS2 Thin Layers on Insulating Substrates. *Nano Lett* **12**, 1538-1544 (2012).

35. Larentis, S., Fallahazad, B. & Tutuc, E. Field-effect transistors and intrinsic mobility in ultra-thin MoSe2 layers. *Appl Phys Lett* **101** (2012).

36. Fang, H. *et al.* Degenerate n-Doping of Few-Layer Transition Metal Dichalcogenides by Potassium. *Nano Lett* **13**, 1991-1995, doi:Doi 10.1021/Nl400044m (2013).

37. Chuang, H. J. *et al.* High Mobility WSe2 p- and n-Type Field-Effect Transistors Contacted by Highly Doped Graphene for Low-Resistance Contacts. *Nano Lett* **14**, 3594-3601 (2014).

Chapter II: LATERAL EPITAXIAL GROWTH OF TWO-DIMENSIONAL LAYERED SEMICONDUCTOR WS_2-WSE_2 HETEROJUNCTIONS

A. Introduction to lateral TMD heterostructure

Inspired by the recent advancements in graphene, the layered transition metal dichalcogenides (TMDs) (*e.g.* WS_2 and WSe_2) have attracted considerable attention as two-dimensional (2D) semiconductors with unique layer-number dependent electronic and optical properties[1-15]. To explore the full potential of these layered semiconductors requires precise spatial modulation of the chemical, structural and electronic properties in these 2D atomic crystals to create well-defined heterostructures, much like the traditional semiconductor heterostructures that have essentially defined the foundation of all modern electronic and optoelectronic devices, including transistors, p-n diodes, photovoltaic/photodetection devices, light-emitting diodes and laser diodes. Although the graphene-boron nitride (BN) based 2D lateral heterostructures has been reported[16-18], the growth of TMD lateral heterostructures is of considerable challenge and has not been realized to date, despite the increasing efforts on the growth of diverse TMD nanosheets[19-23].

Here the compositionally modulated WS_2-WSe_2 lateral heterostructures can be prepared by *in situ* modulating the vapor phase reactants during growth of these 2D crystals was demonstrated. Raman and photoluminescence mapping studies demonstrate the resulting heterostructure nanosheets exhibit clear structural and optical modulation. Transmission electron microscopy and electron diffraction studies reveal a single crystalline structure, and the energy dispersive (X-ray) elemental mapping confirms spatial modulation of chemical

compositions in the heterostructure nanosheets. Electrical transport studies demonstrate that the WSe_2-WS_2 heterojunctions can form lateral p-n diodes with excellent current rectification behaviour and photocurrent generation characteristics, and can be used to create complementary metal-oxide semiconductor (CMOS) inverters with high voltage gain up to 24.

B. Lateral epitaxial growth strategy

It has been recently shown that a wide range of TMD material (e.g. MoS_2, $MoSe_2$, WS_2, WSe_2) can be directly grown on silicon oxide substrate in the form of single or few-layer well-faceted triangular or hexagonal domains or nearly continuous nanosheets[27-40]. The synthetic process usually involves a thermal chemical vapor deposition (CVD) process, in which the vapor phase reactants are generated by thermally evaporating the selected solid source material. With this approach, a lateral heterostructure can in principle be produced through successive growth of a second material (e.g., WSe_2) at the edge of an existing domain of a first material (e.g., WS_2). With a relatively small lattice mismatch (less than 4 %) between WS_2 and WSe_2, it is possible to produce coherent WS_2-WSe_2 heterostructures through a lateral epitaxial process. Although conceptually simple, the growth of TMD lateral heterostructures is of considerable challenge and has not been realized to date. Our studies indicate simple sequential growth often failed to produce the desired heterostructures because: (1) the edge growth front can be easily passivated after the termination of the first growth and exposure to ambient conditions, and cannot function as the effective nucleation sites for subsequent lateral epitaxial growth after transferred into a second growth chamber; and (2) the atomically thin TMD nanosheets are usually too delicate (e.g., far more volatile than graphene or BN) to withstand significant changes in growth temperature or conditions[41] that

are often necessary for the sequential growth of a second material to form the desired heterostructures.

To grow lateral heterostructures, it is therefore essential to design similar synthetic conditions applicable for both materials of interest and to retain a fresh, un-passivated edge growth front for successive lateral epitaxial growth. To this end, we have designed a thermal CVD process (Fig. 3-1) that can allow *in situ* switch of the vapor phase reactants to enable lateral epitaxial growth of single or few-layer TMD lateral heterostructures. The synthesis of WS_2-WSe_2 lateral heterostructures was carried in a home built CVD system that can allow *in situ* switch of solid chemical sources (Fig. 3-1). Two quartz boats with 0.4 g WS_2 powder (Alfa Aesar, 99.8%) or 0.6 g WSe_2 powder (Alfa Aesar, 99.8%) were loaded into a horizontal tube furnace with 1-inch quartz tube. A clean Si/SiO_2 substrate (~1×5 cm) was placed at downstream end of the furnace as the growth substrate. The system was pump-purged with ultra-high purity argon (Ar) gas (Rizhen, ~99.999%) then ramped to the desired growth temperature for the growth of WS_2 nanosheets at 1057 ^oC for 20 minutes under ambient pressure and a constant flow of 70 sccm Ar as the carrier gas. The furnace was then cooled down to 800 ^oC, and the boat with WS_2 powder was pushed out of the hot zone without breaking the vacuum, while the boat with WSe_2 powder was simultaneously pushed into the hot zone of the tube *in situ*. The temperature was then ramped to 1190 ^oC for the lateral epitaxial growth of WSe_2 for about 20 minutes under 5000 sccm Ar flow. Then the growth was terminated by shutting off the power of the furnace, and the sample was naturally cooled down to ambient temperature under 50 sccm Ar flow. For example, to produce a WS_2-WSe_2 heterostructure (Fig. 3-2), the WS_2 domains are first grown using a CVD process by

thermally evaporating a solid WS_2 source at the (center) hot zone of 1-inch tube furnace in an argon atmosphere (Fig. 3-1). The peripheral edges of the triangular domains feature unsaturated dangling bonds that function as the active growth front for the continued addition and incorporation of precursor atoms to extend the two-dimensional crystal in the lateral direction. By *in situ* moving WS_2 solid source out of the hot zone and WSe_2 solid source into the hot zone without exposing to the ambient conditions, the chemical vapor source is switched from WS_2 to WSe_2 in the middle of the growth to enable lateral hetero-epitaxial growth of WSe_2 at the peripheral active growth front to produce WS_2-WSe_2 lateral heterostructures.

C. Characterization of WS_2-WSe_2 lateral heterostructures

The resulting WS_2-WSe_2 lateral heterostructure domains mostly exhibit a well-faceted equilateral triangular geometry (*e.g.,* Fig. 3-3a and inset) with some truncated triangles or hexagons. Atomic force microscopy (AFM) studies show these 2D domains typically have a thickness of one to a few nanometers (*e.g.,* Fig. 3-3a), with a small number of thicker domains up to 10-50 nm in thickness. To probe the spatial structural and optical modulation in WS_2-WSe_2 heterostructures, we have conducted micro-Raman and micro-photoluminescence (micro-PL) studies using a confocal Raman microscope. Importantly, the Raman spectra (excited by 514 nm laser at 50 μW) taken from the centre and the peripheral regions of a triangular domain clearly show distinct features. The Raman spectrum from the centre region show two prominent peaks at 419.3 cm^{-1} and 355.4 cm^{-1} (blue line in Fig. 3-3b), corresponding to the A_{1g} and E^1_{2g} resonance modes of WS_2 [42, 43] ; while the Raman spectrum from the peripheral region show a single peak at 256.1 cm^{-1} (green

line in Fig. 3-3b), in agreement of the A_{1g} resonance mode of WSe_2 [43] . These micro-Raman studies demonstrate the co-existence of two distinct materials within the same triangular domain. The Raman mapping studies can further reveal the spatial modulation within the triangular domain, with the central part consisting a smaller triangular domain of WS_2 (Fig. 3-3d), and the peripheral region made of WSe_2 (Fig. 3-3e). A composite Raman mapping image shows seamless lateral integration of WS_2 and WSe_2 in the heterostructure domain (Fig. 3-3f). Similarly, micro-PL studies also show highly distinct PL peaks at ~665 nm for the centre part and ~775 nm for the peripheral part (Fig. 3-3c), consistent with the near band edge emission from WS_2 and WSe_2, respectively[20,42,44]. The PL mapping studies (Figs. 3-3g to 3i) show similar features to that of Raman mapping studies, further confirming the formation of WS_2-WSe_2 lateral heterostructures. Importantly, these Raman and PL mapping studies indicate that there is no apparent overlap or gap between WS_2 signal and WSe_2 signal (within the limit of optical resolution), suggesting that WS_2 inner triangle and WSe_2 surrounding areas are laterally connected, although the sharpness of the lateral heterostructures can not be accurately determined based on these optical studies.

To investigate the crystalline and microstructure modulation within the WS_2-WSe_2 lateral heterostructures, we have conducted transmission electron microscopy (TEM) and electron diffraction studies. For TEM studies, we have focused on smaller heterostructure domains for complete analysis of the entire domain. A low resolution TEM image of a multilayer triangular domain does not show obvious heterostructure interface (Fig. 3-4a). To better determine the lateral heterostructure interface, we have used high-angle annular dark-field (HAADF) TEM to image the triangular heterostructure domain (Fig. 3-4b). The HAADF

TEM is sensitive to the atomic number and shows a more clearly differentiable contrast in the triangular domain, with the slightly darker inner triangle corresponding to the WS_2 region, and the outer brighter region corresponding to WSe_2. The selected area electron diffraction (SAED) pattern taken across the heterostructure interface (Fig. 3-4c) shows apparently a single set of hexagonal arrangement of diffraction spots that can be indexed to the hexagonal symmetry of the [001] zone plane of WS_2 or WSe_2 lattice structures. The observation of single set of diffraction pattern suggesting the WS_2 or WSe_2 regions in the triangular heterostructure domain exhibit nearly the same lattice structure and the same lattice orientation. A magnified view of the diffraction spots reveal that each diffraction spot consists a pair of diffraction peaks. A careful analysis of these diffraction peaks yields (100) lattice plane spacing of 2.70 Å and 2.81 Å, in agreement with the values for both WS_2 and WSe_2 within the instrumental error[45]. A lattice resolved TEM image around the interface also further confirms the single crystalline structure. Importantly, the lattice fringes appear to be continuous across WS_2 region to WSe_2 region, indicating the heterostructure is nearly coherent (Fig. 3-4d).

To further unambiguously determine the chemical modulation across the lateral heterostructure interface, we have conducted elemental mapping of the triangular domain using energy dispersive X-ray spectroscopy (EDS). These elemental maps (mapping, same as before) show that tungsten (W) is nearly uniformly distributed throughout the entire triangular domain (Fig. 3-4e), while sulfur (S) and selenium (Se) show obvious modulation within the heterostructure domain, with S localized in the centre and Se localized in the peripheral area (Fig. 3-4f, 4g), respectively. A composite EDS mapping image of the S and

Se atoms further confirms seamless lateral integration of WS_2 and WSe_2 in the heterostructure domain (Fig. 3-4h). The EDS line scan profiles of the elemental distribution across the junction show clearly the opposite modulation of S and Se across the interface (Fig. 3-4i). It is noted that the junction is not atomically abrupt, but rather makes the transition from WS_2 to WSe_2 phases over a length scale of 35±5 nm. This gradual interface might be attributed to a relatively slow switching of the vapor phase reactants in the thermal CVD process and/or the ion diffusion across the interface during the high temperature synthetic process. It's noted the sub-40 nm transition region determined by EDS line scan is still limited by the TEM beam size and instrument limitation. Further study in similar system revealed that the transition region can be of an atomically sharp interline.[47]

D. Electronic characterizations and heterostructure devices

The above discussions clearly demonstrate the successful growth of lateral heterostructures of 2D layered TMDs. The formation of such 2D heterostructures with well defined composition or electronic modulation can open up exciting opportunities for the creation of a series of functional electronic and optoelectronic devices. Before constructing the functional devices across the heterostructure interface, we have first characterized the basic electrical transport properties of WS_2 and WSe_2, respectively. To this end, the WS_2 and WSe_2 field-effect transistors (FETs) were fabricated on Si/SiO_2 substrate, with Ti/Au thin film as the source-drain contacts for WS_2, and Au thin film as the contacts for WSe_2, and the silicon substrate as the back gate electrode. To electrically access the inner WS_2 triangle without being shorted to the peripheral WSe_2, a 50-nm thick Al_2O_3 thin film was deposited on part of the peripheral WSe_2 to insulate it from the contact electrodes to centre WS_2. Fig. 3-5a

and 3-5b show the I_{ds}-V_{ds} characteristics at varying back gate voltage for WS_2 and WSe_2, respectively. A linear I_{ds}-V_{ds} relationship is clearly observed for both WS_2 and WSe_2, indicating the metal contact barrier does not significantly affect the intrinsic device behavior. The formation of low-barrier contacts for both WS_2 and WSe_2 is very important for probing the intrinsic electronic and optoelectronic characteristics of the lateral heterojunction devices. The I_{ds}-V_{ds} plots at varying back gate voltages show that the current increases with increasing positive gate voltage for WS_2 (Fig. 3-5a), indicating an n-type semiconductor behavior. On the contrary, the current increases with increasing negative gate voltage for WSe_2 (Fig. 3-5b), demonstrating a *p*-type behavior. It is also noted that *n*-type WS_2 is in the normally "off" state at zero gate with a relatively large positive turn-on voltage (~40V), indicating a low intrinsic electron doping; while the p-type WSe_2 is normally "on", suggesting a relatively high hole-doping concentration. We have also evaluated the carrier mobility in these synthetic materials based FET measurements. The electron mobility in WS_2 is in the range 10-20 cm^2/Vs, and the hole mobility in WSe_2 is in the range of 30-100 cm^2/Vs, both of which are comparable to best values for the respective synthetic materials reported to date.

With well-defined *p*-type characteristics in WSe_2 and *n*-type characteristics in WS_2, the WSe_2-WS_2 lateral heterostructure forms a natural heterojunction *p-n* diode (Fig. 3-5c, inset). Electrical transport studies across a heterojunction device show obvious current rectification behavior in the I_{ds}-V_{ds} plot (Fig. 3-5c), with current only being able to pass through the device when the *p*-type WSe_2 is positively biased. The observation of current rectification clearly demonstrates a *p-n* diode is formed within the WSe_2-WS_2 lateral heterostructure. The ultrathin nature of the heterojunction allows gate tunability of the diode characteristics. The

diode output characteristics (I_{ds}-V_{ds}) under different back gate voltage show that the output current increases with increasing positive gate voltage, suggesting that the *n*-type WS_2 is partly limiting the charge transport in the device. This is consistent with the electrical transport properties of WS_2 and WSe_2, in which WS_2 is much lower doped and therefore dominates the charge transport across the lateral heterojunction *p-n* diode.

The *p-n* diodes form the fundamental basis for many functional devices, including photodiodes. To this end, we have also investigated the photocurrent response of our lateral heterojunction p-n diodes as photodiodes. The I_{ds}-V_{ds} measurements of a multilayer heterojunction p-n diode with and without laser illumination (514 nm, 30 nW) show clear photovoltaic effect with an open-circuit voltage of ~0.47 V and a short-circuit current of ~ 1.2 nA (Fig. 3-5d). In general, the photoresponse exhibits a rapid temporal response beyond our experimental time resolution of 100 μs (Fig. 3-5d, inset), demonstrating that the photoresponse is indeed originated from photocarrier generation and separation rather than any other extrinsic effects. Based on the photocurrent response and total input laser power, we can determine the external quantum efficiency (EQE) of the photon to electron conversion to be ~9.9 %. After determining the optical absorption of the multilayer heterostructure device (~23%), we can estimate an internal quantum efficiency of ~43%. Lastly, the photocurrent mapping clearly shows that the photocurrent response is localized to the lightly doped WS_2 and WS_2-WSe_2 interface region near the centre of the triangular domain (Fig. 3-5e), confirming that the depletion layer is largely localized to the lightly doped WS_2 in the lateral heterojunction diodes.

The preparation of WS_2-WSe_2 lateral heterostuctures with both *p*- and *n*-type characteristics can also allow us to construct many other functional devices. For example, a CMOS inverter (a logic NOT gate) can be constructed by integrating a *p*-channel WSe_2 and an *n*-channel WS_2 transistors in series across the heterojunction interface (Fig. 3-5f, insets). To reduce the required gate voltage, the CMOS inverter was fabricated by using 20 nm HfO_2 as the gate dielectrics. The output–input (V_{out}–V_{in}) voltage response of the inverter shows constant high voltage output at low input (black curve in Fig. 3-5f). When the input is increased to about 1.5 V, the output voltage is quickly switched to nearly 0 V and maintains a low state at higher input voltages. Significantly, the CMOS inverter can readily exhibit a high voltage gain. Differentiation of the measured V_{out}–V_{in} relation reveals a voltage gain as large as 24 (red curve in Fig. 3-5f). Such a large gain can be particularly beneficial for interconnection of arrays of logic circuits for functional electronic applications without the need for signal restoration at each stage.

E. Discussion and summary

In summary, we have successfully demonstrated the growth of lateral heterojunctions of 2D layered semiconductors through a lateral hetero-epitaxial approach. Although the lateral heterojunctions between *h*-BN and graphene (or between intrinsic and substitutionally doped graphene) have been reported previously[23-26,46], they usually exhibit limited functions due to the semimetal nature of graphene and insulator nature of *h*-BN. The realization of lateral heterojunction in the 2D layered semiconductors can open up exciting opportunities for creating a wide range of functional devices, ranging from the complementary logic circuits, photovoltaics, photo-detectors, to light-emitting diodes and laser diodes.

Beyond the typical 2D layered semiconductors, this approach may be extended for the creation of heterojunctions among many other 2D materials with diverse physical properties, including superconducting (*e.g.* $NbSe_2$), magnetic (*e.g.* $CrSe_2$) and topologically insulating (*e.g.* Bi_2Se_3, Bi_2Te_3) materials. It thus has the potential to enable seamless integration of these highly distinct physical properties, creating well-defined spatial modulation of chemical compositions and electronic properties in these 2D atomic crystals. With further development in future studies, the lateral epitaxial approach may be extended for the growth of superlattice structures of two or more 2D layered materials for further complexity and functions, and the size of the lateral "*interface*" in such atomically thin heterostructures may be eventually reduced to a single atomic line between two distinct 2D materials to form an "*interline*". With the quantum confinement in two dimensions at the "*interline*" and the importance of interface in semiconductor heterojunctions and topological insulators, the formation of the "*interline*" in the ultrathin lateral heterostructures could open up a new door to exotic physics and/or totally new device concepts.

The main idea of this study was published in title "Lateral epitaxial growth of two-dimensional layered semiconductor heterojunctions" at *Nature Nanotechnology* **9**, 1024-1030 (2014) and this publication have been cited for more than 223 times with broad impact of 2D lateral heterojunction epitaxial growth, lateral heterojunction demonstration, further lateral superlattice structure and device development. One interesting thing is that two similar studies was published in *Nature Materials* at the same week, indicating the urgency and significance of those demonstration and also the beauty to probe the border of human knowledge with the whole community endeavour.[48, 49] Furthermore, the electrical properties

of TMDs can be well controlled by tuning the chemical composition ratio of n-type WS_2 and p-type WSe_2, which will be discussed in next chapter.

F. Method Summary

Synthesis. The syntheses of lateral heterostructures were conducted in home-built-CVD systems using thermally evaporated vapor phase reactants from solid source materials at atmospheric pressure. The CVD systems are designed to allow for *in situ* switch of chemical vapour sources by mechanically shifting the selected solid source materials into and out of the hot zone, which is essential for retaining the active growth front for the sequential hetero-epitaxial growth. For the growth of WS_2-WSe_2, WS_2 and WSe_2 powders were directly used the solid source;

Characterizations. The microstructures and morphologies of the nanostructures are characterized by optical microscope, atomic force microscope (AFM), and transmission electron microscope (TEM). The micro-Raman and micro-PL studies were conducted using a Horiba LabRAM HR Evolution confocal Raman system with an Ar ion laser (514 nm) excitation. The WS_2-WSe_2 heterojunction devices were fabricated using electron-beam lithography followed by electron-beam deposition of metal thin films. Ti/Au (5/50 nm) was used as the contact electrodes for WS_2 and Au (50 nm) for WSe_2. The electrical transport measurements were conducted in a Lakeshore probe station, with a computer-controlled analogue-to-digital converter and a low noise current pre-amplifier. The scanning photocurrent measurements were conducted with the same Horiba confocal Raman system combined with the same electrical measurement system.

Microscopic, optical, electrical and optoelectrical characterizations. The microstructures and morphologies of the heterostructures are characterized by an optical microscope, JEOL 6700 SEM, and an FEI TEM, STEM (line scan: beam size 3 nm and step size 7 nm). The confocal micro-PL and micro-Raman measurements were conducted using a Horiba LabRAM HR Evolution confocal Raman system with 1800 g/mm grating, 50× diffraction-limited objective (N.A.=0.75), with an Ar ion laser (514 nm) excitation. To fabricate WS_2-WSe_2 heterojunction device, the metal electrodes (for probe contact or wire bonding purposes) were patterned using electron-beam lithography followed by electron-beam deposition of metal thin films. Ti/Au (5/50 nm) was used as the contact electrodes for WS_2 and Au (50 nm) for WSe_2. The D.C. electrical transport measurements were conducted in a Lakeshore probe station (Model TTP4), with a computer-controlled analogue-to-digital converter (National Instruments model 6030E) and a low noise current pre-amplifier (Stanford Research Systems SR570). The scanning photocurrent measurements were conducted with the same Horiba LabRAM HR Evolution confocal Raman system combined with the same electrical measurement system.

G. Figures and Legends

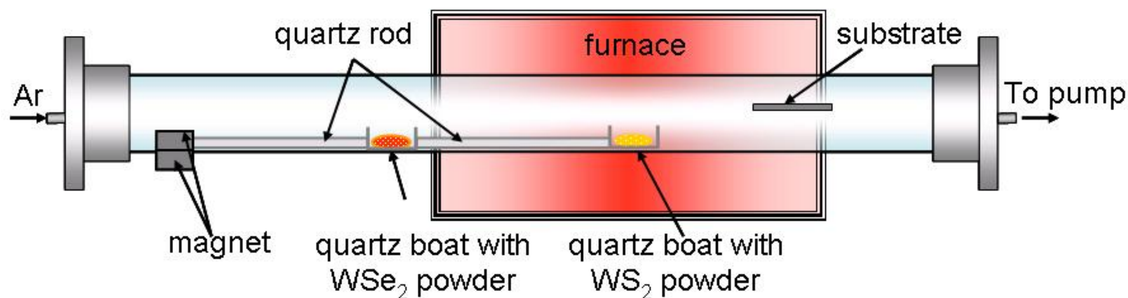

Figure 3-1. Schematic illustration of the home-built CVD system for the growth of WS_2-WSe_2 lateral heterostructures. The WS_2 powder and WSe_2 powder was directly used as the solid source. Two magnets (one inside the CVD chamber and one outside) was used to mechanically push the WS_2 solid source out of and WSe_2 solid source into the centre hot zone without breaking vacuum. This *in situ* switch of chemical source is essential for retaining the active edge growth front for sequential epitaxial growth of WS_2-WSe_2 lateral heterostructures.

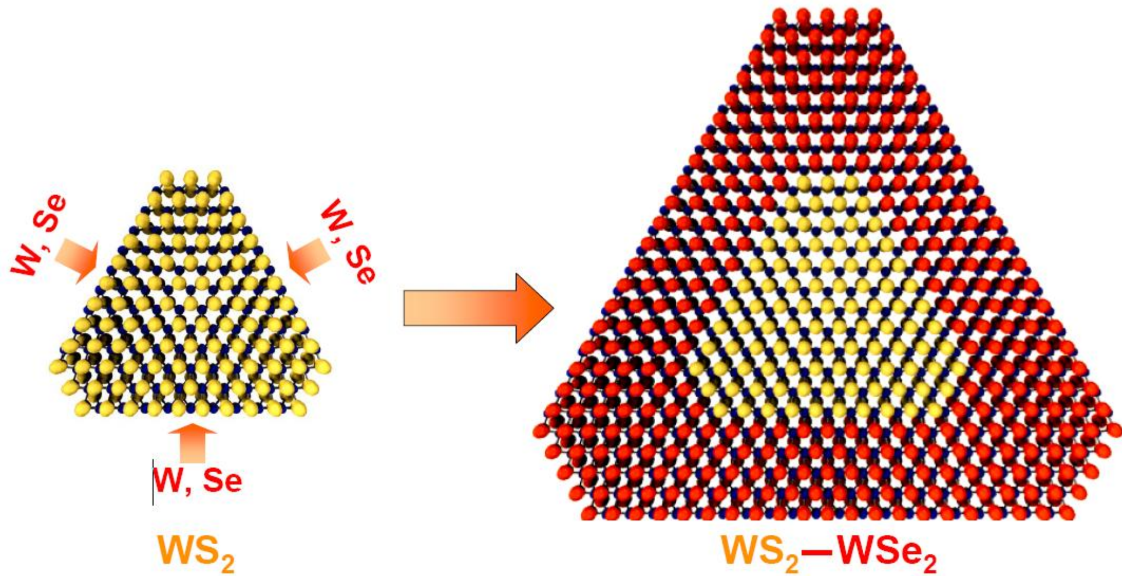

Figure 3-2. Schematic illustration of lateral epitaxial growth WS_2-WSe_2 heterostructures. A triangular domain of WS_2 is first grown using a chemical vapor deposition process. The peripheral edges of the triangular domain features unsaturated dangling bonds that function as the active growth front for the continued addition and incorporation of precursor atoms to extend the two-dimensional crystal in the lateral direction. With an *in situ* switch of the chemical vapor source for WSe_2 during the middle of the growth, lateral hetero-epitaxial growth can occur at the peripheral active growth front to form WS_2-WSe_2 lateral heterostructures.

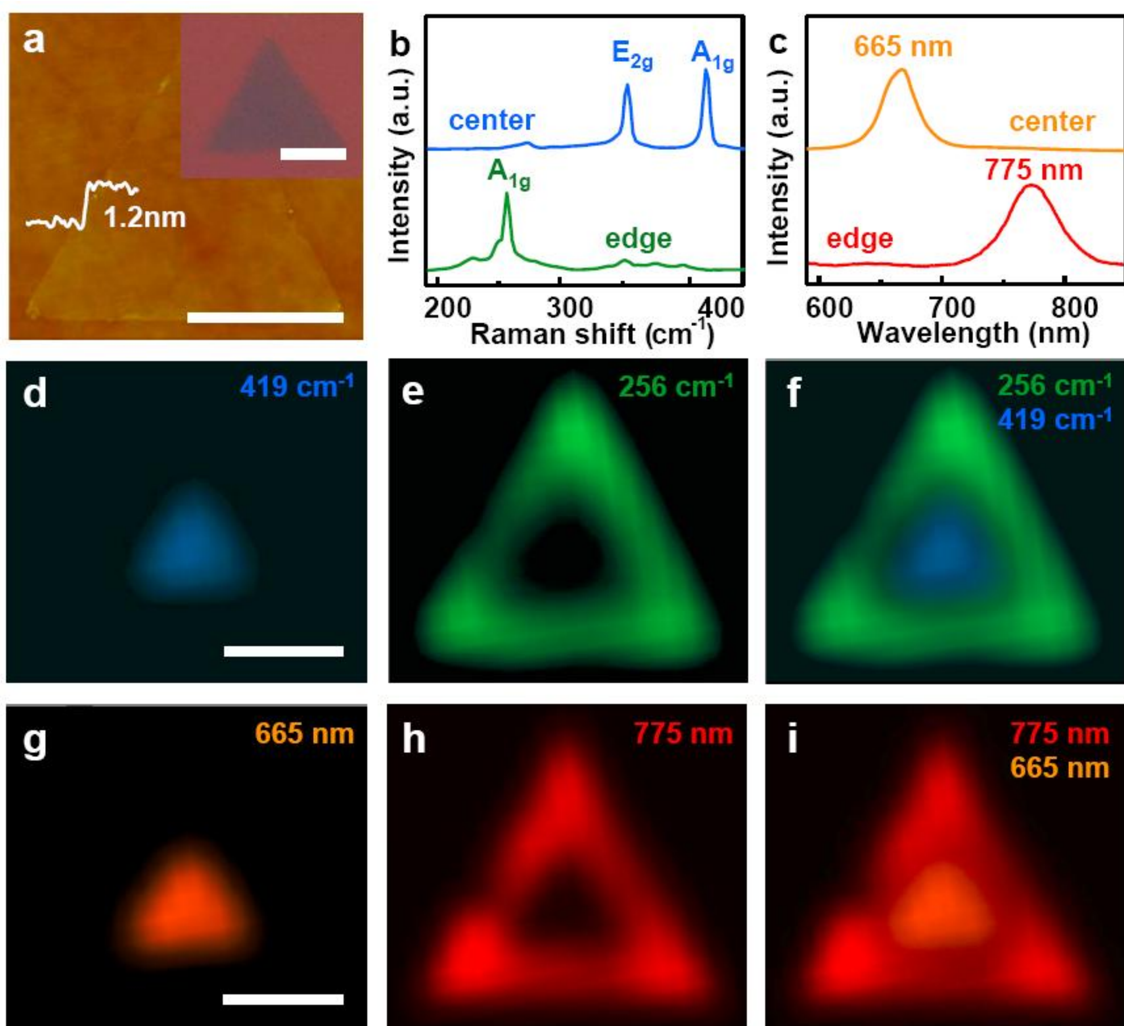

Figure 3-3. The AFM, Raman and photoluminescence (PL) characterizations of WS_2-WSe_2 lateral heterostructures. **a,** AFM image of a triangular domain with a thickness of 1.2 nm. The inset shows an optical image of a triangular domain. The scale bars equal to 5 μm. **b**, The Raman spectra of a heterostructures domain. The blue curve is obtained from the centre region, showing the characteristic Raman peak of WS_2; the green curve is obtained from the peripheral region, showing the characteristic Raman peak of WSe_2. **c**, The PL spectra of a heterostructures domain. The orange curve is obtained from the centre region with the characteristic PL peak of WS_2, and the red curve is obtained from the peripheral region with the characteristic PL peak of WSe_2. **d**, Raman mapping at 419 cm^{-1} (WS_2 A_{1g} signal) demonstrates that WS_2 is localized to the centre region of triangular domain. The scale bar is 5 μm. **e**, Raman mapping at 256 cm^{-1} (WSe_2 A_{1g} signal) demonstrates WSe_2 is located in the peripheral region of triangular domain. **f**, A composite image consisting of the Raman mapping at 255 cm^{-1} and 417 cm^{-1} shows no apparent overlap or gap between the WS_2 signal and WSe_2 signal, demonstrating that WS_2 inner triangle and WSe_2 peripheral areas are laterally connected. **g**,**h**, PL mapping images at 665 nm and 775nm show characteristic PL emission of WS_2 and WSe_2 in the centre and peripheral region of the triangular domain. The scale bar is 5 μm. **i**, A composite image consisting of the PL mapping at 665 nm and 775 nm demonstrates the formation of WS_2-WSe_2 lateral heterostructures, consistent with Raman mapping studies.

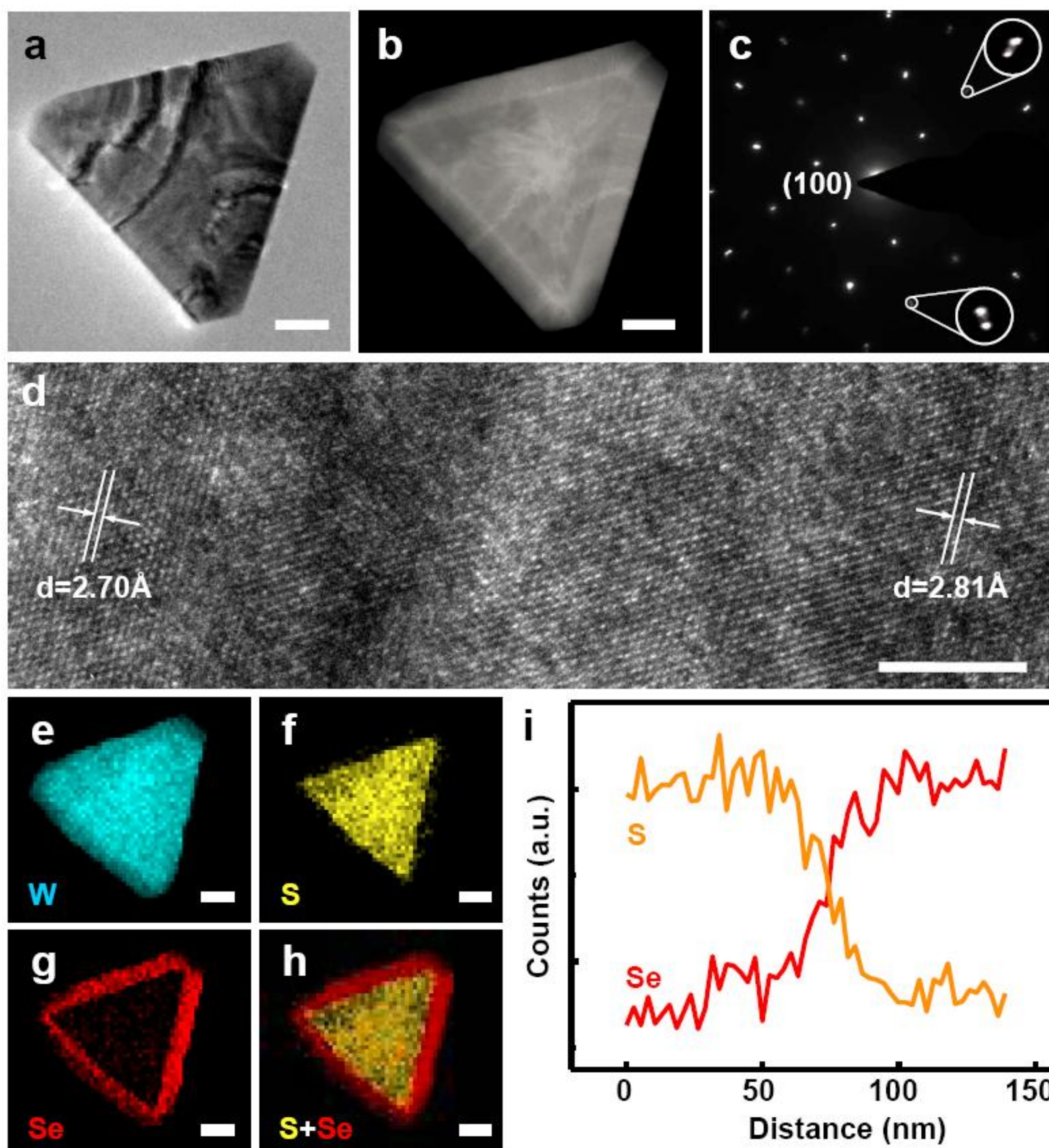

Figure 3-4. Structural and chemical modulation in WS_2-WSe_2 lateral heterostructures. a, TEM image of a triangular domain of WS_2-WSe_2 lateral heterostructure. The scale bar is 200 nm. **b**, High-angle annular dark-field (HAADF) TEM image of the heterostructure domain shows the slightly darker inner triangle corresponding to the WS_2 region, and the slightly brighter outer region corresponding to WSe_2. The scale bar is 200 nm. **c,** The electron diffraction pattern taken across the heterostructure interface, with each diffraction spot consisting of a pair diffraction peaks (see insets for the magnified view), with the indexed lattice spacing of 2.70 Å for WS_2 and 2.78 Å for WSe_2, respectively. **d**, High-resolution TEM image show highly crystalline structure with continuous lattice fringes across the WS_2-WSe_2 heterostructure interface. The scale bar is 5 nm. **e**, **f**, **g**, Energy dispersive X-ray spectroscopy (EDS) elemental (mapping) of W, S and Se atoms show relative uniform distribution of W, and clear modulation of S and Se in the triangular domain. **h**, Composite EDS mapping image of S and Se atoms shows seamless lateral integration of WS_2 and WSe_2 in the heterostructure domain. The scale bars in **e-h** are 200 nm. **i**, The EDS line scan

profiles of Se and S distribution show opposite modulation (Se counts increased as S counts is decreasing) across the heterostructure interface.

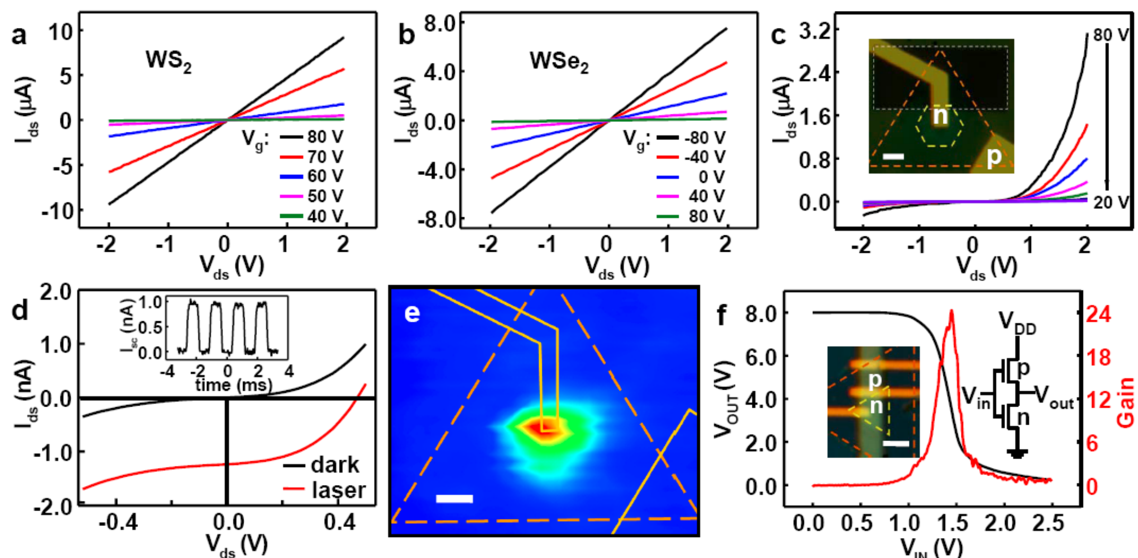

Figure 3-5. Electrical characterizations and functional devices from WS_2-WSe_2 lateral heterojunctions. a, The I_{ds}-V_{ds} output characteristics of WS_2 FET at various back gate voltages (indicated in the plot) show increasing current with increasing positive gate voltage, demonstrating *n*-type behaviour. **b,** The I_{ds}-V_{ds} output characteristics of WSe_2 FET at various back gate voltages (indicated in the plot) show decreasing current with increasing positive gate voltage, demonstrating *p*-type behaviour. **c,** Gate-tunable output characteristics of a lateral WSe_2-WS_2 heterojunction *p*-*n* diode. The gate voltage varies from 80 to 20 V in the steps of 10 V as indicated in the plot. The inset shows an optical image of a heterojunction *p*-*n* diode device. The orange dashed line outlines the triangular heterostructure domain, and the white dashed line outlines the 50-nm Al_2O_3 deposited on WSe_2 for insulation with the WS_2 contact electrodes. The scale bar is 2 μm. **d,** Experimental output (I_{ds}-V_{ds}) characteristics of the lateral WSe_2-WS_2 heterojunction p-n diode in the dark (black) and under illumination (wavelength: 514 nm; power, 30 nW). Inset, temporal photocurrent response under periodic on/off laser illumination through a mechanical chopper. **e,** Scanning photocurrent map of the lateral WSe_2-WS_2 heterojunction *p*-*n* diode show photo-response is localized to the WSe_2-WS_2 interface and the lower doped WS_2 region near the centre of the triangular domain. The orange dashed line outlines the triangular heterostructure domain. The golden solid line outlines the gold electrodes. The scale bar is 2 μm. **f,** A CMOS inverter obtained by integrating a *p*-type WSe_2 and an *n*-type WS_2 FET shows the expected inverter function with a voltage gain as large 24. The black curve is the output-input curve and the red curve indicates the voltage gain. The inset shows the image and circuit diagram of the WSe_2-WS_2 CMOS inverter. The scale bar is 2 μm.

H. References

1. Novoselov, K. S. *et al.* Two-dimensional atomic crystals. *Proc. Natl Acad. Sci. USA* **102**, 10451-10453 (2005).

2. Mak, K. F., Lee, C., Hone, J., Shan, J. & Heinz, T. F. Atomically thin MoS_2: A new direct-gap semiconductor. *Phys. Rev. Lett.* **105**, 136805 (2010).

3. Splendiani, A. *et al.* Emerging photoluminescence in monolayer MoS_2 *Nano Lett.* **10**, 1271-1275 (2010).

4. Eda, G. *et al.* Photoluminescence from chemically exfoliated MoS_2. *Nano Lett* **11**, 5111-5116(2011).

5. Radisavljevic, B., Radenovic, A., Brivio, J., Giacometti, V. & Kis, A. Single-layer MoS_2 transistors. *Nat. Nanotechnol.* **6**, 147-150 (2011).

6. Wang, Q. H., Kalantar-Zadeh, K., Kis, A., Coleman, J. N. & Strano, M. S. Electronics and optoelectronics of two-dimensional transition metal dichalcogenides. *Nat. Nanotech.* **7**, 699-712 (2012).

7. Geim, A. K. & Grigorieva, I. V. Van der Waals heterostructures. *Nature* **499**, 419-425 (2013).

8. Chhowalla, M. *et al.* The chemistry of two-dimensional layered transition metal dichalcogenide nanosheets. *Nat. Chem.* **5**, 263-275 (2013).

9. Huang, X.; Zeng, Z. Y. & Zhang, H. Metal dichalcogenide nanosheets: preparation, properties and applications. *Chem. Soc. Rev*. **42**, 1934-1946 (2013).

10. Britnell, L. *et al.*Field-effect tunneling transistor based on vertical graphene heterostructures. *Science* **335**, 947-950 (2012).

11. Yu W. J. *et al.* Vertically stacked multi-heterostructures of layered materials for logic transistors and complementary inverters. *Nat. Mater.* **12**, 246-252 (2013).

12. Roy, K. *et al.*Graphene-MoS_2 hybrid structures for multifunctional photoresponsive memory devices. *Nat. Nanotechnol.* **8**, 826-830 (2013).

13. Britnell, L. *et al.*Strong light-matter interactions in heterostructures of atomically thin films. *Science* **340**, 1311-1314 (2013).

14. Yu W. J. *et al.* Highly efficient gate-tunable photocurrent generation in vertical heterostructures of layered materials. *Nat. Nanotechnol.* **8**, 952-958 (2013).

15. Mak, K. F. *et al.*Ultrasensitive photodetectors based on monolayer MoS_2. *Nat. Nanotechnol.* **8**, 497-501 (2013).

16. Jones, A. M. *et al.*Spin-layer locking effects in optical orientation of exciton spin in bilayer WSe_2. *Nat. Phys.* **10**, 130-134 (2014).

17. Sundaram, R. S. *et al.*Electroluminescence in single layer MoS_2. *Nano Lett.* **13**, 1416-1421 (2013).

18. Baugher, B. W. H., Churchill, H. O. H., Yang, Y. & Jarillo-Herrero, P. Optoelectronic devices based on electrically tunable p-n diodes in a monolayer dichalcogenide. *Nat. Nanotechnol.* **9**, 262-267 (2014).

19. Pospischil, A., Furchi, M. M., Mueller, T. Solar-energy conversion and light emission in an atomic monolayer p-n diode. *Nat. Nanotechnol.* **9**, 257–261 (2014).

20. Ross, J. S. *et al.*Electrically tunable excitonic light-emitting diodes based on monolayer WSe_2 p-n junctions. *Nature Nanotechnol.* **9**, 268-272 (2014).

21. Lopez-Sanchez, O. *et al.* Light generation and harvesting in a van der Waals heterostructure. *ACS Nano* **8**, 3042-3048 (2014).

22. Zhang, Y., Oka, T., Suzuki, R., Ye, J. & Iwasa, Y. Electrically switchable chiral light-emitting transistor. *Science* **344**, 725-728 (2014).

23. Levendorf, M. P. *et al.* Graphene and boron nitride lateral heterostructures for atomically thin circuitry. *Nature* **488,** 627-632 (2012).

24. Liu, Z. *et al.* In-plane heterostructures of graphene and hexagonal boron nitride with controlled domain sizes. *Nat. Nanotechnol.* **8,** 119-124 (2013).

25. Lei, L. *et al.* Heteroepitaxial growth of two-dimensional hexagonal boron nitride templated by graphene edges. *Science* **343,** 163-167 (2014).

26. Jiong, L. *et al.* Order-Disorder Transition in a Two-Dimensional Boron-Carbon-Nitride Alloy, *Nat. Commun.* **4**, 3681 (2013).

27. Lee, Y. H.*et al.* Synthesis of large-area MoS_2 atomic layers with chemical vapor deposition. *Adv. Mater.* **24**, 2320-2325 (2012).

28. Liu, K. K. *et al.* Growth of large-area and highly crystalline MoS_2 thin layers on insulating substrates. *Nano Lett.* **12**, 1538-1544 (2012).

29. Lee, Y. H. *et al.* Synthesis and transfer of single-layer transition metal disulfides on diverse surfaces. *Nano Lett.* **13**, 1852-1857 (2013).

30. Van der Zande, A. M. *et al.* Grains and grain boundaries in highly crystalline monolayer molybdenum disulphide. *Nat. Mater.* **12***,* 554-561 (2013).

31. Najmaei, S. *et al.* Vapour phase growth and grain boundary structure of molybdenum disulphide atomic layers. *Nat. Mater.* **12**, 754-759 (2013).

32. Yu, Y. *et al.* Controlled scalable synthesis of uniform, high-quality monolayer and few-layer MoS_2 films, *Sci. Rep.* **3**, 1866, (2013).

33. Zhang, Y. *et al.* Controlled growth of high-quality monolayer WS_2 layers on sapphire and imaging its grain boundary. *ACS Nano* **7**, 8963-8971 (2013).

34. Shaw, J. C. *et al.* Chemical vapor deposition growth of monolayer $MoSe_2$ nanosheets *Nano Res*. **7**, 511-517 (2014).

35. Mann, J. *et al.* 2-Dimensional transition metal dichalcogenides with tunable direct band gaps: $MoS_{2(1-x)}Se_{2x}$ monolayers. *Adv. Mater.* **26**, 1399–1404 (2014).

36. Li, H. *et al.* Growth of alloy $MoS_{2x}Se_{2(1-x)}$ nanosheets with fully tunable chemical compositions and optical properties. *J. Am. Chem. Soc.* **136**, 3756-3759 (2014).

37. Schmidt. H. *et al.* Transport properties of monolater MoS_2 grown by chemical vapor deposition. *Nano. Lett.* **14**, 1909-1913 (2014).

38. Ling, X. *et al.* Role of the seeding promoter in MoS_2 growth by chemical vapor deposition. *Nano. Lett.* **14**, 464-472 (2014).

39. Huang, J. K. *et al.* Large-area synthesis of highly crystalline WSe_2 monolayers and device applications. *ACS Nano* **14**, 923-930 (2014).

40. Tongay, S. *et al.*Two-dimensional semiconductor alloys: monolayer $Mo_{1-x}W_xSe_2$, *Appl. Phys. Lett.*, **104**, 012101 (2014).

41. Zhou, H. *et al.* Thickness-dependent patterning of MoS_2 sheets with well-oriented triangular pits by heating in air," *Nano Res*. **6**, 703–711 (2013).

42. Gutierrez, H. R. *et al.* Extraordinary room-temperature photoluminescence in triangular WS_2 monolayers. *Nano Lett* **13**, 3447-3454 (2013).

43. Zhao, W.J. *et al.* Lattice dynamics in mono- and few-layer sheets of WS_2 and WSe_2. *Nanoscale* **5**, 9677-9683 (2013).

44. Zhao, W.J. *et al.* Evolution of electronic structure in atomically thin sheets of WS_2 and WSe_2. *ACS Nano* **7**, 791-797 (2013).

45. Coehoorn, R. , Dijkstra, C. H., J. & Flipse, C. J. F. Electronic structure of $MoSe_2$, MoS_2, and WSe_2. I. Band-structure calculations and photoelectron spectroscopy. *Phys. Rev. B* **35** 6195-6202 (1987).

46. Yan, K. *et al.* Modulation-doped growth of mosaic graphene with single-crystalline p–n junctions for efficient photocurrent generation. *Nat. Commun.* **3**, 1280 (2012).

47. M. Y. Li, *et al*, Epitaxial growth of a monolayer WSe2-MoS2 lateral p-n junction with an atomically sharp interface. Science **349**, 524-528 (2015)

48. Huang, C. M. et al. Lateral heterojunctions within monolayer MoSe2-WSe2 semiconductors. Nature Materials **13**, 1096-1101, doi:Doi 10.1038/Nmat4064 (2014).

49. Gong, Y. J. et al. Vertical and in-plane heterostructures from WS2/MoS2 monolayers. Nature Materials **13**, 1135-1142, doi:Doi 10.1038/Nmat4091 (2014)

Chapter III: SYNTHESIS OF WS2XSE2-2X ALLOY NANOSHEETS WITH COMPOSITION TUNABLE ELECTRONIC PROPERTIES

A. Introduction to semiconductor TMD alloy

The two-dimensional layered materials (2DLMs) are emerging as an exciting class of material system that has the potential to enable breakthroughs in fundamental materials science and create totally new technologies.[1-13] In general, a large family of layered materials (*e.g.*, MoS_2, WS_2, $NbSe_2$ and Bi_2Te_3) in which the atomic layers are weakly bonded together by *van der Waals* (vdW) interactions, can be isolated into single or few-layer nanosheets, allowing to access a wide range of physical properties at the atomic scale, such as metallic, semimetallic, semiconducting, insulating, topological insulating, superconducting and thermoelectric properties.[1-3,14-20] In particular, the layered transition metal dichalcogenides (TMDs) (*e.g.*, MoS_2, WSe_2) represent a large family of layered materials, many of which exhibit a tunable band gap that transits from an indirect band gap in bulk crystals to a direct band gap in monolayer nanosheets.[15-17,21,22] These 2D nanosheets typically have well-defined crystalline structure with few surface dangling bonds that traditionally plaque conventional semiconductor nanostructures. These 2D-TMDs have thus emerged as an exciting class of atomically thin semiconductors for a new generation of electronic, optoelectronic and valleytronic devices, as well as ultra sensitive sensors.[15,17,23-43]

Recent studies have demonstrated the exciting potentials of these 2D semiconductors, including the creation of atomically thin transistors that function in the gigahertz regime and entirely new types of heterostructure devices.[23,24,27,28,31,32,36,37,44] However, the studies to date

are largely based on small flakes obtained from mechanical exfoliation. Rational chemical synthesis of 2D-TMDs and their heterostructures represents a significant challenge and has motivated considerable efforts worldwide.[1,2,14,16,25,28,45-54] To explore the full potential of 2D-TMDs requires a precise control of their chemical compositions, physical dimensions and hence the electronic and optical properties. For example, to design optoelectronic devices with desired spectral responses requires semiconductors with tunable band gaps.[24,27,30,31] Creating semiconductor alloys with variable chemical compositions is an effective strategy for the band gap engineering of bulk or thin film semiconductors. Using a similar strategy, a series of 2D-TMD alloy nanosheets have been recently prepared with tunable band gaps and optical properties.[45,48,55-66] The electronic properties of such alloy nanosheets are, however, rarely systematically explored to date.

In addition to band gap engineering, intentionally introducing a controllable number of impurity elements (~10^{16}-10^{19}/cm^3) into the bulk semiconductor lattice represents another key strategy to control the electronic properties of semiconductors. The impurity doping largely dictates the charge carrier type and carrier concentration in traditional semiconductors, and is central for creating functional electronic and optoelectronic devices. However, the controllable impurity doping in atomically thin 2D-TMD crystals represents a considerable challenge and the systematic control of charge carrier type and concentration has not been achieved to date.[67-71] Recent studies indicate that the naturally grown WS_2 nanosheets on SiO_2/Si substrate mainly exhibit n-type semiconductor characteristics, while naturally grown WSe_2 nanosheets on SiO_2/Si substrate are mostly p-type semiconductors.[16,25,72] Therefore, it offers a plausible pathway to control the carrier type and electronic properties of such 2D

nanosheets by creating a mixing alloy of WS_2 and WSe_2 with tunable chemical compositions. Here, for the first time, the synthesis of $WS_{2x}Se_{2-2x}$ alloy nanosheets with fully tunable chemical compositions, optical and electronic properties was reported.

B. Dual source CVD growth of $WS_{2x}Se_{2-2x}$ alloy

The chemical vapor deposition (CVD) process has been recently developed for the growth of atomically thin 2D-TMDs on different substrate including SiO_2/Si, in which the target TMD vapor is generated by thermally evaporating the selected solid source.[14,16,50] This approach is rather versatile and has been applied for the synthesis of diverse 2D-TMD nanosheets (*e.g.*, MoS_2, WS_2, $MoSe_2$, WSe_2) by simply switching the solid source. Additionally, it is also possible to produce the TMD alloy nanosheets by introducing multiple solid sources and mixing different TMD vapor phase reactants in the aforementioned process.[25,45-47]

In this study, to synthesize $WS_{2x}Se_{2-2x}$ nanosheets, the WS_2 and WSe_2 vapor phase reactants are created and by placing the respective solid material at different temperature in a home built CVD system (Fig. 4-1). The resulting vapor phase reactants were mixed and transported downstream in argon carrier gas to produce $WS_{2x}Se_{2-2x}$ nanosheets on the SiO_2/Si substrates placed at the downstream end of the CVD system. The equilibrium partial pressure of WS_2 and WSe_2 and their ratio can be precisely controlled by systematically varying the temperature of WS_2 and WSe_2 source to produce $WS_{2x}Se_{2-2x}$ nanosheets with fully tunable chemical compositions.

In details, the synthesis was carried out in a home built CVD system (Fig. 4-1). Two quartz boats with 0.8 g WS_2 powder (Alfa Aesar, 99.8%) and 0.6 g WSe_2 powder (Alfa Aesar,

99.98%) were loaded at variable locations inside a 1-inch quartz tube in a horizontal tube furnace. A clean Si/SiO_2 substrate (~1 cm × 5 cm) was placed at downstream end of the furnace as the growth substrate. The system was purged with ultra-high purity argon (Ar) gas (Rizhen, ~99.999%) and then raised to the desired growth temperature. The WS_2 source and WSe_2 source were placed at different locations in the quartz tube with an intrinsic temperature gradient inside the tube furnace. The ultra-high purity Ar gas is used as the carrier gas and the overall pressure inside the growth chamber is kept at 1 bar. To grow $WS_{2x}Se_{2-2x}$ nanosheets with increasing S atomic ratio, the temperature of WS_2 source is gradually increased from 1155 ^{o}C to 1194 ^{o}C, while WSe_2 source is reduced from 1194 ^{o}C to 1100 ^{o}C by controlling their exact locations inside the tube furnace, producing systematically tunable vapour pressure of WS_2 and WSe_2 and their relative ratio. Monolayer or few-layer $WS_{2x}Se_{2-2x}$ alloy nanosheets with different compositions can thus be synthesized by controlling the equilibrium partial pressure ratio of WS_2 and WSe_2.

C. Characterization of $WS_{2x}Se_{2-2x}$ alloy

By systematically varying the growth parameters, we have produced a series of $WS_{2x}Se_{2-2x}$ nanosheets with continuously tunable alloy compositions on the 300 nm SiO_2/Si substrate. The resulting alloy nanosheets are typically monolayers with a well-defined triangular shape, as identified by optical contrast and atomic force microscopy studies (Fig. 4-2a and Fig. 4-6). To investigate the band gap modulation in the resulting alloy nanosheets, micro-photoluminescence (μ-PL) spectra were taken using a micro-Raman microscope and spectrometer excited by a 488 nm argon ion laser (power: 5μW) in ambient condition. Photoluminescence studies demonstrate that all the monolayer samples display prominent

emission with a single sharp peak with full width at half maximum (FWHM) about 25 nm. The PL spectral peak positions are continuously tunable from 626.6 nm (nearly pure WS_2) to 751.9 nm (nearly pure WSe_2) depending on the exact synthetic conditions (Fig. 4-2b). A spatially resolved mapping of the PL peak positions of an alloy nanosheet shows a rather small variation of the peak positions (<3 nm, which may be corresponding to 2% composition difference if we think the reason for peak shift is just from composition, but for the peak variation in same sample, the main difference come from center to edge due to interaction with substrate. Compared with 8% composition difference of neighboring sample in Fig. 4-2b and spectra taken from center, the 3nm variation is a good indicator of alloy uniformity) across the entire triangular domain (Fig. 4-2c), suggesting the spatially uniform chemical composition in the resulting nanosheets. Furthermore, the spatially resolved mapping of the PL intensity also shows a highly uniform contrast (Fig. 4-2d), demonstrating highly uniform optical properties and crystalline quality. To correlate the band gap energy with the composition of the alloy nanosheets, we have approximated the band gap (E_g) using the PL emission peak ($E_g=hc/\lambda$, where h is Planck constant, c is the speed of light, and λ is the wavelength of PL peak) and determined the composition using energy dispersive X-ray spectroscopy (EDS) elemental analysis. The plot of the band gap vs. composition shows an apparent linear relationship (Fig. 4-2e), as expected for the ternary semiconductor alloys: $E_g(x) = xE_{g(WS2)}+(1-x)E_{g(WSe2)}$, where x is the S/(S+Se) ratio.[61] These studies clearly demonstrate that the band gap of the alloy nanosheets can be fully tuned all the way from pure WS_2 to pure WSe_2 by systematically controlling the growth conditions. This band-gap

tunability in $WS_{2x}Se_{2-2x}$ alloy system can greatly enrich 2D material family and enable spectral tunability for selected optoelectronic applications.

To further investigate the structural evolution in the $WS_{2x}Se_{2-2x}$ alloy nanosheets, we have collected the Raman spectra from the same sample series used for PL studies. In general, the Raman spectra display five main modes for most $WS_{2x}Se_{2-2x}$ nanosheets (Fig. 4-3a), which can be assigned to $A_{1g\,(S\text{-}W)}$ mode (398.5 cm^{-1}–419.7 –), $A_{1g\,(Se\text{-}W)}$ mode (251.6 – 266.5 cm^{-1}), $A_{1g\,(S\text{-}W\text{-}Se)}$ mode (379.0 – 385.2 cm^{-1}), $E_{2g\,(S\text{-}W)}$ mode (~354.7-355.9 cm^{-1}) and the $E_{2g\,(S\text{-}W)}$-$LA_{\,(S\text{-}W)}$+$A_{1g\,(Se\text{-}W)}$-$LA_{\,(Se\text{-}W)}$ mode (135.2 – 172.5 cm^{-1}). The normalized Raman spectra of the $WS_{2x}Se_{2-2x}$ nanosheets with modulated compositions show a clear peak position shift and relative intensity evolution for the A_{1g} mode (Fig. 4-3e). The $A_{1g\,(S\text{-}W)}$ mode shows a strong resonance at 398.5 cm^{-1} for WSe_2 rich phase, that systematically shifts to the higher frequency (up to 419.7 cm^{-1}) with increasing intensity as the S ratio is cumulative; Similarly, the A_{1g} (Se-W) mode follows the same trend and changes from a strong resonance at 251.6 cm^{-1} in pure WSe_2 phase to 266.5 cm^{-1} in WS_2-rich phase. The $E_{2g(S\text{-}W)}$-$LA_{(S\text{-}W)}$+$A_{1g\,(Se\text{-}W)}$-$LA_{(Se\text{-}W)}$ mode, the superposition of $E_{2g\,(S\text{-}W)}$-$LA_{(S\text{-}W)}$ and $A_{1g\,(Se\text{-}W)}$-$LA_{(Se\text{-}W)}$ also showed a systematic shift from 135.2 cm^{-1} in WSe_2 rich phase to 172.5 cm^{-1} in WS_2 rich phase, which matches well with the individual peak evolution of $E_{2g(S\text{-}W)}$ and $A_{1g(Se\text{-}W)}$ and is unique for $WS_{2x}Se_{2-2x}$ alloy nanosheets; Additionally, another extra alloy peak, the $A_{1g\,(S\text{-}W\text{-}Se)}$ mode can also be observed in the $WS_{2x}Se_{2-2x}$ alloy nanosheets, with the resonance frequency shifting from 379.0 cm^{-1} in WSe_2 rich phase to 385.2 cm^{-1} in WS_2 rich phase. It is also interesting to note that $E_{2g(S\text{-}W)}$ mode remains at nearly the same frequency, with less than 1.2 cm^{-1} difference across the entire composition modulation range. There appears to be little

contribution from the $E_{2g(Se-W)}$ mode, which could be attributed to very weak $E_{2g(Se-W)}$ mode and its weak coupling with the strong $E_{2g(S-W)}$ mode. The systematic Raman shifts further confirm the expected structural and compositional evolution in the $WS_{2x}Se_{2-2x}$ alloy nanosheets.

To further probe the microstructure of $WS_{2x}WSe_{2-2x}$ alloy nanosheets, transmission electron microscopy (TEM) studies, including energy dispersive X-ray spectroscopy (EDS), high-resolution TEM (HRTEM) image and selected area electron diffraction (SAED) (Fig. 4-4) were employed for crystal structure and composition analysis. Fig. 4-4a shows a low magnification high-angle annular dark field (HAADF) image of a $WS_{2x}Se_{2-2x}$ nanosheet. The spatially resolved EDS elemental mapping of the S, Se and W elements show relative uniform distribution across the entire triangular domain, indicating composition uniformity throughout the entire nanosheet (Fig. 4-4b to 4d). The HRTEM image showed the well-resolved lattice fringe along (100) plane with no obvious defects, confirming the high crystalline quality of the alloy nanosheets (Fig. 4-4e). The selected-area electron diffraction (SAED) taken along the [0001] zone axis displays a single set of diffraction spots with 6-fold symmetry, further confirming the single crystal quality of the alloy nanosheets (Fig. 4-4f). A systematic analysis of a series of SAED patterns of a series selected alloy samples shows that the lattice constant can be continuously tuned from 2.8361 Å in near pure WSe_2 to 2.7202 Å in nearly pure WS_2 (Fig. 4-7), further confirming the successful alloy formation.

D. Electrical properties of $WS_{2x}Se_{2-2x}$ alloy

To probe the composition modulation of the electronic properties of the $WS_{2x}Se_{2-2x}$ alloy nanosheets, we have studied the electrical transport properties of $WS_{2x}Se_{2-2x}$ nanosheets using the back-gated field effect transistors (FETs). The back-gated nanosheet FETs are fabricated on 300 nm SiO_2/Si substrate (Fig. 4-5a). In general, a single triangular domain is used as the transistor channel with a channel length around 5μm. The source and drain electrodes are defined by using electron beam lithography and metalized by using electron beam evaporation (10-nm-Ti/50-nm-Au for S-rich alloys; and 50-nm-Au for Se-rich alloys). The SiO_2/Si substrate is used as the back gate with the 300 nm SiO_2 as the gate dielectrics. The standard transistor measurements were conducted under ambient condition to derive the conductivity, on-off ratio, threshold voltage and carrier type and mobility. To ensure the consistency, five to ten devices are fabricated from each sample to evaluate their electrical properties.

The output characteristics (the source-drain current (I_{sd}) vs. source-drain voltage (V_{sd}) at varying back gate voltages) of a typical $WS_{2x}Se_{2-2x}$ nanosheet (x=0.813) FET show nearly linear relationship (Fig. 4-5b), indicating an Ohmic contact was achieved at the source-drain contacts. The current amplitude increases with increasingly positive gate voltage, suggesting an n-type semiconductor behavior. The transfer characteristics (source-drain current (I_{sd}) vs. gate voltage (V_g)) show an on-off ratio of 10^5 to 10^8 can be achieved for most devices (Fig. 4-5c and inset, Fig. 4-8). The electrical transport studies of the nanosheet devices with different alloy compositions show a systematic shift in carrier type, from p-type behavior in WSe_2-rich phase, and to n-type semiconductors in WS_2-rich phase, and a consistent shift of the threshold voltages as the composition is changed (Fig. 4-9).

The evolution of electrical properties and FET threshold voltages can be more clearly seen from $I_{sd}^{1/2}$-V_g plot under a source-drain bias of 3 V for the nanosheets with increasing sulfur atomic ratio from nearly pure WSe_2 (brown curve) to nearly pure WS_2 (black curve) (Fig. 4-5d). For the WSe_2-rich alloys (~ 0-0.55 of sulfur atomic ratio), the FETs predominantly display p-type semiconductor properties, whereas for the WS_2-rich alloys (~ 0.55-1 of sulfur atomic ratio), the n-type semiconductor properties are mainly observed. Additionally, it is noted that, for the intermediate alloy region (0.40-0.65 of S atomic ratio), several devices showed weak ambipolar behavior (Fig. 4-8). For WSe_2-rich alloys, the devices are normally "on" with a highest threshold voltage (V_{th}) of +33 V observed in the nearly pure WSe_2 nanosheets, suggesting relatively high hole-concentration. The extracted average positive threshold voltage of the alloy samples decreases with the decreasing selenium ratio, suggesting a reducing number of holes in the nanosheets transistors; Similarly for the WS_2-rich alloys, a V_{th} of -50 V is observed for the nearly pure WS_2 sample, indicating the intrinsically n-type doping behavior. The negative threshold voltage also decreases with the decreasing sulfur ratio, signifying the decreasing electron carriers in the nanosheets with lower S-ratio (Fig. 4-5e). Overall, the WSe_2-rich alloys show highly p-type behavior, which gradually shifts to the lightly doped p-type semiconductors as the Se ratio is decreased, and then switches to an n-type semiconductor character as the Se ratio is further decreased in the WS_2 rich alloys. The derived hole-mobility dropped from 68.2 $cm^2V^{-1}s^{-1}$ to 5.3 $cm^2V^{-1}s^{-1}$ as the Se-ratio is decreased in Se-rich side. The electron mobility in S-rich alloys shows a similar trend, starting from a relatively high value of 11.8 $cm^2V^{-1}s^{-1}$ in the nearly pure WS_2, and decreasing to 0.9 $cm^2V^{-1}s^{-1}$ in the increasingly alloying samples (Fig. 4-5f). The mobility

values achieved in the Se-rich and S-rich end sample are comparable to the best-reported mobility values for pure WSe_2 and WS_2 samples. The relative low mobility for intermediate alloyed $WS_{2x}Se_{2-2x}$ nanosheets (0.30<x<0.80) may be partly attributed to higher contact resistance due to lower doping concentration, and partly to the increased ionized impurity scattering and alloy scattering in the alloy sample, which is commonly observed in group III-V alloy semiconductors.[73] It's noted that lowest mobility of alloy was observed at about 60% S concentration, which may be due to slight chemical difference of S or Se, the atomic structure of the alloy and measurement limitation discussed below. Our electrical transport studies clearly demonstrate the carrier type and threshold voltages of the alloy nanosheet transistors can be systematically tuned by varying the alloy composition. We recognize that both the intrinsic doping (dominated by impurities, vacancies) and contact doping (dominated by band alignments) could affect the electrical transport characteristics of the alloy nanosheet transistors, and a complete decouple of these two doping effects is difficult. Further investigation of the electronic property evolution in the alloy nanosheets would be an interesting topic in future studies.

E. Discussion and summary

In summary, we have shown that $WS_{2x}Se_{2-2x}$ alloy nanosheets with fully tunable chemical compositions can be successfully grown on SiO_2/Si substrate by controlling the relative ratio of WS_2 and WSe_2 vapor in a home-built CVD system. Micro-photoluminescence and micro-Raman studies showed a systematic shift of PL peak position and the Raman resonance frequencies, indicating successful chemical, structural modulation and band gap engineering.

TEM studies confirm single crystalline structure with uniform alloy. Electrical transport studies further reveal a systematic modulation of the electronic properties, including the carrier type, threshold voltage and mobility, as the alloy composition is changed. The successful growth of $WS_{2x}Se_{2-2x}$ nanosheets with tunable band gaps and electrical properties will greatly enrich the TMD material family, and could empower a great deal flexibility in designing atomically thin electronics and optoelectronics with tailored device characteristics. The main idea of this study was published at the title of "Synthesis of $WS_{2x}Se_{2-2x}$ Alloy Nanosheets with Composition-Tunable Electronic Properties" at *Nano Letters*, **16**, 264-269. (2016)

F. Figures and Legends

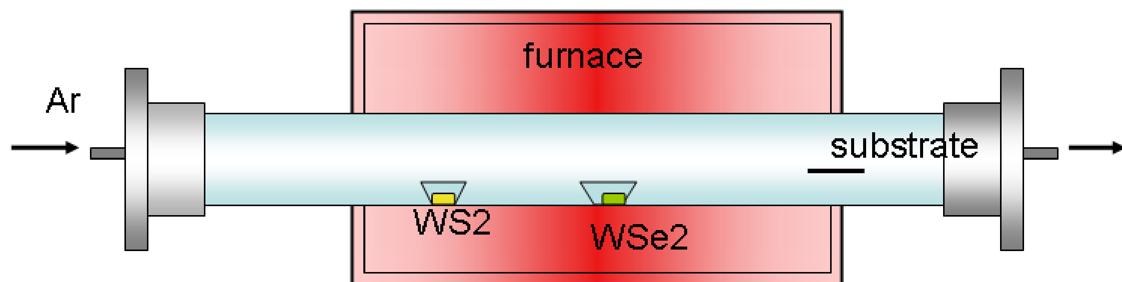

Figure 4-1. Schematic illustration of the home-built CVD system. Two sources, WS_2 and WSe_2 power were placed in the heater zone, but with tuned distance to heater center, which leading to different temperature of each source, i.e. different ratio of vapor pressure of WS_2 and WSe_2, enabling the alloy growth with tunable composition.

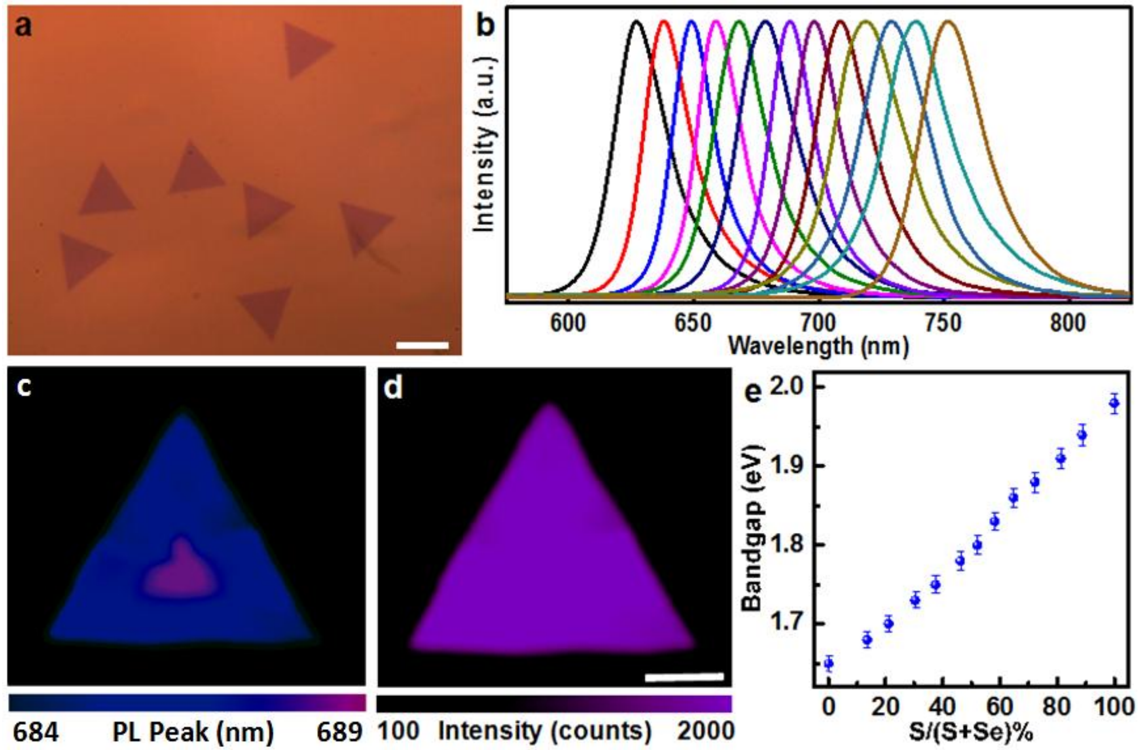

Figure 4-2. Bandgap engineering of $WS_{2x}WSe_{2-2x}$ nanosheets. **a**, Optical microscopy image of typical $WS_{2x}Se_{2-2x}$ nanosheets (x=0.454). Scale bar: 20 μm; **b**, Photoluminescence spectra of a series of composition tunable $WS_{2x}Se_{2-2x}$ monolayer nanosheets; **c**, Photoluminescence peak position mapping of one typical $WS_{2x}Se_{2-2x}$ nanosheets (x=0.522, scale bar: 10 μm) **d**, Photoluminescence intensity mapping of the same $WS_{2x}Se_{2-2x}$ nanosheets (x=0.522, mapping peak: 687.5 nm, scale bar: 10 μm); **e**, The optical bandgap vs. sulfur ratio in $WS_{2x}Se_{2-2x}$ nanosheets.

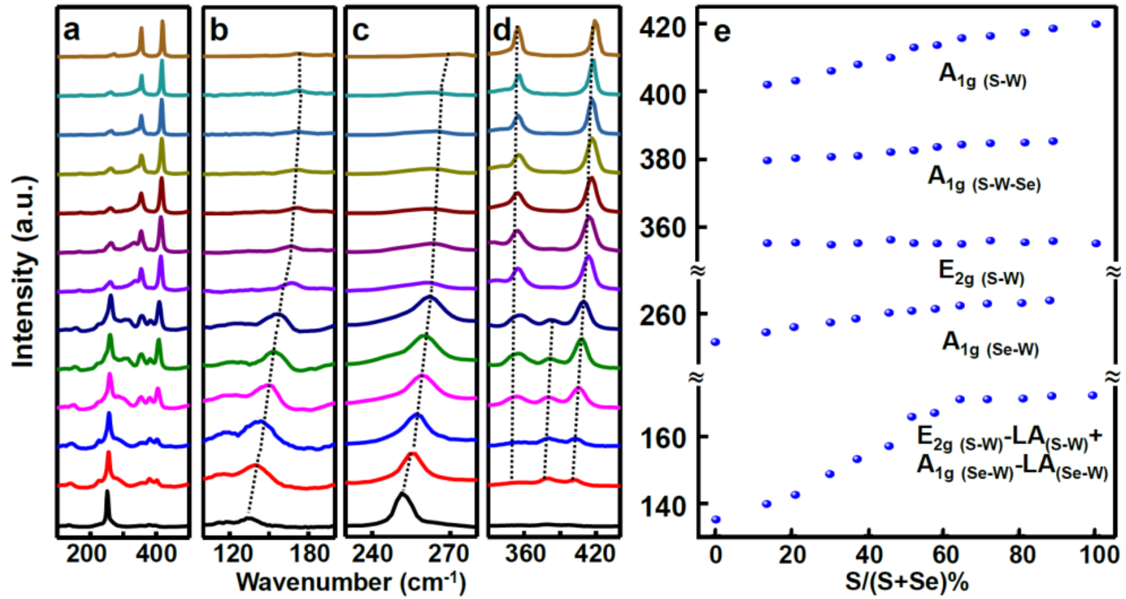

Figure 4-3. The evolution of Raman spectra in the $WS_{2x}Se_{2-2x}$ monolayer nanosheets as a function of chemical composition. **a**, Full range Raman spectra, **b**, $E_{2g(S\text{-}W)}$)-$LA_{(S\text{-}W)}$ +$A_{1g(Se\text{-}W)}$ -$LA_{(Se\text{-}W)}$ mode of the $WS_{2x}Se_{2-2x}$ nanosheets, **c**, A_{1g} of Se-W mode and **d**, E_{2g} of S-W mode, A_{1g} of S-W-Se mode and A_{1g} of S-W; **e**, The Raman spectra peak position shift with increasing S atomic ratio for the five Raman modes.

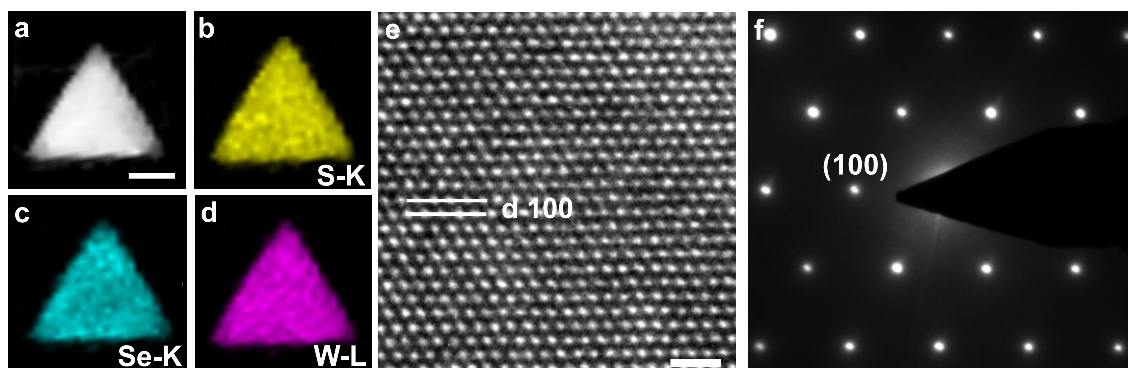

Figure 4-4. Composition and crystal structure analysis of the alloy nanosheet by TEM. **a**, HAADF image of a small $WS_{2x}Se_{2-2x}$ domain (x=0.573, scale bar: 500 nm); EDS mapping of the same nanosheet for S-K line **b**, Se-K line **c** and W-L line **d**; **e**, High-resolution TEM image of a typical $WS_{2x}Se_{2-2x}$ nanosheet (x= 0.796; scale bar: 1nm); **f**, SAED pattern of a $WS_{2x}Se_{2-2x}$ nanosheet along the zone axis of [0001].

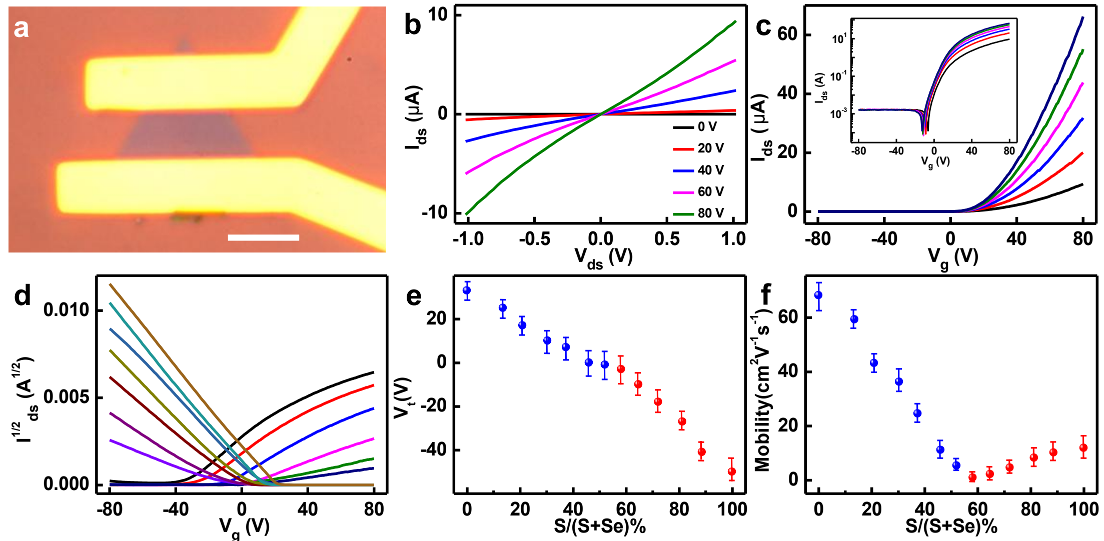

Figure 4-5. Electrical transport properties of $WS_{2x}Se_{2-2x}$ alloy nanosheets. a, Optical microscopy image of a typical back gated field effect transistor made of a $WS_{2x}Se_{2-2x}$ nanosheet (scale bar: 5 μm); **b**, Output characteristics of a $WS_{2x}Se_{2-2x}$ nanosheet transistor (x=0.813, gate voltage changing from 0 - 80 V in 20 V steps); **c**, Transfer characteristics of the same transistor (source-drain bias changing from 0.5 V to 3.0 V in 0.5 V steps); inset: log plot of I_{ds}-V_g curve; **d**, Transfer characteristics ($I_d^{1/2}$-V_g plot) of $WS_{2x}Se_{2-2x}$ nanosheet transistors with different S atomic ratio from nearly pure WSe_2 (brown curve) to nearly pure WS_2 (black curve); **e**, The alloy nanosheet transistor threshold voltage (V_{th}) vs. S atomic ratio, with the blue dots highlighting the n-type behavior in WS_2-rich alloys and red dots highlighting p-type behavior in WSe_2-rich alloys; **f**, Field-effect mobility vs. S atomic ratio relationship in $WS_{2x}Se_{2-2x}$ alloy nanosheets, with the blue dots representing the electron mobility in WS_2-rich alloys and red dots representing hole mobility in WSe_2-rich alloys.

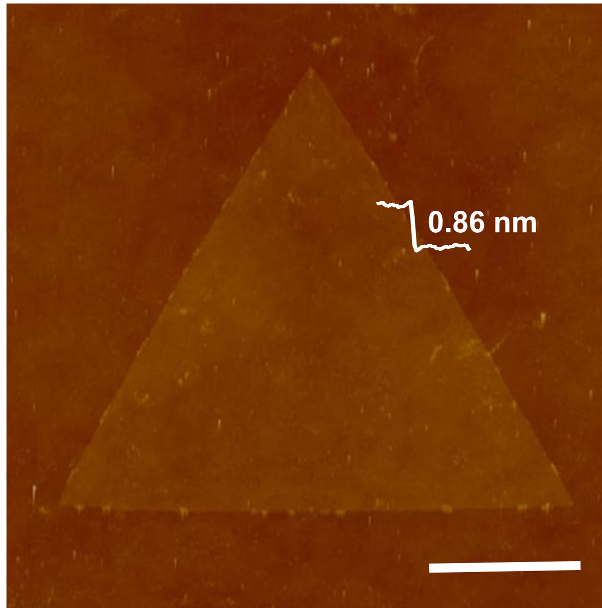

Figure 4-6. Typical AFM image of $WS_{2x}Se_{2-2x}$ nanosheets (x=0.668) with thickness 0.86 nm. Scale bar: 5 μm.

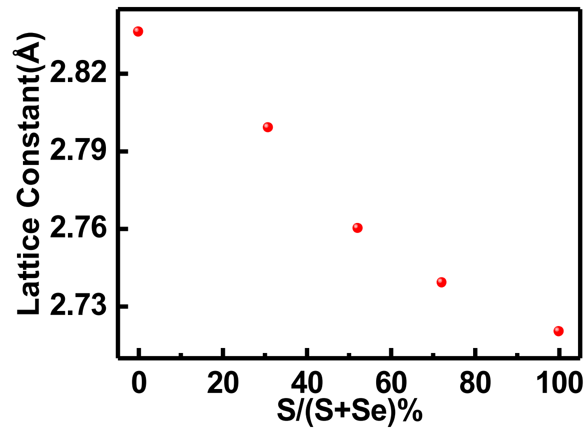

Figure 4-7. Relationship between the lattice constants derived from SAED studies and the alloy composition.

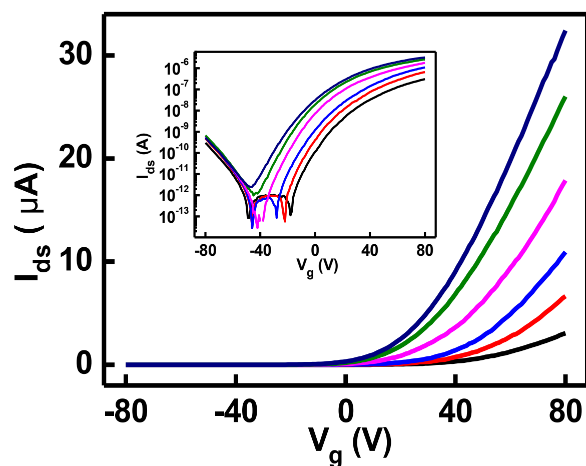

Figure 4-8. **Transfer characteristics of $WS_{2x}Se_{2-2x}$ (x=0.515) transistors** (source-drain bias changing from 0.5 V to 3 V in 0.5 V steps); inset: log plot of I_{ds}-V_g curve. For the intermediate alloy region (0.40-0.65 of S atomic ratio), several devices showed weak ambipolar behavior.

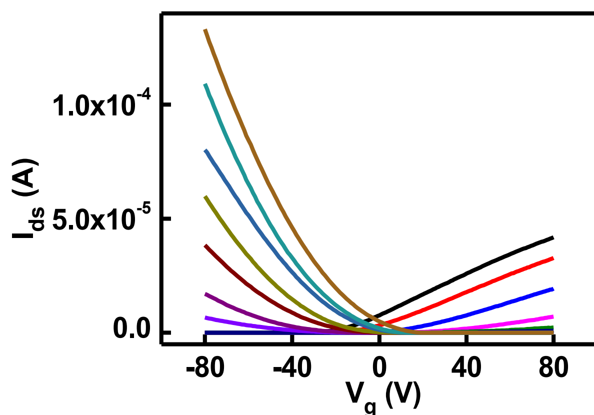

Figure 4-9. **Transfer characteristics of $WS_{2x}Se_{2-2x}$ nanosheet transistors with different S atomic ratio from nearly pure WSe_2 (brown curve) to nearly pure WS_2 (black curve).**

F. Reference:

1. Chhowalla, M. *et al.* The chemistry of two-dimensional layered transition metal dichalcogenide nanosheets. *Nat Chem* **5**, 263-275, doi:10.1038/Nchem.1589 (2013).

2. Coleman, J. N. *et al.* Two-Dimensional Nanosheets Produced by Liquid Exfoliation of Layered Materials. *Science* **331**, 568-571, doi:10.1126/science.1194975 (2011).

3. Novoselov, K. S. *et al.* Two-dimensional atomic crystals. *P Natl Acad Sci USA* **102**, 10451-10453, doi:10.1073/pnas.0502848102 (2005).

4. Butler, S. Z. *et al.* Progress, Challenges, and Opportunities in Two-Dimensional Materials Beyond Graphene. *Acs Nano* **7**, 2898-2926, doi:10.1021/nn400280c (2013).

5. Huang, X., Zeng, Z. Y. & Zhang, H. Metal dichalcogenide nanosheets: preparation, properties and applications. *Chem Soc Rev* **42**, 1934-1946 (2013).

6. Zhang, H. Ultrathin Two-Dimensional Nanomaterials. *Acs Nano*, doi:10.1021/acsnano.5b05040 (2015).

7. Kuc, A., Heine, T. & Kis, A. Electronic properties of transition-metal dichalcogenides. *MRS Bulletin* **40**, 577-584 (2015).

8. Cao, L. Two-dimensional transition-metal dichalcogenide materials: Toward an age of atomic-scale photonics. *MRS Bulletin* **40**, 592-599 (2015).

9. Shi, Y., Zhang, H., Chang, W.-H., Shin, H. S. & Li, L.-J. Synthesis and structure of two-dimensional transition-metal dichalcogenides. *MRS Bulletin* **40**, 566-576 (2015).

10. Amin, B., Singh, N. & Schwingenschlögl, U. Heterostructures of transition metal dichalcogenides. *Phys Rev B* **92**, 075439 (2015).

11. Chia, X., Eng, A. Y. S., Ambrosi, A., Tan, S. M. & Pumera, M. Electrochemistry of

Nanostructured Layered Transition-Metal Dichalcogenides. *Chemical Reviews*, doi:10.1021/acs.chemrev.5b00287 (2015).

12. Schmidt, H., Giustiniano, F. & Eda, G. Electronic transport properties of transition metal dichalcogenide field-effect devices: surface and interface effects. *Chem Soc Rev* **44**, 7715-7736, doi:10.1039/C5CS00275C (2015).

13. Duan, X., Wang, C., Pan, A., Yu, R. & Duan, X. Two-dimensional transition metal dichalcogenides as atomically thin semiconductors: opportunities and challenges. *Chem Soc Rev*, doi:10.1039/C5CS00507H (2015).

14. Liu, K. K. *et al.* Growth of Large-Area and Highly Crystalline MoS2 Thin Layers on Insulating Substrates. *Nano Lett* **12**, 1538-1544, doi:10.1021/nl2043612 (2012).

15. Mak, K. F., Lee, C., Hone, J., Shan, J. & Heinz, T. F. Atomically Thin MoS2: A New Direct-Gap Semiconductor. *Phys Rev Lett* **105**, doi:Artn 136805 10.1103/Physrevlett.105.136805 (2010).

16. Zhou, H. L. *et al.* Large Area Growth and Electrical Properties of p-Type WSe2 Atomic Layers. *Nano Lett* **15**, 709-713, doi:Doi 10.1021/Nl504256y (2015).

17. Wang, Q. H., Kalantar-Zadeh, K., Kis, A., Coleman, J. N. & Strano, M. S. Electronics and optoelectronics of two-dimensional transition metal dichalcogenides. *Nat Nanotechnol* **7**, 699-712, doi:10.1038/Nnano.2012.193 (2012).

18. Chhowalla, M., Liu, Z. F. & Zhang, H. Two-dimensional transition metal dichalcogenide (TMD) nanosheets. *Chem Soc Rev* **44**, 2584-2586, doi:10.1039/c5cs90037a (2015).

19. Dang, W. H., Peng, H. L., Li, H., Wang, P. & Liu, Z. F. Epitaxial Heterostructures of Ultrathin Topological Insulator Nanoplate and Graphene. *Nano Lett* **10**, 2870-2876,

doi:10.1021/nl100938e (2010).

20. Guo, Y. F. *et al.* 2D Hybrid Nanostructured Dirac Materials for Broadband Transparent Electrodes. *Advanced Materials* **27**, 4315-4321, doi:10.1002/adma.201501912 (2015).

21. Splendiani, A. *et al.* Emerging Photoluminescence in Monolayer MoS2. *Nano Lett* **10**, 1271-1275, doi:10.1021/nl903868w (2010).

22. Eda, G. *et al.* Photoluminescence from Chemically Exfoliated MoS2. *Nano Lett* **11**, 5111-5116, doi:10.1021/nl201874w (2011).

23. Cheng, R. *et al.* Few-layer molybdenum disulfide transistors and circuits for high-speed flexible electronics. *Nat Commun* **5**, doi:Artn 5143 10.1038/Ncomms6143 (2014).

24. Cheng, R. *et al.* Electroluminescence and Photocurrent Generation from Atomically Sharp WSe2/MoS2 Heterojunction p-n Diodes. *Nano Lett* **14**, 5590-5597, doi:Doi 10.1021/Nl502075n (2014).

25. Duan, X. D. *et al.* Lateral epitaxial growth of two-dimensional layered semiconductor heterojunctions. *Nat Nanotechnol* **9**, 1024-1030, doi:Doi 10.1038/Nnano.2014.222 (2014).

26. Geim, A. K. & Grigorieva, I. V. Van der Waals heterostructures. *Nature* **499**, 419-425, doi:10.1038/nature12385 (2013).

27. Xu, Y. *et al.* Solution Processable Holey Graphene Oxide and Its Derived Macrostructures for High-Performance Supercapacitors. *Nano Lett* **15**, 4605-4610, doi:10.1021/acs.nanolett.5b01212 (2015).

28. Li, M. Y. *et al.* Epitaxial growth of a monolayer WSe2-MoS2 lateral p-n junction with an atomically sharp interface. *Science* **349**, 524-528 (2015).

29. Liu, Y. *et al.* Toward Barrier Free Contact to Molybdenum Disulfide Using Graphene

Electrodes. *Nano Lett* **15**, 3030-3034, doi:10.1021/nl504957p (2015).

30. Lopez-Sanchez, O., Lembke, D., Kayci, M., Radenovic, A. & Kis, A. Ultrasensitive photodetectors based on monolayer MoS2. *Nat Nanotechnol* **8**, 497-501, doi:10.1038/Nnano.2013.100 (2013).

31. Pospischil, A., Furchi, M. M. & Mueller, T. Solar-energy conversion and light emission in an atomic monolayer p-n diode. *Nat Nanotechnol* **9**, 257-261, doi:10.1038/Nnano.2014.14 (2014).

32. Ross, J. S. *et al.* Electrically tunable excitonic light-emitting diodes based on monolayer WSe2 p-n junctions. *Nat Nanotechnol* **9**, 268-272, doi:10.1038/Nnano.2014.26 (2014).

33. Roy, K. *et al.* Graphene-MoS2 hybrid structures for multifunctional photoresponsive memory devices. *Nat Nanotechnol* **8**, 826-830, doi:10.1038/Nnano.2013.206 (2013).

34. Sie, E. J. *et al.* Valley-selective optical Stark effect in monolayer WS2. *Nat Mater* **14**, 290-294 (2015).

35. Wu, S. F. *et al.* Electrical tuning of valley magnetic moment through symmetry control in bilayer MoS2. *Nat Phys* **9**, 149-153 (2013).

36. Yu, W. J. *et al.* Vertically stacked multi-heterostructures of layered materials for logic transistors and complementary inverters. *Nature Materials* **12**, 246-252, doi:10.1038/NMAT3518 (2013).

37. Yu, W. J. *et al.* Highly efficient gate-tunable photocurrent generation in vertical heterostructures of layered materials. *Nat Nanotechnol* **8**, 952-958, doi:10.1038/Nnano.2013.219 (2013).

38. Mai, C. *et al.* Many-Body Effects in Valleytronics: Direct Measurement of Valley

Lifetimes in Single-Layer MoS2. *Nano Lett* **14**, 202-206, doi:10.1021/nl403742j (2014).

39. Zou, X. M. *et al.* Interface Engineering for High-Performance Top-Gated MoS2 Field-Effect Transistors. *Adv Mater* **26**, 6255-6261, doi:DOI 10.1002/adma.201402008 (2014).

40. Buscema, M., Steele, G. A., van der Zant, H. S. J. & Castellanos-Gomez, A. The effect of the substrate on the Raman and photoluminescence emission of single-layer MoS2. *Nano Res* **7**, 561-571, doi:10.1007/s12274-014-0424-0 (2014).

41. Xu, Y. X. *et al.* Holey graphene frameworks for highly efficient capacitive energy storage. *Nature Communications* **5**, doi:Artn 4554 10.1038/Ncomms5554 (2014).

42. Yin, Z. *et al.* Single-Layer MoS2 Phototransistors. *Acs Nano* **6**, 74-80, doi:10.1021/nn2024557 (2012).

43. Jiang, S., Cheng, R., Ng, R., Huang, Y. & Duan, X. Highly sensitive detection of mercury(II) ions with few-layer molybdenum disulfide. *Nano Res* **8**, 257-262, doi:10.1007/s12274-014-0658-x (2015).

44. Zhang, W. J. *et al.* Ultrahigh-Gain Photodetectors Based on Atomically Thin Graphene-MoS2 Heterostructures. *Sci Rep-Uk* **4**, doi:Artn 3826 10.1038/Srep03826 (2014).

45. Li, H. L. *et al.* Growth of Alloy MoS2xSe2(1-x) Nanosheets with Fully Tunable Chemical Compositions and Optical Properties. *J Am Chem Soc* **136**, 3756-3759, doi:10.1021/ja500069b (2014).

46. Gong, Y. J. *et al.* Vertical and in-plane heterostructures from WS2/MoS2 monolayers. *Nat Mater* **13**, 1135-1142, doi:10.1038/NMAT4091 (2014).

47. Huang, C. M. *et al.* Lateral heterojunctions within monolayer MoSe2-WSe2

semiconductors. *Nat Mater* **13**, 1096-1101, doi:10.1038/NMAT4064 (2014).

48. Li, H. L. *et al.* Lateral Growth of Composition Graded Atomic Layer MoS2(1-x)Se2x Nanosheets. *J Am Chem Soc* **137**, 5284-5287, doi:10.1021/jacs.5b01594 (2015).

49. Schmidt, H. *et al.* Transport Properties of Monolayer MoS2 Grown by Chemical Vapor Deposition. *Nano Lett* **14**, 1909-1913, doi:10.1021/nl4046922 (2014).

50. Shaw, J. C. *et al.* Chemical vapor deposition growth of monolayer MoSe2 nanosheets. *Nano Res* **7**, 511-517, doi:10.1007/s12274-014-0417-z (2014).

51. Chen, Y.-Z. *et al.* Ultrafast and Low Temperature Synthesis of Highly Crystalline and Patternable Few-Layers Tungsten Diselenide by Laser Irradiation Assisted Selenization Process. *Acs Nano* **9**, 4346-4353, doi:10.1021/acsnano.5b00866 (2015).

52. Chen, J. Z. *et al.* One-pot Synthesis of CdS Nanocrystals Hybridized with Single-Layer Transition-Metal Dichalcogenide Nanosheets for Efficient Photocatalytic Hydrogen Evolution. *Angew Chem Int Edit* **54**, 1210-1214 (2015).

53. Tan, C. & Zhang, H. Epitaxial Growth of Hetero-Nanostructures Based on Ultrathin Two-Dimensional Nanosheets. *J Am Chem Soc* **137**, 12162-12174, doi:10.1021/jacs.5b03590 (2015).

54. Tan, C. L. *et al.* Liquid-Phase Epitaxial Growth of Two-Dimensional Semiconductor Hetero-nanostructures. *Angew Chem Int Edit* **54**, 1841-1845 (2015).

55. Feng, Q. *et al.* Growth of Large-Area 2D MoS2(1-x)Se2x Semiconductor Alloys. *Advanced Materials* **26**, 2648-2653, doi:10.1002/adma.201306095 (2014).

56. Huang, Y. L. *et al.* Bandgap tunability at single-layer molybdenum disulphide grain boundaries. *Nat Commun* **6**, doi:Artn 6298 10.1038/Ncomms7298 (2015).

57. Zheng, S. J. *et al.* Monolayers of WxMo1-xS2 alloy heterostructure with in-plane composition variations. *Appl Phys Lett* **106**, doi:Artn 063113 10.1063/1.4908256 (2015).

58. Mouri, S., Miyauchi, Y. & Matsuda, K. Tunable Photoluminescence of Monolayer MoS2 via Chemical Doping. *Nano Lett* **13**, 5944-5948, doi:10.1021/nl403036h (2013).

59. Tongay, S. *et al.* Two-dimensional semiconductor alloys: Monolayer Mo1-xWxSe2. *Appl Phys Lett* **104**, doi:Artn 012101 10.1063/1.4834358 (2014).

60. Zhang, W. *et al.* CVD synthesis of Mo(1-x)WxS2 and MoS2(1-x)Se2x alloy monolayers aimed at tuning the bandgap of molybdenum disulfide. *Nanoscale* 7, 13554-13560.

61. Kang, J., Tongay, S., Li, J. B. & Wu, J. Q. Monolayer semiconducting transition metal dichalcogenide alloys: Stability and band bowing. *J Appl Phys* **113**, doi:Artn 143703 10.1063/1.4799126 (2013).

62. Song, J. G. *et al.* Controllable synthesis of molybdenum tungsten disulfide alloy for vertically composition-controlled multilayer. *Nat Commun* **6**, doi:Artn 7817 10.1038/Ncomms8817 (2015).

63. Su, S.-H. *et al.* Controllable synthesis of band-gap-tunable and monolayer transition-metal dichalcogenide alloys. *Frontiers in Energy Research* **2**, 27 (2014).

64. Yan, T. F., Qiao, X. F., Liu, X. N., Tan, P. H. & Zhang, X. H. Photoluminescence properties and exciton dynamics in monolayer WSe2. *Appl Phys Lett* **105** (2014).

65. Gan, L.-Y., Zhang, Q., Zhao, Y.-J., Cheng, Y. & Schwingenschlögl, U. Order-disorder phase transitions in the two-dimensional semiconducting transition metal dichalcogenide alloys Mo1−xWxX2 (X = S, Se, and Te). *Scientific Reports* **4**, 6691, doi:10.1038/srep06691 (2014).

66. Klee, V. *et al.* Superlinear Composition-Dependent Photocurrent in CVD-Grown Monolayer MoS2(1–x)Se2x Alloy Devices. *Nano Letters* **15**, 2612-2619.

67. Dolui, K., Rungger, I., Das Pemmaraju, C. & Sanvito, S. Possible doping strategies for MoS2 monolayers: An ab initio study. *Phys Rev B* **88**, doi:Artn 075420 10.1103/Physrevb.88.075420 (2013).

68. Fang, H. *et al.* Degenerate n-Doping of Few-Layer Transition Metal Dichalcogenides by Potassium. *Nano Lett* **13**, 1991-1995, doi:10.1021/nl400044m (2013).

69. Fang, H. *et al.* High-Performance Single Layered WSe2 p-FETs with Chemically Doped Contacts. *Nano Lett* **12**, 3788-3792, doi:10.1021/nl301702r (2012).

70. Kiriya, D., Tosun, M., Zhao, P. D., Kang, J. S. & Javey, A. Air-Stable Surface Charge Transfer Doping of MoS2 by Benzyl Viologen. *J Am Chem Soc* **136**, 7853-7856, doi:10.1021/ja5033327 (2014).

71. Suh, J. *et al.* Doping against the Native Propensity of MoS2: Degenerate Hole Doping by Cation Substitution. *Nano Lett* **14**, 6976-6982, doi:10.1021/nl503251h (2014).

72. Zhang, Y. *et al.* Controlled Growth of High-Quality Monolayer WS2 Layers on Sapphire and Imaging Its Grain Boundary. *Acs Nano* 7, 8963-8971, doi:10.1021/nn403454e (2013).

73. Adachi, S. *Physical Properties of III-V Semiconductor Compounds*. (John Wiley & Sons, Inc, 1992).

Chapter IV: MONOLAYER PHOSPHORENE MOLECULAR SUPERLATTICES

A. Black phosphorus and phosphorene electronics

Black phosphorus (BP) was first synthesized by applying high pressure to red phosphorus and studied by P. W. Bridgman in 1914 [1]. However, its two-dimensional nature was not fully explored until 100 years later, when the thin BP transistor was fabricated, showing high current modulation up to five orders of magnitude and a respectable carrier mobility up to 1,000 $cm^2 V^{-1} s^{-1}$ [2]. The rediscovery of BP and phosphorene (monolayer BP) introduced the second important elemental two-dimensional layered material (2DLM) with balanced carrier mobility and bandgap, in contrast with semi-metallic graphene and semiconducting transition metal dichalcogenides (TMDs), yet retaining all the merits of 2DLMs. This includes the ultimate limit for electronic scaling, versatile lateral and vertical integration, along with exceptional mechanical strength and elasticity for highly robust flexible electronics.

Combining high mobility, suitable direct bandgap, and highly anisotropic properties, phosphorene represents an attractive atomically thin semiconductor for next generation electronics and optoelectronics, including transistors [2-4], broadband photo-detectors [5], and diverse *van der Waals* heterojunction devices [6]. However, the difficulty in isolating and stabilizing monolayer phosphorene [7-9] has limited most studies to date to multi-layer BP flakes rather than monolayer phosphorene. Demonstration of fundamental properties and devices from monolayer phosphorene has been severely limited by its intrinsic instability in ambient conditions. The much expected intrinsic properties including large direct bandgap or high mobility of monolayer phosphorene has been difficult to reach with traditional 2DLM processing and fabrication methods [7,10,11].

B. Intercalation of thin black phosphorus

Here electrochemical intercalation of BP with cetyltrimethylammonium bromide ($(C_{16}H_{33})N(CH_3)_3Br$, abbreviated as CTAB to form a monolayer phosphorene molecular superlattice (MPMS) with stable monolayer phosphorene characteristics was reported. Using a home-built *in situ* electro-chemical-optical measurement (IS-ECOM) system, we conducted systematic investigations of the dynamic intercalation process and the evolution of its structure and properties. The evolution of electrochemical current and photoluminescence spectra during the MPMS formation suggests a stepwise reaction mechanism. Photoluminescence studies of the intercalation product shows a strong photoluminescence signal centered at 548 nm (2.26 eV), suggesting a monolayer with a strain-induced blue shift from the theoretically predicted band gap of ~2 eV [12]. Atomic force microscopy (AFM) and X-ray diffraction (XRD) studies clearly demonstrate interlayer distance expansion from 5.23 Å in BP to 11.27 Å in MPMS, indicating the insertion of well-ordered molecular layers. Cross-sectional transmission electron microscopy (TEM) studies confirmed the highly ordered superlattice structure with alternative layers of monolayer phosphorene and self-assembled molecular (SAM) layers. Planar TEM studies reveal a significant expansion (by ~ 3%) of the phosphorene in the armchair direction, which is further confirmed by Raman spectroscopic studies. Electrical transport studies based on MPMS field effect transistors (FETs) demonstrate the highest on/off ratio ($>10^7$) reported in BP to date, yet with a respectable mobility (328 $cm^2V^{-1}s^{-1}$). Sandwiched between molecular layers, the MPMS exhibits excellent stability in ambient conductions with >10 times longer lifetime than pristine BP devices with similar starting current. DFT calculations using the Vienna ab-initio

Simulation Package (VASP) with projector augmented wave (PAW) pseudopotentials gave the most probable atomic configuration of MPMS with the predicted interlayer distance, armchair strain, and widened bandgap matching well with experimental observations. Lastly, we show that a lateral BP-MPMS heterojunction device can be created with diode characteristics. Our studies demonstrate the preparation of ambient-stable high-quality monolayer phosphorene for the first time. We expect that formation of MPMS could open up new opportunities in phosphorene electronics and photonics [13-16]. To the best of our knowledge, this unique MPMS system is one and only platform that can demonstrate all key intrinsic properties of monolayer phosphorene to date, including the highest mobility of few-layer phosphorene, highest on/off ratio, largest optical bandgap and high stability.

C. Electrochemical intercalation dynamics

The intercalation of 2DLMs with selected molecules or ions can considerably modulate their electronic properties. Examples include phase transitions in MoS_2 or TaS_2 due to Li intercalation [17-19]. However, the most typical intercalation of alkaline metals is usually unstable under ambient conditions. Here we report a systematic investigation of intercalation of BP with organic molecules (CTAB) to produce stable intercalation compounds. We constructed a home-designed electrochemical-optical measurement platform for *in situ* monitoring the evolution of electronic and optical properties during the intercalation process (Fig. 5-1a, 2b). In a typical experiment, a standard back-gated BP FET was fabricated on a 300-nm-SiO_2/Si substrate (see methods for details) and immersed in a polydimethylsiloxane (PDMS) reservoir filled with supersaturated CTAB solution dissolved in N-Methyl-2-pyrrolidone (NMP) to facilitate the intercalation process after proper

configuration of Pt counter electrode and Ag/AgCl reference electrode. This intercalation device can be placed under a Raman/photoluminescence microscope during the intercalation process. With this setup, the electrochemical current from the Pt counter electrode, the drain current from the metal drain electrode, and Raman/photoluminescence spectra can be simultaneously monitored while the BP is being intercalated.

The molecular intercalation process involves the insertion of CTAB into the BP interlayer gaps through edges during the electrochemical reaction. The electrochemical reaction consists of two half-reactions:

$$Br^- \rightarrow 1/2\ Br_2 + e^- \quad (1)$$

and

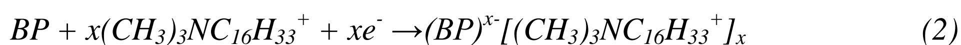

$$BP + x(CH_3)_3NC_{16}H_{33}^+ + xe^- \rightarrow (BP)^{x-}[(CH_3)_3NC_{16}H_{33}^+]_x \quad (2)$$

The electrochemical current was monitored *in situ* from the Pt counter electrode (*electrolyte gate*) as the voltage was swept from 0 V up to ~ 3 V. Careful analysis of the electrochemical current curve (I_{eg} in Fig. 5-2A) and its first derivative (Fig. 5-8) shows apparent stepwise reactions, which may be attributed to the strong layer-number dependent bandgap and electronic properties of the BP (see Supplementary Text 1 and 2 for more detailed discussions). The stepwise reaction can be partitioned into six regions based on minimum points of the first derivative of the electrochemical current (Fig. 5-8):

- **0 - 1.0 V**: no obvious intercalation (due to over-potential for Br^- sub-reaction, see more details in Supplementary Text 1),
- **1.0 - 1.4 V**: major bulk intercalation occurring,

- **1.4-2.0 V**: few-layer (~ 4-10 layers) BP formation,
- **2.0-2.5 V:** trilayer BP formation,
- **2.5-3.0 V**: bilayer BP formation and
- **beyond 3.0 V:** monolayer phosphorene formation (Fig. 5-2a).

Fig. 5-2b shows the corresponding source-drain current of first scan (black) and last scan (red) in a multi-scan intercalation process, demonstrating relative small on/off ratio before intercalation and strong gate effects with ~ 10^5 current modulation (limited by precise off-current measurement with the electrolyte gate) in the final fully intercalated materials.

An *in situ* monitor of the photoluminescence evolution in BP during the intercalation process reveals clearly the evolution from the absence of apparent photoluminescence in the visible-NIR regime in bulk BP (Fig. 5-9) to prominent emission at ~898 nm (1.38 eV), then ~ 710 nm (1.75 eV) and eventually ~ 548 nm (2.26 eV) as the intercalation process progresses (Fig. 5-2c). These emission peaks correspond roughly to near band edge emission from trilayer, bilayer and monolayer phosphorene. Interestingly, the bandgap and the onset intercalation electrochemical potential exhibit a highly similar relationship with the layer number, suggesting a close correlation between electrochemical potential and the measured bandgap (Fig. 5-2d). To the best of our knowledge, the photoluminescence emission at 548 nm (2.26 eV) is the highest optical bandgap observed in phosphorene or thin BP based structures (values from 1.45-1.84 eV were observed previously) [7,10,20], suggesting that we may have formed the true monolayer material. The observed optical bandgap of 2.26 eV is slightly higher than theoretical limit of ideal phosphorene (~ 2 eV) [21], which may be attributed to the strain induced bandgap expansion and will be further discussed in TEM

analysis section and explained by DFT calculations [10,22]. Photoluminescence map (at 550 nm) of MPMS flake show highly uniform contrast (Fig. 5-2e), indicating the relative structure uniformity of the resulting MPMS.

D. Structural characterizations of MPMS

Compared with pristine BP (Fig. 5-2f), AFM studies show the thickness of the fully intercalated MPMS (Fig. 5-2g) is increased by about 130 %. Importantly, X-ray diffraction (XRD) studies show clearly the minimum interlayer distance is expanded from 5.23 Å (16.93°) in BP to 11.27 Å (7.84°) in of MPMS with about 115 % increase in the interlayer distance (Fig. 5-2h), which is consistent with AFM measurements. Second order peak of pristine BP at 2.62 Å (34.20°) as well as the high order peaks of MPMS at 5.65 Å (15.67°) and 3.76 Å (23.61°) further confirm the expansion of the interlayer distance. Besides the final MPMS structure, most intermediate structures before reaching complete intercalation show mixed phases with variable number of BP layers (Fig. 5-10).

We have next conducted high resolution-transmission electron microscopy (HR-TEM) studies to further probe the MPMS structure, (Fig. 5-3). The cross sectional TEM images clearly show the distinct structure between layered BP (Fig. 5-3a) and MPMS superlattice (Fig. 5-3d) with strikingly different interlayer distance. Electron diffractions (ED) patterns (insets of Fig. 5-3a, 3d) clearly reveal the increased interlayer distance from 5.24 Å in BP to 11.21 Å in MPMS, which is further verified by direct measurement in the magnified cross sectional images (Fig. 5-3b, 3e). This directly observed expansion of interlayer distance is consistent with AFM thickness measurement and XRD analysis (Fig. 5-2f to 2h). The ~ 6 Å interlayer distance increase corresponds roughly to the end to end distance between the

CTAB methyl-methyl substituent [23]. Planar TEM studies reveal ~ 3% lattice expansion from 2.17 Å of pristine BP (Fig. 5-3c) to 2.24 Å of MPMS (Fig. 5-3f) in the armchair direction (200) with negligible change in the zigzag direction (1.66 Å for (020) in both BP and MPMS). ED patterns of the corresponding samples further confirmed the lattice expansion in (200) (insets of Fig. 5-3c, 3f). This distinct ~3% expansion in the armchair direction is also consistent with the observed photoluminescence blue shift in the monolayer due to strain induced bandgap expansion [10]. Elemental analysis based energy dispersive X-ray (EDX) spectra gives an atomic ratio of P:N:Br ~33.2:1.2:1.0 (Fig. 5-11), suggesting Br are also intercalated into the final superlattice structure. Although free Br_2 is produced and not intercalated into BP during the electrochemical intercalation process (see Equ. 1 & 2), the produced Br_2 during intercalation process may back-react with phosphorene$^{-}CTA^{+}$ layers again after the release of electrochemical potential, in which process the Br^{-} ions are intercalated into the final MPMS structure to form phosphorene/CTAB superlattices (Supplementary Text 1 for more details).

E. DFT calculation of molecular structure and electronic structure

To understand the formation MPMS and the molecular structure of the resulting MPMS, we conducted density functional theory (DFT) calculations using the Vienna ab-initio simulation package (VASP) [24,25] with projector augmented wave (PAW) pseudopotentials [26,27]. Based on average atomic ratio analysis from EDX analysis, the MPMS structure is modeled by a close-packing configuration, with 32 P atoms and 1 CTAB molecule in the supercell, as shown in Fig. 5-3g and 3h. The reciprocal space was sampled by Γ-centered Monkhorst-Pack scheme [28] with 7x1x3 k-points. Both the cell parameters and the internal atomic coordinates

are fully relaxed using Perdew–Burke–Ernzerhof (PBE) exchange-correlation functional [29]. Significantly, the relaxed structure gives an interlayer distance of 11.41 Å, matching well with the 11.27 Å value determined by XRD and cross sectional TEM. Furthermore, the relaxed structure also shows a 2.9 % expansion in the armchair direction compared with that of BP calculated using the same method and negligible lattice parameter change in the zigzag direction, consistent with our planar TEM observations (Supplementary Text 3 for more details). We attribute the strain to the repulsion between CTAB molecules, which leads to the expansion of BP lattice, similar to the strain observed in alkali-metal intercalated graphite [30].

The PBE calculations also show a bandgap expansion of 0.24 eV from monolayer phosphorene to MPMS, consistent with the increase of optical band gap. For accurate evaluation of the electronic structure, we used B3PW91 functional as implemented in the CRYSTAL14 package [31,32], and all-electron 6-31G(d) basis sets of double-ζ quality were used for H, C, N, O, P and Br. An extra-large grid, consisting of 75 radial points and 974 angular points, was used for accurate integration, and the reciprocal space was sampled by Γ-centered Monkhorst-Pack scheme with a 7×1×3 grid. As show in Fig. 5-4a and 4b, MPMS have enlarged bandgap at 2.13 eV with 0.19 eV increment compared with monolayer phosphorene at 1.94 eV, which is in agreement with experimental observed bandgap of 2.26 eV in MPMS, compared with monolayer BP bandgap at around 2 eV [20,21]. In addition, there are additional bands within the band gap of MPMS in Fig. 5-4b that are marked in gray dotted line, which are mainly composed of Br atomic p orbitals (ranging from 24% to 56%, larger than the averaged contribution of 8%~4% from black phosphorus unit (P_4)), while the orange VBM-0 bands are with contributions from P dominating over from Br (less than 10%). Our

calculations of the frequency dependent dielectric matrix (at the PBE level) indicate that in the isolated monolayer BP, the VBM-1 (Fig. 5-4e) band and VBM-0 (Fig. 5-4d) have symmetrically equivalent charge density distributions, and thus they are very close to each other in energy, and they both contribute to the first absorption peak (Fig. 5-4a), as they both have significant overlap with the CBM band state (Fig. 5-4c). However, for MPMS, only the VBM-1 (Fig. 5-4h) has largest overlap with CBM (Fig. 5-4f) and contributed significantly to the transition from VBM-1 to CBM. For VBM-0 (Fig. 5-4g) and CBM (Fig. 5-4f), due to small states overlap with each other, the transition between them is very limited. So the optical transition bandgap of MPMS was determined by the transition from VBM-1 (Fig. 5-4h, green band in Fig. 5-4b) to CBM (Fig. 5-4f, red band in Fig. 5-4b), which matched well with our experimental observation of enlarged bandgap in MPMS.

F. Raman spectroscopic studies

We have also used Raman spectroscopic studies to probe the structural evolution from BP to MPMS. Raman studies show that all three characteristic BP Raman modes remain after intercalation, yet with considerable intensity wakening (by ~ 40 times) (Fig. 5-5a). A close analysis reveals considerable peak broadening and apparent peak position shifts. The A_g^1 mode is slightly red shifted from BP 360.93 cm^{-1} to MPMS 359.77 cm^{-1} (Fig. 5-5b), whereas B_{2g} and A_g^2 modes are blue shift from 437.98 cm^{-1} in BP to 438.21 cm^{-1} in MPMS (Fig. 5-5c) and 465.45 cm^{-1} in BP to 465.96 cm^{-1} in MPMS (Fig. 5-5d), respectively. As depicted as atomic motions of three lattice vibrational modes in the insets of Fig. 5-5b to 5d, these peak shifts can be qualitatively understood as a consequence of ~3% armchair direction strain as observed in the TEM analysis and in the simulated structure [33]. Basically, the armchair

expansion originates from CTAB repulsion each other. Thus, the molecular orienting in zigzag direction exerts tiny external force along armchair direction to separate slightly two non-bonded but neighboring phosphorus atoms, which will contribute positively to projected components of A_g^1, but negative for projected motion of A_g^2. This leads to the red shift for A_g^1 and the blue shift for A_g^2. Though atomic motions associated with B_g^2 occur mostly along the zigzag direction, the armchair expansion will harden the zigzag direction atomic motions indirectly, resulting in a very small blue shift of B_g^2. Therefore, the energy spacing between A_g^1 and B_g^2 or between A_g^1 and A_g^2 modes increases under armchair stretching [33]. Raman studies of MPMS also reveal a new peak around 1460.1 cm^{-1} in MPMS (Fig. 5-12), which corresponds to CH_3 antisym deformation or CH_2 scissors vibration, further confirming successful intercalated CTAB inside BP monolayers.

G. Electrical properties and stability analysis

Due to its intrinsic instability, monolayer phosphorene has been difficult to access and its intrinsic properties are insufficiently explored to date. With the successful preparation of MPMS, we have further explored their electronic properties in depth. To reveal the electrical properties change before and after the intercalation process for same BP nanosheet, back gate BP and MPMS transistors were studied. In general, the output characteristics (source drain current vs. source drain voltage: I_{sd}-V_{sd}) for both BP and MPMS show linear relationships (insets of Fig. 5-6a, 6b), suggesting the absence of an obvious contact barrier and an acceptable Ohmic contact. Back gate transfer characteristics of pristine BP show the typical p-type behavior with an on/off ratio <10 and mobility up to 721 $cm^2V^{-1}s^{-1}$ (Fig. 5-6a). The MPMS device retains p-type properties with a respectable mobility of 328 $cm^2V^{-1}s^{-1}$ (Fig.

5-6b), which outperformed the best few-layer BP devices and show comparable mobility but much higher on/off ratio than thin BP devices (see Fig. 5-13 for a statistical analysis of the electrical properties of six MPMS devices and their comparison with few-layer and thin BP devices from other recent studies) and close to its theoretical limit (250 to 400 $cm^2V^{-1}s^{-1}$) [34-36]. Significantly, the MPMS device can be completely switched off with a greatly increased current on/off ratio. For example, a current modulation up to 10^7 is achieved in MPMS structure at V_{sd} of 0.01 V (Fig. 5-6c), in contrast to an on/off ratio <10 for the same BP before intercalation. This on/off ratio of >10^7 represents the highest on/off ratio ever achieved in phosphorene or thin BP nanodevices [2,8].

To further understand the electrical properties of MPMS, we have also explored the transport properties of MPMS FETs at various temperatures from 1.9 K to 300 K (Fig. 5-6d, 6e). In general, the linear output characteristics are retained at low temperature down to 1.9 K, suggesting good Ohmic contact of the device. With the decreasing temperature, the on-current more than doubled from 1.74 μA at 300 K to 3.85μA at 1.9 K (Fig. 5-6d and inset). In addition, the field-effect mobility extracted from the transfer characteristics increased to 599 $cm^2V^{-1}s^{-1}$ at 1.9 K, compared with initial mobility of 289 $cm^2V^{-1}s^{-1}$ at 300 K. In the phonon limited temperature range (100–300 K), the mobility best fits the expression $\mu \sim T^{-\gamma}$ with the exponent γ around 0.73 for MPMS. A power law dependence with a positive exponent is indicative of a phonon scattering mechanism, which is consistent with other studies of thin BP that show band-like transport [2,37].

Importantly, with the sandwiching and encapsulation of monolayer phosphorene between molecular monolayers, the environmental stability of the material is greatly increased. For

example, comparing a BP device and a MPMS device with similar on-current, the MPMS show no significant electrical degradation for as long as 300 hours exposure in ambient condition; this contrasts with the BP device that shows serious degradation after 20-30 hours exposure (Fig. 5-6f). We attribute this greatly improved stability of MPMS to the special superlattice structure, in which each phosphorene monolayer is sandwiched/encapsulated by the molecular layers, which considerably slows the oxygen and water diffusion believed to be the main cause of BP degradation [8,38,39]. It is important note that electrical stability of MPMS compares favorably with those of BN-encapsulated/passivated or Al_2O_3 passivated few-layer BP devices reported recently. Furthermore, the intercalation process of MPMS does not involve any complex fabrication steps and prevents the potential fabrication-induced performance degradation or unavoidable exposure to ambient atmosphere (table 1) [8,37,40,41].

H. Lateral BP-MPMS heterojunctions

Lateral integration of 2D materials by using either the same material with different dopants at two ends [42,43] or two different materials with opposite doping type [44,45] is an exciting topic for creating functional nanodevices. However, lateral integration of phosphorene based structure has not been sufficiently studied due to the difficulty in controllable and selective doping and the complexity in fabricating such devices. Inspired by superior electrical properties of MPMS, Fermi level mismatch between BP and MPMS as well as high controllability of intercalation process, we fabricated lateral BP-MPMS heterojunctions by partial interaction of a BP flake. Since the insertion of CTAB into BP occurs through the edges, partial intercalation can be achieved by selectively opening an intercalation window on a PMMA-covered BP and controlling the diffusion-limited

intercalation time. The exposed edges underwent electrochemical reactions, forming a lateral junction between the intercalated MPMS and the passivated BP. Photoluminescence spectra mapping of a typical lateral BP-MPMS heterostructure show clear PL signal in the MPMS region and the absence of PL signal in the BP part (Fig. 5-7a). Similarly, corresponding Raman spectra mapping centering at 438 cm^{-1} showed considerably stronger signal in the BP region than that in the MPMS region (Fig. 5-7b). After standard electron beam lithography and metal deposition process to contact the BP region and MPMS region separately, we obtained a BP-MPMS heterojunction device (Fig. 5-7c and inset of 7f), which is schematically illustrated in the inset of Fig. 5-7d. Considering the large bandgap difference between monolayer phosphorene (MPMS) and BP, we expect a diode-like rectification from the band diagram (Fig. 5-7e) and indeed we observed it (Fig. 5-7f) [46]. This demonstration of a unique lateral BP-MPMS heterojunction diode represents an essential step towards functional phosphorene electronics and optoelectronics.

I. Discussion and summary

With a unique two-dimensional geometry, a relatively high mobility, a suitable layer-number dependent direct bandgaps, phosphorene provides an alternative atomically thin semiconductor for a new generation of electronic and optoelectronic devices. The formation of MPMS structure with superior current modulation, intrinsic optical bandgap, outstanding stability, and the demonstration MPMS transistors with high mobility and record-high on/off ratio and lateral BP-MPMS heterojunction diodes represents exciting advancements for phosphorene electronics both fundamentally and technically. This MPMS transistor and lateral BP-MPMS can be applied directly to functional phosphorene electronics devices, such

as high performance radio frequency (RF) transistors or MPMS/MoS_2 vertical heterojunction transistors, further opening up exciting opportunities for creation of a wide variety of integrated devices, ranging from complementary logic devices, photovoltaics, photodetectors to light emitting devices. In addition to the intercalation dynamics study of BP, our *in situ* electro-chemical-optical measurement (IS-ECOM) platform provides a general means to study diverse 2DLMs such as MoS_2 and graphene to produce a wide array of 2D superlattices with tunable electronics and optoelectronic properties, as already demonstrated in our preliminary studies. By varying the size and functional group of the molecules, it is also possible to further tune the intercalation parameters, leading to superlattices with variable interlayer distances, controllable doping and tunable electronic properties. Our study thus defines a general strategy to preparing 2D superlattices and opens up a new pathway to tailoring and taming the electronic properties of 2D materials for functional electronics and optoelectronics. This main idea of this study was submitted for potential publication.

J. Materials and Methods

BP FET fabrication.

BP was synthesized under a constant pressure of 10 kbar by heating red phosphorus （99.999 %） to 1,000 °C and slowly cooling to 600 °C at a cooling rate of 100 °C per hour. Standard mechanical exfoliation method was employed to isolate thin BP on 300nm SiO_2/Si substrate in N_2 filled glove-box. The thin BP transistors were fabricated using electron-beam lithography (EBL) followed by electron-beam deposition of 10/80 nm Cr/Au metal thin films.

Structural characterizations.

SEM characterization was performed by FEI Nova Nano 230 at 15kV voltage. TEM cross section sample of BP was made through FIB cutting from thin BP. TEM cross section sample of MPMS was made though sonication of thick intercalated BP flakes to make MPMS nanoprism, then dipped the MPMS nanoprism onto TEM grid for imaging. Planar TEM sample was made by directly transferring mechanical exfoliated thin BP on TEM grid for the BP characterization; then using TEM grid with thin BP on top for intercalation process, then imaging the same intercalated sample. TEM characterization was performed by FEI Titan at 300kV accelerating voltage. XRD samples were prepared by transferring mechanical exfoliated thin BP to 300nm SiO_2/Si substrate with a 50/50 nm Ti/Au film on top. The whole metal covered substrate with thin BP was directly used for intercalation process, and then characterized by PANalytical XPert Pro power X-ray diffractometer with 45 kV voltage, 40 mA emission current and 1/4° beam slit. The micro-Raman and micro-PL studies were conducted using a Horiba Lab RAM HR Evolution confocal Raman system with Ar ion laser (488 nm and 633nm) excitation.

K. Supplementary Text

<u>1. Intercalation chemistry of BP</u>

The basic of this electrochemical reaction dictate that electrons are transferred from the HOMO level of the cathode/reducing agent towards the LUMO of the oxidizing agent on the anode. On the cathode, two bromide ions acts as the reducing agent each losing an electron to form Br_2, requiring around 1 V of electrochemical potential. On the anode side, electrons are pumped into the BP conduction band. The additional electron causes BP to be negatively charged. To stabilize the additional electron, $(CH_3)_3NC_{16}H_{33}^+$ molecules insert itself between

the BP layers gap through edges acting as a counter ion.

The start of the major reaction observed at ~ 1 V can be explained by its HOMO/valence band and LUMO/conduction band difference around 0.35 eV and ~ 1 eV *Br-* sub-reaction electrochemical potential. The first insertion of $(CH_3)_3NC_{16}H_{33}^+$ does not require high applied potential due to the low (~0.35 eV) band gap of the bulk BP. As the intercalation continuing, the HOMO/LUMO gap of BP/substrate increases, hence causing it to become harder for the next reaction to occur. The intercalation decouples the neighboring BP layers and reduces the effective layer thickness, leading to blue shift of the photoluminescence peak wavelength, and a final peak was recorded at ~2.26 eV for MPMS, representing the highest observed optical gap.

During reaction, it's clear that Br_2 was formed at cathode with the emergence of the darker yellow Br_2 solution. However, after the electrochemical potential was withdrawn, due to high activity of Br_2, it will re-react with phosphorene$^-$CTA$^+$ layers quickly to form final phosphorene/CTAB layered superlattice structure, which is consistent with the TEM EDX analysis and the DFT simulated structure.

2. Stepwise reaction mechanism

Due to strong layer-number dependent bandgap of black phosphorus, stepwise reaction mechanism is proposed mainly based on the characteristic stepwise electrochemical current curve[47] and the corresponding photoluminescence spectra of bulk, few-layer, trilayer, bilayer and monolayer phosphorene as described in the main text. In addition, XRD spectra taken at different intercalation stage on a small $Au/SiO_2/Si$ substrate with couple of BP flakes or bulk

sample was observed with peak around ~16.34 Å, ~ 26.41 Å due to bilayer or trilayer structure (Supplementary Fig. 3). The properties of CTA^+ with one positive charge and relative large molecular size was expected to stepwisely intercalated based on modeling study.[48]

In addition, for each region labeled with specific structure, like bilayer region, it means the majority of structure is bilayer, but it also included other structure, like trilayer, which can be explained from the bilayer PL spectra, where weak trilayer shoulder peak was observed as well. Even for the monolayer structure, from its XRD spectrum, tiny pristine BP peak can be observed as well. So for most intermediate structures, including few-layer, trilayer, bilayer, it's a mixed phase at some extent. Very careful scan times, scan step, scan duration and stop voltage should be adjusted to for relatively pure structure. Since monolayer structure is the final step, it's relatively easier to reach compared with those intermediate states.

The intercalation scan times, scan step, step duration and stop voltage have large effect on the final structure as well. Due to the diffusion limited intercalation progress, the structure may not form within one fast scan. To better control the intercalated process, the multi-scan method was employed in this study. In addition, too large scan step may lead to sample cracking at higher voltage. Too short step duration time are the reason for incomplete intercalation as limited by CTAB molecular supply or CTAB diffusion inside BP. Incorrect stop voltage will lead to strongly mixed phase, especially in the intermediate states. Stop voltage above 3V for long time will result in sample cracking.[49] Sometimes, multi-scan with different parameters may be employed to slowly tune the structure from mixed phase to relative pure phase by increasing the intercalation degree in small ratio. Those parameters

setting are related to sample size, thickness, shape (sharp or rough edges) and expected structure. More systematic study with precise intermediate structure control may be isolated in future work.

3. Simulated MPMS structure parameters and bandgap

According to DFT calculations using the VASP with PAW pseudopotentials, lattice parameter in armchair direction changed from 4.62 Å of BP to 4.75 Å of MPMS with 2.9 % increment. For the zigzag direction, the change is negligible comparing 3.30 Å of BP with 3.28 Å of MPMS. For the bandgap of MPMS, we also calculate a bandgap of 1.14 eV with 0.24 eV increment by using PBE compared to 0.90 eV for monolayer phosphorene. It is noted that PBE underestimates band gaps but leads to bandgap increment of 0.24 eV of MPMS compared with monolayer phosphorene.

L. Figure and Legends

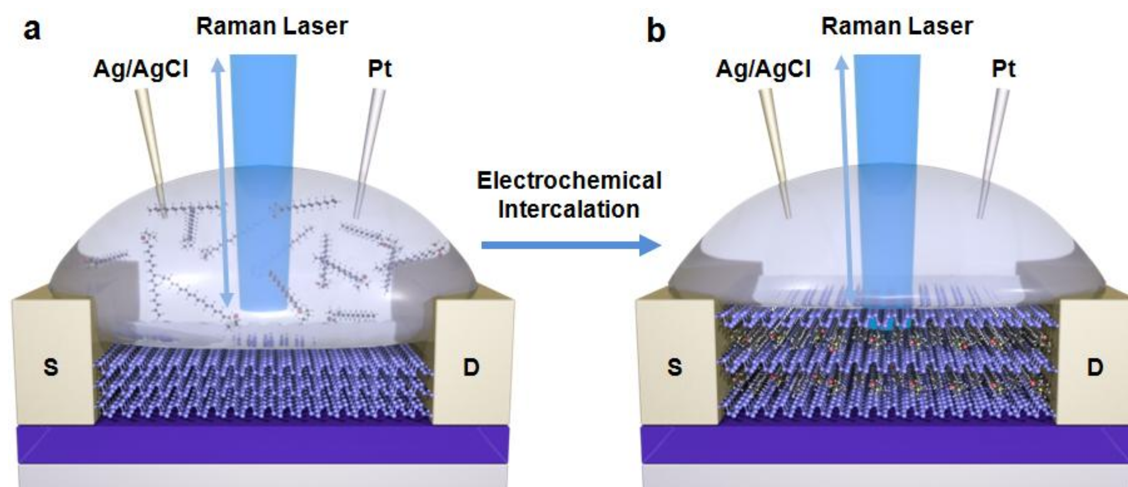

Figure 5-1. *in situ* electrochemical-optical measurement (IS-ECOM) platform to monitor electrochemical intercalation in real time. a and **b,** schematics of the IS-ECOM platform for the BP intercalation process from BP (**a**) to MPMS (**b**)**.** The IS-ECOM system can allow to simultaneously monitor electrochemical current, source-drain current, and photoluminescence/Raman spectra during the electrochemical intercalation process.

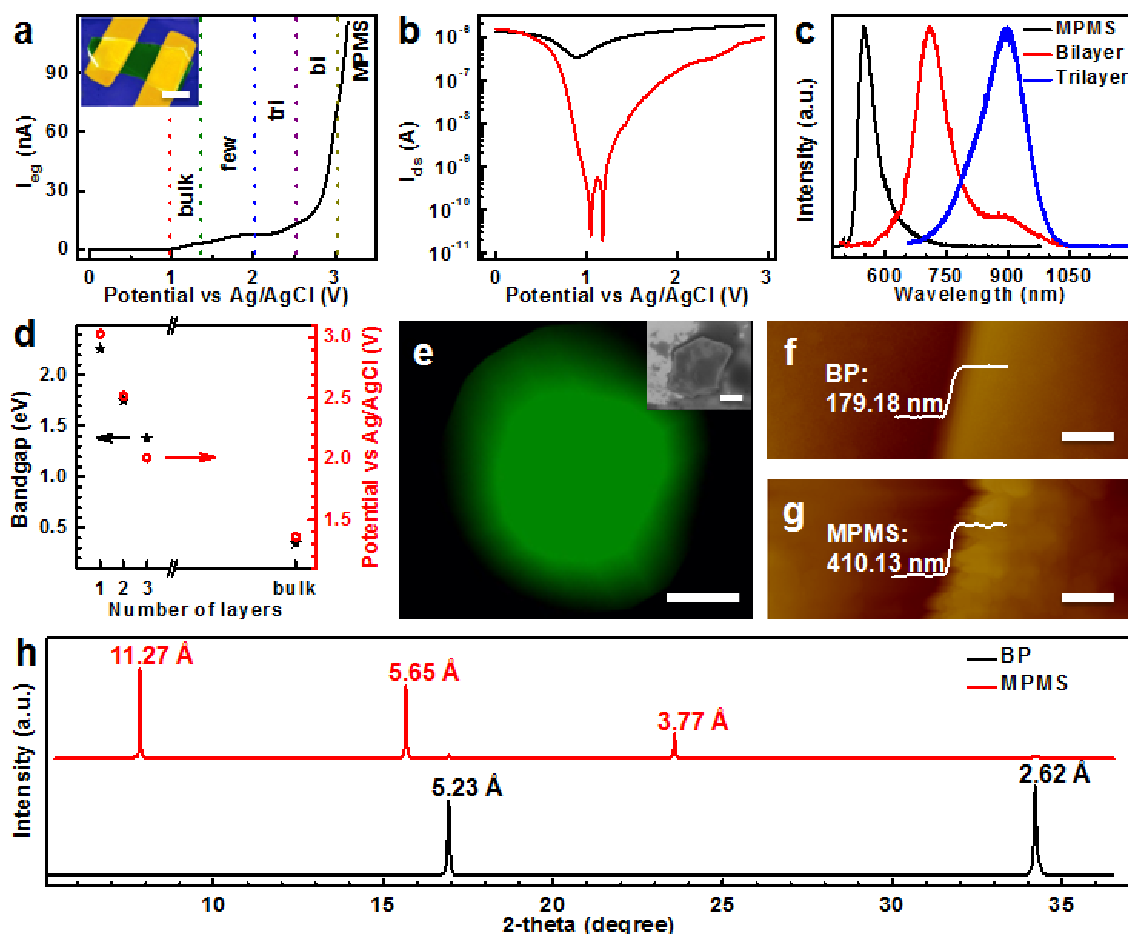

Figure 5-2. Structural and property evolution from BP to MPMS during the dynamic electrochemical intercalation process. a, Electrochemical current as a function of the applied electrochemical potential from 0 V to ~ 3 V, showing stepwise reactions with 6 distinct regions during the BP intercalation with CTAB. Inset: false-color SEM image of MPMS transistors. Scale bar: 5 μm. **b**, ionic gate transfer characteristics of the first scan (black, BP) and the last scan (red, MPMS) monitored simultaneously by applying the same electrochemical potential during MPMS formation at 0.01 V source-drain bias. **c**, photoluminescence signals observed at 898 nm (1.38eV), 710 nm (1.75eV) and 548 nm (2.26 eV) during different stages of intercalation, roughly corresponding to band edge emission from trilayer, bilayer and monolayer phosphorene. **d**, The bandgap/electrochemical potential vs. layer number relationship showing a good correlation between electrochemical potential and the corresponding bandgap at bulk, bi, tri and monolayer regions. **e**, Photoluminescence mapping centering at 550.0 nm with similar intensity demonstrating the relatively uniformity of the resulting MPMS. Inset: the corresponding SEM image of photoluminescence mapping sample; scale bar: 3 μm. **f** and **g,** AFM images of a BP flake (**f**) and the resulting MPMS (**g**) after CTAB intercalation, demonstrating the overall thickness increase by about 130 %. Scale bar: 300 nm. **h**, X-ray diffraction spectra of BP and MPMS verifying the interlayer distance expansion from 5.23 Å (16.93°) of BP (black) to 11.27 Å (7.84°) of MPMS (red).

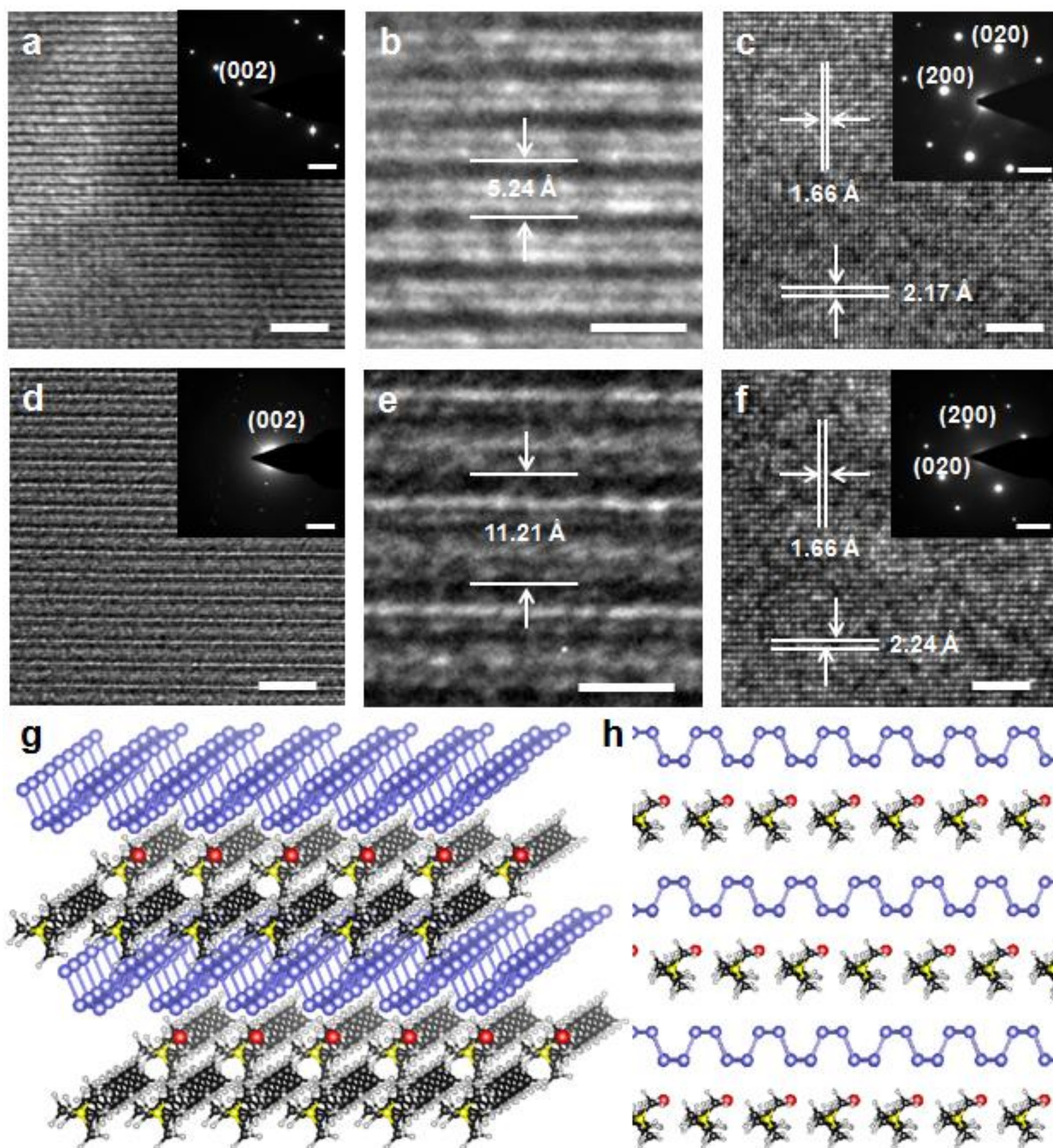

Figure 5-3. TEM characterization of structure evolution from BP to MPMS. a and **d** TEM cross section image comparison between BP (**a**) and MPMS (**d**) to show well-ordered intercalation of CTAB layer into BP monolayers. Scale bar: 3 nm; Insets are the corresponding electron diffraction to verify the increased interlayer distance. Scale bar: 2 1/nm. **b** and **e** are magnified high-resolution cross sectional TEM images to further demonstrating the insertion of CTAB layer between BP layers to form MPMS with the interlayer distance increasing from 5.24 Å in BP (**b**) to 11.21 Å in MPMS (**e**). Scale bar: 1 nm; **c** and **f**, Planar TEM images of BP **c** and MPMS **f** showing the lattice parameter expansion in armchair direction from 2.17 Å in pristine BP to 2.24 Å in MPMS and negligible change in zigzag direction (1.66 Å for both BP and MPMS). Scale bar: 2 nm; Insets: electron diffraction of the corresponding TEM images to confirm the lattice parameter change in (200) and (020) and directions; Scale bar: 5 1/nm. **g** and **h**, three-dimensional (**g**) and cross sectional (**h**) atomic structure view of simulated structure of MPMS, verifying the 11. 41 Å interlayer distance and 2.9 % expansion in armchair direction.

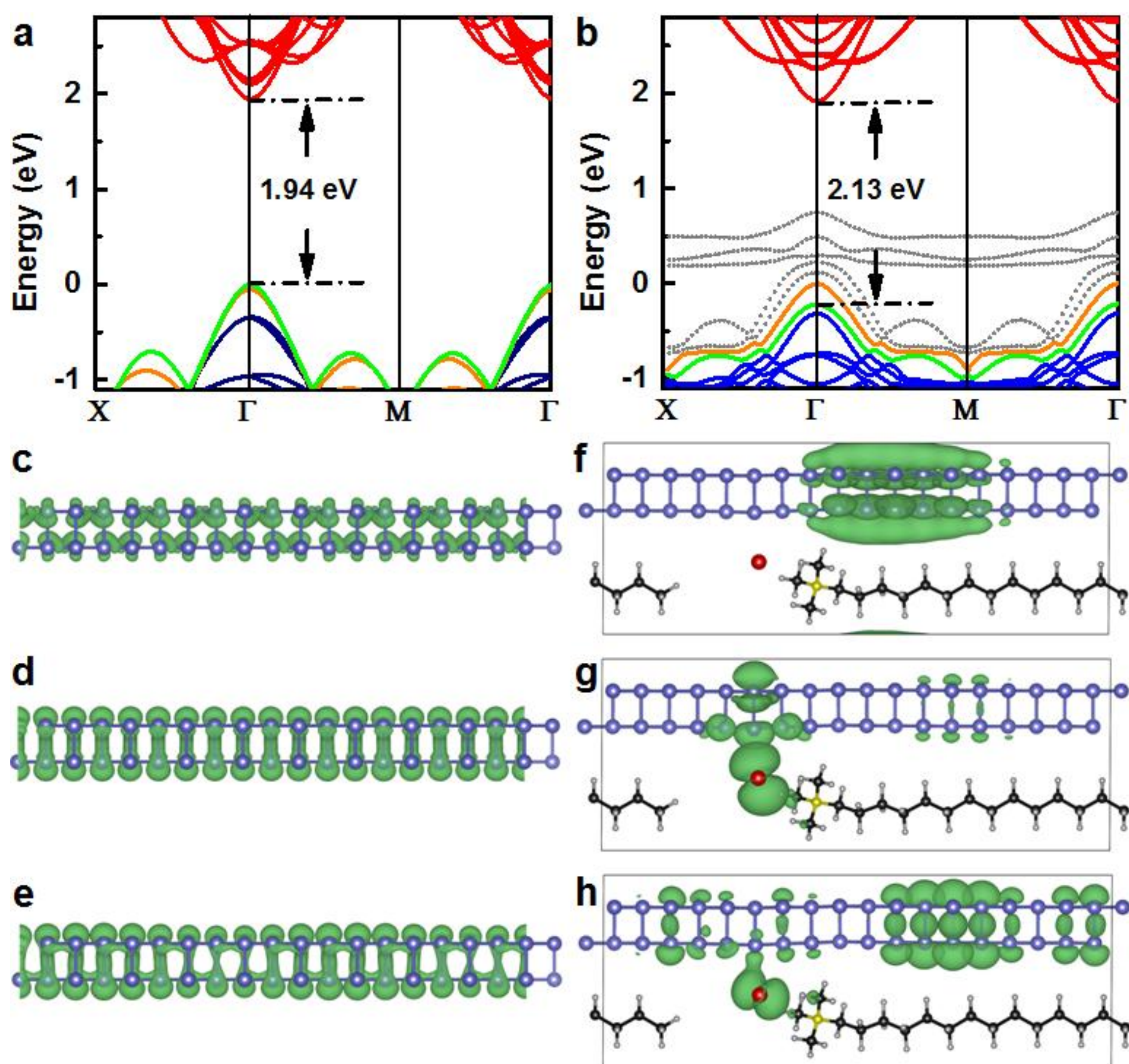

Figure 5-4. The calculated electronic band structure evolution from BP to MPMS. a and **b**, electronic structure of BP (**a**) and MPMS (**b**), demonstrating the enlarged bandgap from 1.94 eV in BP to 2.13 eV in MPMS as determined by the transition from first VBM-1 (green) and CBM (red). The newly introduced bands of MPMS marked as gray dotted lines are mainly from Br atomic p orbitals and the orange VBM-0 band mainly (~ 90%) from P, but almost didn't contribute to the optical transition due to its very small overlap with CBM. **c**, **d** and **e**, monolayer phosphorene charge density distribution of CBM (red in **a**), VBM-0 (orange in **a**) and VBM-1 (green in **a**), showing the transition bandgap determined by CBM and VMB-0/VMB-1 (energy very close); **f**, **g** and **h**, MPMS charge density distribution of CBM (red in **b**), VBM-0 (orange in **b**) and VBM-1 (green in **b**), showing the transition bandgap determined by VBM-1 and CBM due to large overlap of charge density.

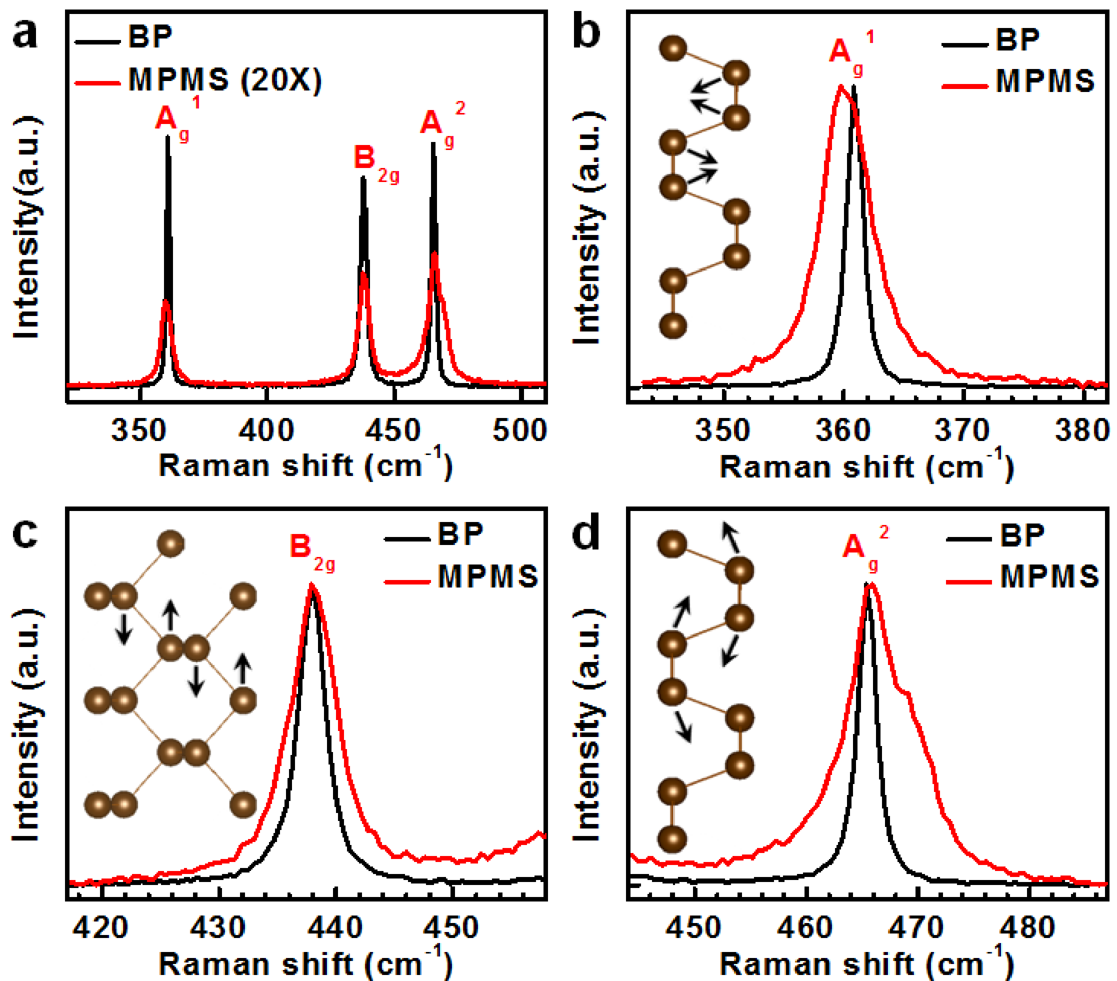

Figure 5-5. Raman spectra characterization of BP and MPMS. a, Raman spectra to compare the relative peak intensity and FWHM evolution from pristine BP (black) to MPMS (red). The MPMS spectrum is multiplied by 20 times for easy comparison. **b-d**, A_g^1, B_{2g} and A_g^2 mode comparison between pristine BP and MPMS to show red shift, blue shift and blue shift after MPMS formation, respectively. Insets: schematic illustration of atomic motion of each vibration modes.

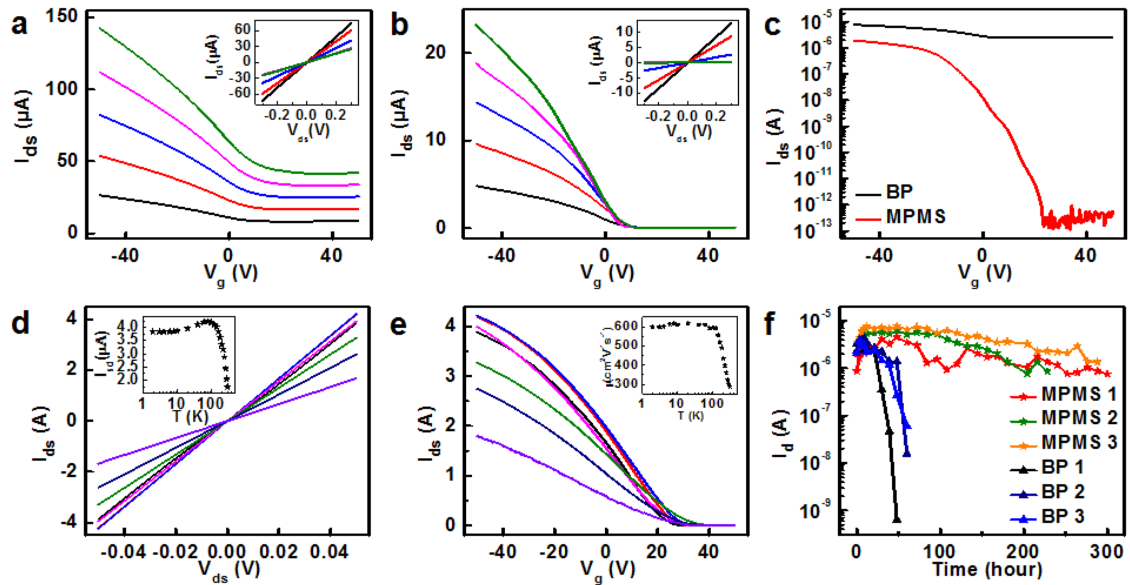

Figure 5-6. Electrical properties evolution from BP to MPMS and stability comparison. a and b, back gate transfer characteristics of pristine BP and MPMS as the source-drain bias is stepped from 0.1 V (black curve) to 0.5 V (green curve) bias with 0.1 V step; insets: output characteristics of BP (**a)** and the corresponding MPMS (**b)** after CTAB intercalation, showing the absence of obvious contact barrier and acceptable Ohmic contact. **c**, comparison of typical transfer characteristics between BP (black) and MPMS (red) at a source drain bias of 0.01 V, demonstrating an on/off ratio $>10^7$ in MPMS vs. <10 in BP. **d**, output characteristics of MPMS at various temperature from 1.9 K (black) to 300 K (violet). Inset: on-current vs temperature of MPMS. **e**, transfer characteristics of MPMS at various temperature from 1.9 K (black) to 300 K (violet). Inset is the temperature dependence of mobility. **f,** Comparison of electrical stability between three MPMS (star marked) and three BP (triangle marked) devices with similar starting on-current, highlighting exceptional stability of MPMS without obvious electrical degradation for as long as 300 hours, which is more than 10-15 times longer lifetime than pristine BP.

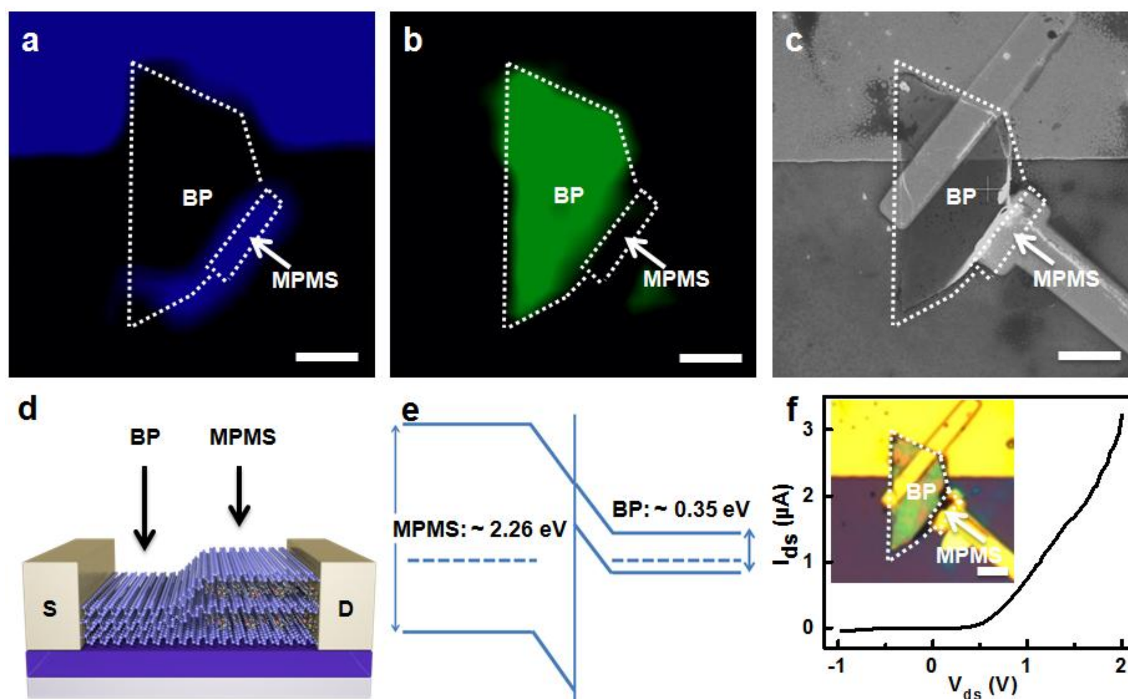

Figure 5-7. Lateral BP-MPMS heterojunction. a, Photoluminescence (at 553 nm) mapping of a lateral BP-MPMS heterostructure to emphasize the MPMS part. Scale bar: 3 μm. The signal in the electrode area is due to a scattering induced background. **b,** The corresponding Raman spectral mapping centered at 438 cm^{-1} to show the main BP region with stronger Raman signal. Scale bar: 3 μm. **c,** SEM image to show the lateral BP-MPMS heterojunction device. Scale bar: 3 μm. **d,** Schematic illustration of a lateral BP-MPMS heterojunction. **e**, Band diagram of the BP-MPMS heterojunction. **f**, The typical diode characteristics of a lateral BP-MPMS heterojunction; inset: optical microscope image of the corresponding BP-MPMS heterojunction. Scale bar: 3 μm.

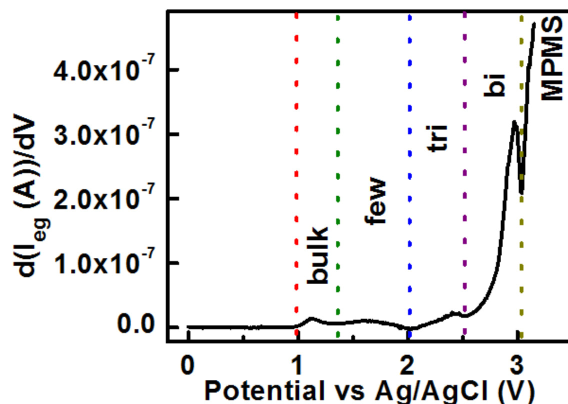

Figure 5-8. Stepwise reaction mechanism and its partition map. First derivative of electrochemical current in Fig. 2a. By analyzing original current curve and local minimum of first derivative, the stepwise reaction can be clearly identified, i.e. no major intercalation for 0-1.0 V (over-potential for Br^- sub-reaction),1.0-1.4 V for few-layer structure formation, 1.4-2.0 V for few-layer BP formation, 2.0-2.5 V for trilayer BP formation, 2.5-3.0 V for bilayer BP formation and beyond 3.0 V for MPMS formation, which is also consistent with bandgap evolution from bulk, few, tri, bi and monolayer phosphorene.

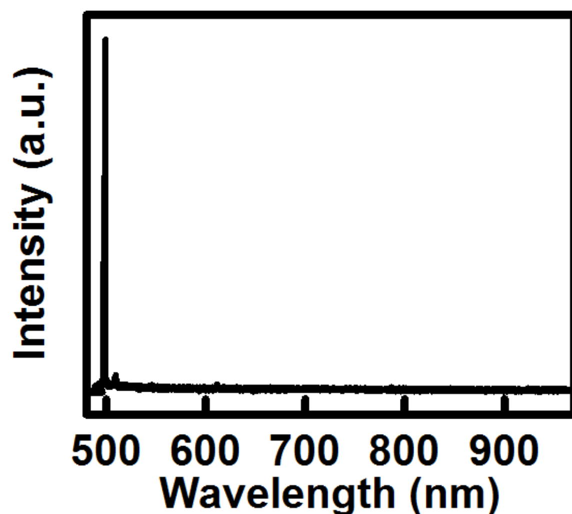

Figure 5-9. Photoluminescence spectrum of bulk black phosphorus. Photoluminescence spectra of pristine thick BP sample taken from the bulk region in Fig. 5-2a, just showing the strong Raman peak, but no any observable PL peak at same range in Fig. 5-2c.

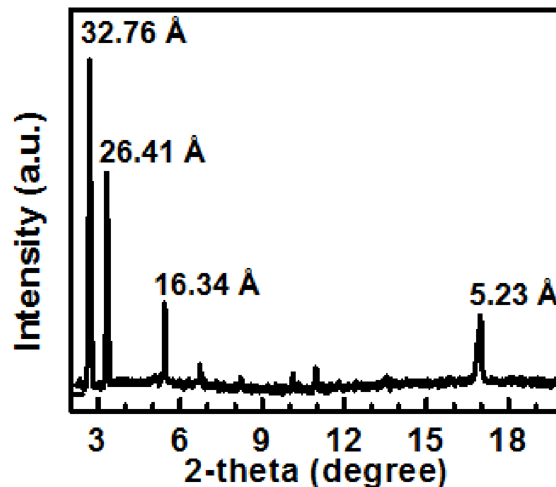

Figure 5-10. XRD of mixed few-layer phosphorene molecular superstructure. XRD peak with interlayer distance at 32.76 Å (five-layer phosphorene-molecular structure or mixed structure), 26.41 Å (four-layer phosphorene-molecular structure or mixed structure) and 16.34 Å (bilayer phosphorene-molecular structure), indicating the mixed structure during transition region. It's noted that peak with 5.23 Å is originated from non-intercalated BP. It is noted that small peak are high order peak of mixed structure.

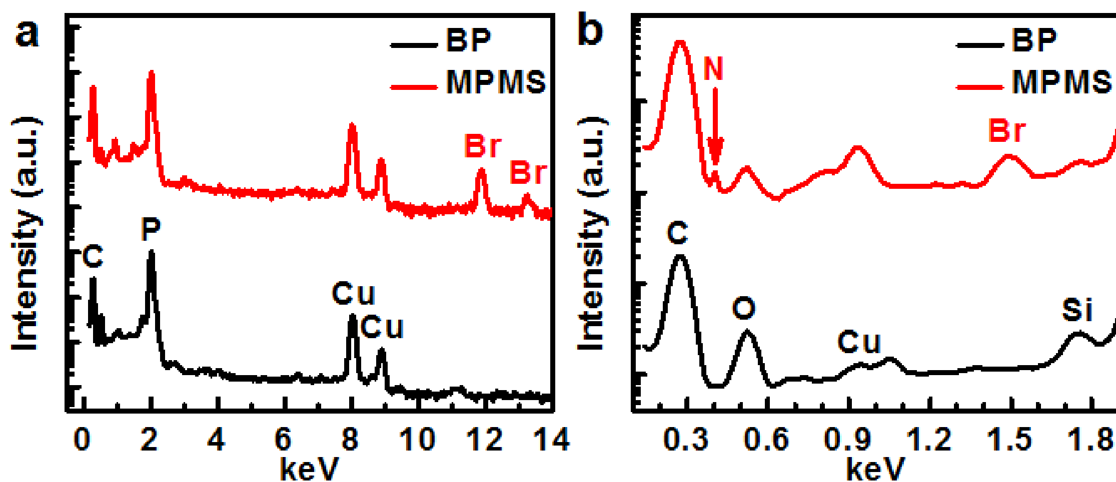

Figure 5-11. TEM EDX spectra of BP and MPMS. a and b showed the TEM EDX spectra at different range from same cross sectional TEM samples, showing the existence of Br and N after intercalation. Three average spectra gave atomic ratio of P : N : Br is 33.2 : 1.2 : 1.0.

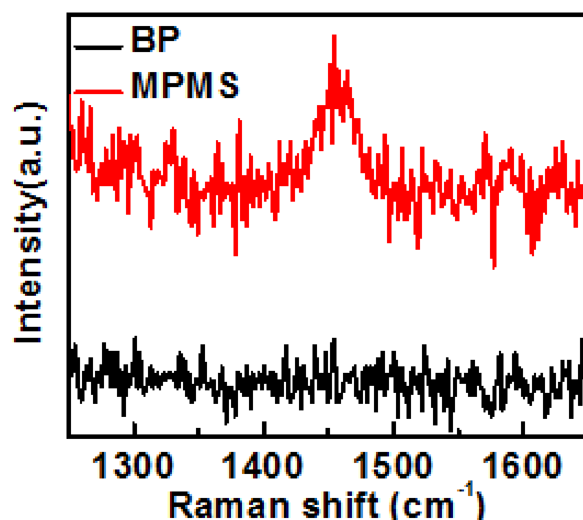

Figure 5-12. Raman peak of CH_3 antisym deformation or CH_2 scissors vibration from CTAB. Raman peak around 1460.1 cm^{-1} indicating the existing of CH_3 antisym deformation or CH_2 scissors vibration and successful intercalation of CTAB inside BP monolayers.

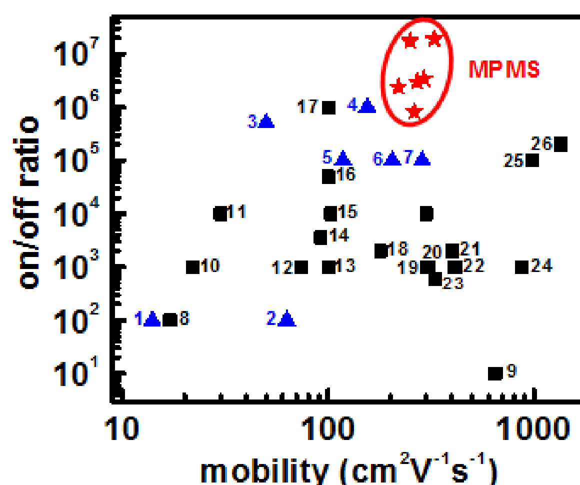

Figure 5-13. Statistical analysis of six MPMS devices performance compared with few-layer and thin BP devices of recent other studies. Six MPMS devices (red star) show average mobility of 270 cm^2 V^{-1} s^{-1} and averaged on/off ratio of $8.6*10^6$. As comparison, we listed recent studies of few-layer (less than 5 nm, marked as blue triangle) and thin BP (5 nm to 15 nm, marked as black square). It's clear that MPMS devices outperformed the best few-layer BP devices as for the mobility and on/off ratio and show comparable mobility but much higher on/off ratio of thin BP devices. Data points indexed are adapted: data 1 from Ref. [50], data 2 from Ref. [41], data 3 from Ref. [51], data 4 from Ref.[52], data 5 from Ref. [40], data 6 from Ref. [51], data 7 from Ref. [10], data 8 from Ref. [11], data 9 from Ref. [51], data 10 from Ref. [53], data 11 from Ref. [54], data 12 from Ref. [55], data 13 from Ref. [56], data 14 from Ref. [57], data 15 from Ref. [58], data 16 from Ref. [54], data 17 from Ref. [8], data 18 from Ref. [54], data 19 from Ref. [59], data 20 from Ref. [60], data 21 from Ref. [3], data 22 from Ref. [61], data 23 from Ref. [62], data 24 from Ref. [63], data 25 from Ref. [2], data 26 from Ref. [37].

Table 1. Device key characteristics compassion between MPMS and other recent studies

Ref.: BP thickness, passivation approach,	bandgap (eV)	mobility ($cm^2/V/s$)	on/off ratio	electrical stability (hour)
This work (MPMS)	**2.26**	**328**	**1.9E7**	**300+**
Ref. [8]*: 10 nm, aryl diazonium passivation*	n.a.	~ 100	**1E6**	83+
Ref. [40]*: 5 nm, BN passivated in inert air*	n.a.	118 (200K)	1E5	48+
Ref. [37]*: 8 nm, BN encapsulated*	n.a.	n.a.	2E5	150+
Ref. [41]*: 4.5 nm, BN passivated;*	n.a.	63	100	n.a.
Ref. [20]*: monolayer*	1.73	n.a.	n.a.	n.a.
Ref. [10]: 5 nm, *not passivated*	1.45	**286**	1E5	n.a.
Ref. [7]*: Monolayer, ALD Al2O3 passivated;*	**1.84**	n.a.	n.a.	144 + (PL)
Ref. [55]: 8.9 nm, *ALD AlO_x passivated*	n. a.	74	1e3	**175**

Notes: Compared with key improvements of few-layer (less than 5 nm) phosphorene in past three years, this study represented a fundamental advance of few-layer and monolayer phosphorene intrinsic properties demonstration including highest optical bandgap, highest few-layer mobility, highest on/off ratio and extraordinary stability.

M. References

1. Bridgman, P. W. Two new modifications of phosphorus. *J Am Chem Soc* **36**, 1344-1363, doi:Doi 10.1021/Ja02184a002 (1914).

2. Li, L. K. *et al.* Black phosphorus field-effect transistors. *Nat Nanotechnol* **9**, 372-377 (2014).

3. Wang, H. *et al.* Black phosphorus radio-frequency transistors. *Nano Lett* **14**, 6424-6429 (2014).

4. Perello, D. J., Chae, S. H., Song, S. & Lee, Y. H. High-performance n-type black phosphorus transistors with type control via thickness and contact-metal engineering. *Nature Communications* **6**, doi:Artn 7809 10.1038/Ncomms8809 (2015).

5. Yuan, H. *et al.* Polarization-sensitive broadband photodetector using a black phosphorus vertical p–n junction. *Nat Nanotechnol* **10**, 707-713 (2015).

6. Deng, Y. *et al.* Black Phosphorus–Monolayer MoS2 van der Waals Heterojunction p–n Diode. *Acs Nano* **8**, 8292-8299 (2014).

7. Pei, J. *et al.* Producing air-stable monolayers of phosphorene and their defect engineering. *Nat Commun* **7**, doi:10.1038/ncomms10450 (2016).

8. Ryder, C. R. *et al.* Covalent functionalization and passivation of exfoliated black phosphorus via aryl diazonium chemistry. *Nat Chem* **8**, 598-603, doi:10.1038/Nchem.2505 (2016).

9. Island, J. O., Steele, G. A., van der Zant, H. S. & Castellanos-Gomez, A. Environmental instability of few-layer black phosphorus. *2d Mater* **2**, 011002 (2015).

10. Liu, H. *et al.* Phosphorene: An Unexplored 2D Semiconductor with a High Hole Mobility.

Acs Nano **8**, 4033-4041, doi:10.1021/nn501226z (2014).

11. Miao, J. S., Zhang, S. M., Cai, L., Scherr, M. & Wang, C. Ultrashort Channel Length Black Phosphorus Field-Effect Transistors. *Acs Nano* **9**, 9236-9243 (2015).

12. Ling, X., Wang, H., Huang, S., Xia, F. & Dresselhaus, M. S. The renaissance of black phosphorus. *Proceedings of the National Academy of Sciences* **112**, 4523-4530 (2015).

13. Yang, J. *et al.* Atomically thin optical lenses and gratings. *Light-Sci Appl* **5**, doi:ARTN e16046 10.1038/lsa.2016.46 (2016).

14. Cheng, Y. H., Chen, C. H., Yu, K. Y. & Hsueh, W. J. Extraordinary light absorptance in graphene superlattices. *Opt Express* **23**, 28755-28760, doi:10.1364/Oe.23.028755 (2015).

15. Othman, M. A. K., Guclu, C. & Capolino, F. Graphene-dielectric composite metamaterials: evolution from elliptic to hyperbolic wavevector dispersion and the transverse epsilon-near-zero condition. *J Nanophotonics* **7**, doi:Artn 073089 10.1117/1.Jnp.7.073089 (2013).

16. Lotsch, B. V. Vertical 2D Heterostructures. *Annu Rev Mater Res* **45**, 85-109, doi:10.1146/annurev-matsci-070214-020934 (2015).

17. Xiong, F. *et al.* Li Intercalation in MoS2: In Situ Observation of Its Dynamics and Tuning Optical and Electrical Properties. *Nano Lett* **15**, 6777-6784, doi:10.1021/acs.nanolett.5b02619 (2015).

18. Yu, Y. J. *et al.* Gate-tunable phase transitions in thin flakes of 1T-TaS2. *Nat Nanotechnol* **10**, 270-276, doi:10.1038/Nnano.2014.323 (2015).

19. Nishii, T., Maruyama, Y., Inabe, T. & Shirotani, I. Synthesis and Characterization of Black Phosphorus Intercalation Compounds. *Synthetic Met* **18**, 559-564, doi:Doi

10.1016/0379-6779(87)90940-4 (1987).

20. Li, L. *et al.* Direct observation of the layer-dependent electronic structure in phosphorene. *Nat Nano*, **12**, 21-25 (2016).

21. Castellanos-Gomez, A. Black phosphorus: narrow gap, wide applications. *The journal of physical chemistry letters* **6**, 4280-4291 (2015).

22. Guan, J., Song, W. S., Yang, L. & Tomanek, D. Strain-controlled fundamental gap and structure of bulk black phosphorus. *Phys Rev B* **94**, doi:Artn 045414 10.1103/Physrevb.94.045414 (2016).

23. Paradies, H. H. & Clancy, S. F. Crystalline Polymorphism Of Cetyltrimethylammo-Nium Bromide And Distearyldimethylammonium (Dsdma) Compounds. A Comparison Of The Hydrated Dsdma-Chloride, Dsdma-S-(+)-Lactate And Dsdma-Pyruvate Systems. *Rigaku J* **17**, 20-34 (2000).

24. Kresse, G. & Hafner, J. *Ab initio* molecular dynamics for liquid metals. *Phys. Rev. B* **47**, 558-561 (1993).

25. Kresse, G. & Furthmüller, J. Efficient iterative schemes for *ab initio* total-energy calculations using a plane-wave basis set. *Phys. Rev. B* **54**, 11169-11186 (1996).

26. Kresse, G. & Joubert, D. From ultrasoft pseudopotentials to the projector augmented-wave method. *Phys. Rev. B* **59**, 1758-1775 (1999).

27. Blöchl, P. E. Projector augmented-wave method. *Phys. Rev. B* **50**, 17953-17979 (1994).

28. Monkhorst, H. J. & Pack, J. D. Special points for Brillouin-zone integrations. *Phys. Rev. B* **13**, 5188-5192 (1976).

29. Perdew, J. P., Burke, K. & Ernzerhof, M. Generalized Gradient Approximation Made

Simple. *Phys. Rev. Lett.* **77**, 3865-3868 (1996).

30. Liu, Y., Merinov, B. V. & Goddard, W. A. Origin of low sodium capacity in graphite and generally weak substrate binding of Na and Mg among alkali and alkaline earth metals. *Proc. Natl. Acad. Sci. USA* **113**, 3735-3739, doi:10.1073/pnas.1602473113 (2016).

31. Xiao, H., Tahir-Kheli, J. & Goddard, W. A. Accurate Band Gaps for Semiconductors from Density Functional Theory. *The Journal of Physical Chemistry Letters* **2**, 212-217, doi:10.1021/jz101565j (2011).

32. Crowley, J. M., Tahir-Kheli, J. & Goddard, W. A. Resolution of the Band Gap Prediction Problem for Materials Design. *The Journal of Physical Chemistry Letters* **7**, 1198-1203, doi:10.1021/acs.jpclett.5b02870 (2016).

33. Fei, R. & Yang, L. Lattice vibrational modes and Raman scattering spectra of strained phosphorene. *Appl Phys Lett* **105**, 083120 (2014).

34. Rudenko, A. N., Brener, S. & Katsnelson, M. I. Intrinsic Charge Carrier Mobility in Single-Layer Black Phosphorus. *Physical Review Letters* **116**, 246401 (2016).

35. Du, H. W., Lin, X., Xu, Z. M. & Chu, D. W. Recent developments in black phosphorus transistors. *J Mater Chem C* **3**, 8760-8775, doi:10.1039/c5tc01484k (2015).

36. Bohloul, S., Zhang, L., Gong, K. & Guo, H. Theoretical impurity-limited carrier mobility of monolayer black phosphorus. *Appl Phys Lett* **108**, doi:Artn 033508 10.1063/1.4940381 (2016).

37. Chen, X. L. *et al.* High-quality sandwiched black phosphorus heterostructure and its quantum oscillations. *Nature Communications* **6**, doi:Artn 7315 10.1038/Ncomms8315 (2015).

38. Ziletti, A., Carvalho, A., Campbell, D. K., Coker, D. F. & Castro Neto, A. H. Oxygen Defects in Phosphorene. *Physical Review Letters* **114**, 046801 (2015).

39. Favron, A. *et al.* Photooxidation and quantum confinement effects in exfoliated black phosphorus. *Nat Mater*, **14**, 826-832 doi:10.1038/nmat4299 (2015).

40. Doganov, R. A. *et al.* Transport properties of pristine few-layer black phosphorus by van der Waals passivation in an inert atmosphere. *Nature Communications* **6**, doi:Artn 6647 10.1038/Ncomms7647 (2015).

41. Avsar, A. *et al.* Air-Stable Transport in Graphene-Contacted, Fully Encapsulated Ultrathin Black Phosphorus-Based Field-Effect Transistors. *Acs Nano* **9**, 4138-4145 (2015).

42. Cai, J. M. *et al.* Graphene nanoribbon heterojunctions. *Nat Nanotechnol* **9**, 896-900 (2014).

43. Yu, W. J., Liao, L., Chae, S. H., Lee, Y. H. & Duan, X. F. Toward Tunable Band Gap and Tunable Dirac Point in Bilayer Graphene with Molecular Doping. *Nano Lett* **11**, 4759-4763, doi:10.1021/nl2025739 (2011).

44. Duan, X. D. *et al.* Lateral epitaxial growth of two-dimensional layered semiconductor heterojunctions. *Nat Nanotechnol* **9**, 1024-1030, doi:Doi 10.1038/Nnano.2014.222 (2014).

45. Levendorf, M. P. *et al.* Graphene and boron nitride lateral heterostructures for atomically thin circuitry. *Nature* **488**, 627-632, doi:10.1038/nature11408 (2012).

46. Cai, Y., Zhang, G. & Zhang, Y.-W. Layer-dependent band alignment and work function of few-layer phosphorene. *Scientific reports* **4** (2014).

47. Sole, C., Drewett, N. E. & Hardwick, L. J. In situ Raman study of lithium-ion intercalation into microcrystalline graphite. *Faraday Discuss* **172**, 223-237,

doi:10.1039/c4fd00079j (2014).

48. Hembram, K. P. S. S. *et al.* A comparative first-principles study of the lithiation, sodiation, and magnesiation of black phosphorus for Li-, Na-, and Mg-ion batteries. *Phys Chem Chem Phys* **18**, 21391-21397, doi:10.1039/c6cp02049f (2016).

49. Hembrarn, K. P. S. S. *et al.* Unraveling the Atomistic Sodiation Mechanism of Black Phosphorus for Sodium Ion Batteries by First-Principles Calculations. *J Phys Chem C* **119**, 15041-15046, doi:10.1021/acs.jpcc.5b05482 (2015).

50. Yang, Z. B. *et al.* Field-Effect Transistors Based on Amorphous Black Phosphorus Ultrathin Films by Pulsed Laser Deposition. *Adv Mater* **27**, 3748-3754 (2015).

51. Xia, F., Wang, H. & Jia, Y. Rediscovering black phosphorus as an anisotropic layered material for optoelectronics and electronics. *Nature communications* **5**, 4458 (2014).

52. Kamalakar, M. V., Madhushankar, B. N., Dankert, A. & Dash, S. P. Low Schottky Barrier Black Phosphorus Field-Effect Devices with Ferromagnetic Tunnel Contacts. *Small* **11**, 2209-2216, doi:10.1002/smll.201402900 (2015).

53. Youngblood, N., Chen, C., Koester, S. J. & Li, M. Waveguide-integrated black phosphorus photodetector with high responsivity and low dark current. *Nature Photonics*, **9**, 247-252 (2015).

54. Na, J. *et al.* Few-Layer Black Phosphorus Field-Effect Transistors with Reduced Current Fluctuation. *Acs Nano* **8**, 11753-11762 (2014).

55. Wood, J. D. *et al.* Effective passivation of exfoliated black phosphorus transistors against ambient degradation. *Nano Lett* **14**, 6964-6970 (2014).

56. Buscema, M. *et al.* Fast and Broadband Photoresponse of Few-Layer Black Phosphorus

Field-Effect Transistors. *Nano Lett* **14**, 3347-3352 (2014).

57. Kim, J. S. *et al.* Dual Gate Black Phosphorus Field Effect Transistors on Glass for NOR Logic and Organic Light Emitting Diode Switching. *Nano Lett* **15**, 5778-5783 (2015).

58. Hong, T. *et al.* Polarized photocurrent response in black phosphorus field-effect transistors. *Nanoscale* **6**, 8978-8983 (2014).

59. Koenig, S. P., Doganov, R. A., Schmidt, H., Neto, A. H. C. & Ozyilmaz, B. Electric field effect in ultrathin black phosphorus. *Appl Phys Lett* **104**, doi:Artn 103106 10.1063/1.4868132 (2014).

60. Zhu, W. N. *et al.* Flexible Black Phosphorus Ambipolar Transistors, Circuits and AM Demodulator. *Nano Lett* **15**, 1883-1890, doi:10.1021/nl5047329 (2015).

61. Kah-Wee, A., Zhi-Peng, L. & Juntao, Z. in *Digital Signal Processing (DSP), 2015 IEEE International Conference on.* 1223-1226.

62. Viti, L. *et al.* Efficient Terahertz detection in black-phosphorus nano-transistors with selective and controllable plasma-wave, bolometric and thermoelectric response. *Scientific Reports* **6**, doi:Artn 20474 10.1038/Srep20474 (2016).

63. Zhou, H. L. *et al.* Large Area Growth and Electrical Properties of p-Type WSe2 Atomic Layers. *Nano Lett* **15**, 709-713, doi:Doi 10.1021/Nl504256y (2015).